

Dileptons and resonances as probes for hot and dense nuclear matter

DISSERTATION
ZUR ERLANGUNG DES DOKTORGRADES
DER NATURWISSENSCHAFTEN

VORGELEGT BEIM FACHBEREICH PHYSIK
DER JOHANN WOLFGANG GOETHE - UNIVERSITÄT
IN FRANKFURT AM MAIN

VON
SASCHA VOGEL
AUS FRANKFURT AM MAIN

FRANKFURT 2009
(D 30)

VOM FACHBEREICH PHYSIK DER
JOHANN WOLFGANG GOETHE - UNIVERSITÄT ALS DISSERTATION
ANGENOMMEN.

DEKAN:

GUTACHTER:

DATUM DER DISPUTATION:

— *Zwei Dinge sind zu unserer Arbeit nötig: Unermüdliche Ausdauer und die Bereitschaft, etwas, in das man viel Zeit und Arbeit gesteckt hat, wieder wegzuwerfen.*

Albert Einstein

1

Zusammenfassung

Diese Arbeit behandelt die Analyse von Signalen zur Wiederherstellung der chiralen Symmetrie. Sie ist unterteilt in ein einführendes Kapitel, die in die Thematik und die Physik einleiten und Kapitel, die die Ergebnisse der durchgeführten Studien erläutern. Obwohl die Arbeit als durchgängiger Text konzipiert ist, wurde darauf Wert gelegt, dass jedes Kapitel alleinstehend zu verstehen und als solches abgeschlossen ist.

Zunächst wird in Kapitel 2 das Thema der Schwerionenkollisionen eingeführt und die Motivation derartiger Experimente vorgestellt. Der grobe Verlauf einer solchen Reaktion wird erläutert und der Zusammenhang zur Physik des frühen Universums hervorgehoben. Es werden verschiedene Observablen von Schwerionenkollisionen diskutiert, die in den folgenden Kapiteln näher beleuchtet werden. Hierbei wird darauf geachtet, dass die

zugrundeliegenden Konzepte anstatt spezieller Fragestellungen diskutiert werden, um einen Einblick in das Thema zu ermöglichen.

Das folgende Kapitel 3 führt in die Thematik der chiralen Symmetrie ein. Es wird der Unterschied zwischen expliziter und spontaner Symmetriebrechung diskutiert und an Beispielen erläutert. Speziell wird das sogenannte “mexican hat”-Potential erklärt, welches in einem klassischen Analogon die spontane Symmetriebrechung verdeutlicht. Des Weiteren werden Quantenzustände diskutiert, die die Quantenzahlen verschiedener Mesonen haben. Außerdem wird der Zusammenhang zwischen der spontanen Symmetriebrechung und der Entartung der Massen des ρ und a_1 Mesons verdeutlicht sowie angerissen, warum eine Verschiebung der Mesonenmassen ein mögliches (aber nicht zwangsläufig hinreichendes) Signal der Wiederherstellung der chiralen Symmetrie ist.

Um in den folgenden Kapiteln mögliche Dileptonen-Messungen zu diskutieren, werden in Kapitel 4 die Grundlagen von Zerfällen in Dileptonen erläutert, unter anderem der Unterschied zwischen Zerfällen in dileptonischen und hadronischen Zerfallskanälen, welche in späteren Kapiteln noch genauer untersucht werden. Hier wird auch der Unterschied zwischen Dalitzzerfällen und direkten Zerfällen erläutert. Im Folgenden werden dann Zerfallsbreiten abgeleitet, die in den theoretischen Studien verwendet wurden. Hier werden auch die implementierten Formfaktoren diskutiert. Im letzten Unterkapitel wird die sogenannte “shining”-Methode vorgestellt, die dann in der tatsächlichen Modellierung verwendet wurde.

Das anschliessende Kapitel 5 gibt einen kurzen Überblick über einige Experimente, die Resonanz-Studien durchführen. Es werden die wichtigsten Detektoren diskutiert, im Speziellen die der Experimente: DLS, HADES, CERES, NA60, PHENIX, CBM und ALICE. Die Detektoren werden hier nicht im Detail besprochen, hingegen soll vielmehr Wert darauf gelegt

werden, dass die generelle Funktionsweise des Experiments deutlich wird. Bedeutende physikalische Entdeckungen werden angerissen.

In Kapitel 6 werden theoretische Modelle vorgestellt, die zur Beschreibung von Schwerionenkollisionen verwendet werden. Insbesondere werden Statistische Modelle, Hydrodynamische Modelle und Transportmodelle beschrieben. Da zur Durchführung dieser Arbeit ein Transportmodell verwendet wurde, werden Transportmodelle, und vor allem das UrQMD-Modell (Ultra-relativistic Quantum Molecular Dynamics) in größerer Genauigkeit beschrieben. Hierzu wird zuerst der QMD-Ansatz diskutiert und im Folgenden die beinhalteten Teilchensorten und die verwendeten Wirkungsquerschnitte in UrQMD erläutert. Schließlich wird auf die Produktion von Mesonen und der Zerfall von Resonanzen eingegangen, wobei letztgenannte von besonderer Bedeutung für diese Arbeit sind.

Kapitel 7 gibt einen Überblick über einige aktuelle Resonanz-Studien. Hier stehen besonders experimentelle Ergebnisse der STAR, NA60, HADES und CLAS Kollaborationen im Vordergrund.

Kapitel 8 beinhaltet dann die erste von mehreren Analysen, die im Rahmen dieser Arbeit durchgeführt wurden. Die Untersuchung der a_1 -Spektralfunktion und der experimentell bestimmbaren Massenspektren wird als “smoking gun”-Signal gehandelt, um die Wiederherstellung der chiralen Symmetrie zu detektieren. Somit ist eine theoretische Analyse der möglichen Zerfallskanäle von besonderer Wichtigkeit. Es werden die verschiedenen Kanäle, insbesondere der Zerfall $a_1 \rightarrow \gamma \pi$ und der Zerfall $a_1 \rightarrow \rho \pi$ analysiert. Hier wird die Massenabhängigkeit der Zerfallsbreiten diskutiert, die zu einer Verzerrung des Massenspektrums führt, wenn man das a_1 Meson in bestimmten Zerfallskanälen misst (insbesondere im $a_1 \rightarrow \gamma \pi$ Zerfallskanal). Dies hat weitreichende Konsequenzen zur experimentellen Bestimmung der Restaurierung der chiralen Symmetrie, da kinematische

Faktoren eine größere Rolle spielen als bisher vermutet.

Der Fokus des Kapitels 9 liegt auf der Analyse von Massenspektren von Dileptonen in elementaren (p+p) und C+C Kollisionen. Hier wird zuerst der Einfluss der Isospin-Asymmetrie der η -Produktion untersucht, was dann in die Analyse der Dileptonen-Massenspektren einfließt. Zunächst werden elementare Reaktionen im Energiebereich des DLS-Experiments analysiert und mit experimentellen Daten verglichen. Im weiteren Verlauf des Kapitels werden elementare und C+C Reaktionen diskutiert, wobei im Besonderen der Energiebereich des HADES-Programms abgedeckt wird. An dieser Stelle werden die Rechnungen auch mit experimentellen Daten verglichen. Des Weiteren wird die Wichtigkeit der genauen Messung der elementaren Wirkungsquerschnitte von Baryonresonanz-Produktion und die Messung von Zerfallsbreiten erörtert. Es wird deutlich, dass die Messung und theoretische Analyse elementarer Reaktionen von besonderer Wichtigkeit ist, um Schwerionen-Daten grundlegend zu simulieren und zu verstehen.

In Kapitel 10 liegt das Gewicht auf der Analyse von Zeit- und Dichte-Evolutionen von Dilepton-Multiplizitäten. Hieraus kann man indirekte Rückschlüsse über die Dynamik des System und die Produktion von Dileptonen aus Resonanzzerfällen gewinnen. Dies ermöglicht eine genaue Antwort auf die Frage, von welcher Dichte die gemessenen Dileptonen emittiert werden. Diese Frage wird im Folgenden in größerer Genauigkeit behandelt.

Kapitel 11 beschäftigt sich mit der Fragestellung, inwieweit man die Hoch-Dichte-Phase einer Schwerionenkollision mit Hilfe von leptonischen Zerfallskanälen untersuchen kann. Hier wird insbesondere auf das ρ Meson eingegangen und geprüft, welche Mechanismen diese Mesonen erzeugen und reabsorbieren. Es wird eine detaillierte Analyse präsentiert, die von SiS (SchwerIonen-Synchrotron) Energien von 2 AGeV bis zu FAIR (Facility for Antiproton and Ion Research) Energien von 30 AGeV reicht. Die so-

nannten “gain”- und “loss”-Terme werden als Funktion der Reaktionszeit diskutiert. Ein weiterer Punkt, der in diesem Kapitel ausführlich besprochen wird ist die Baryondichte-Verteilung der Punkte, an denen ρ Mesonen zerfallen. Dies wird verglichen mit der Dichte-Verteilung der emittierten Dileptonen, die aufgrund der vorher besprochenen “shining”-Methode durchaus unterschiedlich sein kann. Hieraus kann man die experimentell erprobte Dichte für zukünftige Schwerionen-Experimente ableiten. Da die ρ -Mesonen, die in der Hochdichte-Phase entstehen, quasi instantan wieder reabsorbiert werden, ist die Chance ein ρ -Meson aus dieser Phase der Reaktion zu rekonstruieren sehr gering.

Das abschließende Kapitel 12 durchleuchtet das Thema der maximal rekonstruierbaren Dichte in Schwerionenkollisionen von einem anderen Blickpunkt. In diesem Kapitel liegt der Fokus auf hadronischen Zerfallskanälen und der Möglichkeit Resonanzen in diesen Zerfallskanälen zu rekonstruieren. Es wird der Anteil der rekonstruierbaren Resonanzen als Funktion der Dichte ausgewertet und ein unerwarteter Anstieg bei höheren Dichten diskutiert. Dieser ist besonders ausgeprägt bei sehr hohen Schwerpunktenergien. Diskutiert werden insbesondere Kollisionen bei FAIR-Energien von $E_{lab} = 30$ AGeV und RHIC-Energien von $\sqrt{s} = 200$ AGeV. Der Ursprung dieses Anstiegs liegt darin, dass die ersten Kollisionen einen sehr hohen transversalen Impuls der Reaktionsprodukte ermöglichen. Diese Reaktionsprodukte werden zwar bei extrem hoher Dichte produziert, es ist aber relativ wahrscheinlich, dass sie die Reaktionszone aufgrund des hohen transversalen Impulses schnell verlassen. Dies wiederum führt zu einer erhöhten Rekonstruierbarkeit. Es eröffnet sich hierdurch eine Möglichkeit die Hochdichte-Phase von Schwerionenkollisionen zu erforschen, welche seit Kurzem auch experimentell verfolgt wird.

Die Arbeit endet in einer Zusammenfassung und einem Ausblick.

Contents

1	Zusammenfassung	3
2	Introduction	16
2.1	Motivation	16
2.1.1	Heavy Ion Physics - Goals and Concept	19
2.2	Structure of this thesis	21
3	Chiral Symmetry	25
3.1	Explicit and spontaneous symmetry breaking	25
3.2	Chiral symmetry transformations	27
4	Dileptons	33
4.1	Dileptons as an observable for heavy ion collisions	33
4.2	Dilepton decays	35
4.3	Decay widths	37
4.4	Shining method	39
5	Experiments	41
5.1	Experiments at low energies	43
5.2	Experiments at intermediate energies	45
5.3	Experiments at high energy	47
5.4	Future experiments	49
6	Theoretical Models for Heavy Ion Collisions	53
6.1	Statistical models	54

6.2	Hydrodynamics	61
6.3	Transport models	62
6.4	UrQMD	64
6.4.1	Particle species	67
6.4.2	Cross sections	69
6.4.3	Meson production and resonance decays	70
7	Resonances as a probe of heavy ion collisions	75
8	The a_1 meson as a signature for chiral symmetry restoration	83
8.1	The a_1 as an observable for chiral symmetry restoration	83
8.2	Experimental reconstruction	85
8.3	Mass dependent branching ratios	87
8.4	Distribution in space and time	91
9	Dilepton production at SiS energies - mass spectra	95
9.1	Isospin asymmetry in η production	97
9.2	ρ production	99
9.3	Elementary reactions	101
9.3.1	Comparison to DLS measurements	101
9.3.2	Predictions for HADES	103
9.4	Dilepton yields in C+C collisions	104
9.5	Predictions for Ar+KCl	108
9.6	Investigating effects of baryon resonance production cross sections	109
10	Dilepton production at SiS energies - time evolution	113
10.1	Time evolution	114
10.2	Density evolution	116
11	How sensitive are ρ mesons to the hot and dense stage of heavy ion collisions?	119
11.1	The change of ρ meson properties as an observable in heavy ion collisions	119

11.2 Approaches to model dileptons from ρ mesons	121
11.3 Density calculation	124
11.4 Gain and loss rates of ρ mesons	126
11.5 Dilepton rates	130
12 High p_T resonances as a possibility to explore hot and dense nuclear matter	133
12.1 Problems of hadronic decay channels	133
12.2 Reconstruction probability in heavy ion collisions	136
12.3 Using high p_T resonances to explore the hot and dense phase .	138
13 Conclusions	141

List of Figures

2.1	Evolution of the Universe	17
2.2	Schematic Evolution of a heavy ion collision	19
2.3	Schematic phase diagram of nuclear matter	21
3.1	Mexican hat potential	27
4.1	Schematic view of resonances decaying in a medium	35
4.2	Schematic view of dilepton abundancies of different species as a function of mass.	36
5.1	Schematic view of the DLS experiment	43
5.2	Schematic view of the HADES experiment	44
5.3	Schematic view of the CERES experiment	45
5.4	Schematic view of the NA60 experiment	46
5.5	Schematic view of the PHENIX experiment	47
5.6	Schematic view of the CBM experiment with absorber	49
5.7	Schematic view of the CBM experiment without absorber	50
5.8	Schematic view of the ALICE experiment	51
6.1	Thermal particle ratios at production as a function of temper- ature	57
6.2	Thermal particle ratios as a function of time and temperature	60
6.3	ρ meson mass spectrum as an example for baryon resonance contributions	73

LIST OF FIGURES

7.1	Thermal model calculations for particle ratios compared with experimental data from the various RHIC experiments	76
7.2	Resonance over non-resonance ratio as a function of charged particles of the collision	77
7.3	K^{*0} meson mass and width as a function of transverse momentum as measured by the STAR experiment	78
7.4	ρ^0 meson mass as a function of transverse momentum as measured by the STAR experiment	79
7.5	NA60 result on the ρ meson spectral function measured in semi-central In-In collisions at 158 AGeV beam energy	80
7.6	Dilepton spectrum for 2 AGeV C+C collisions measured by HADES	81
7.7	e^+e^- spectrum for photon induced reactions as measured by CLAS	82
8.1	Mass distribution of a_1 mesons in proton-proton collisions	87
8.2	Mass distribution of a_1 mesons in central Au+Au collisions	88
8.3	Mass dependent branching ratios for the a_1 meson with the two exit channel of $\gamma\pi$ and $\rho\pi$	90
8.4	Mass distribution of a_1 mesons as constructed in the $\gamma\pi$ decay channel	91
8.5	Baryon density distribution of a_1 mesons which decay into $\gamma\pi$ for central Au+Au collisions at 20 and 30 AGeV	92
8.6	The a_1 meson mass spectrum for 20 AGeV Au+Au collisions evaluated during different times of the collision	92
8.7	Scatterplot of the space-distribution (in x-y-plane) of $a_1 \rightarrow \gamma\pi$ decays	93
9.1	The η production cross section from pn reactions as a function of the excess energy	98
9.2	Average η multiplicity in C+C reactions at 1 AGeV and 2 AGeV from UrQMD in comparison to TAPS data	98
9.3	Cross sections for ρ^0 meson production in pp collisions	99

9.4	UrQMD model calculations for dilepton spectra from pp reactions at 1.04, 1.27, 1.61, 1.85 , 2.09 and 4.88 GeV in comparison to the DLS data	102
9.5	UrQMD model calculations for dilepton spectra from p+p collisions at HADES beam energies	103
9.6	UrQMD model calculations for dilepton spectra from C+C collisions at HADES beam energies	105
9.7	Comparison between the decay vertex and the shining methods for C+C collisions at HADES beam energies	106
9.8	UrQMD model calculations for dilepton invariant mass spectra from Ar+KCl collisions at beam energy of 1.75 AGeV	108
9.9	Cross sections for ρ^0 meson production in pp collisions with modified cross sections for baryon resonance production	110
9.10	UrQMD model calculations for dilepton spectra from pp reactions at 1.04, 1.27, 1.61, 1.85 , 2.09 and 4.88 GeV in comparison to the DLS data with modified resonance production cross section	111
9.11	Dilepton spectrum for C+C collisions with modified resonance production cross section	112
10.1	Dilepton multiplicity for minimal bias C+C collisions at beam energies of 2 AGeV as a function of time	115
10.2	Dilepton multiplicity from minimal bias C+C collisions at beam energies of 2 AGeV as a function of the time and density using two different methods of extracting dileptons	117
10.3	Dilepton multiplicity from minimal bias C+C collisions at beam energies of 2 AGeV as a function of the local density	118
11.1	Time evolution of the local rest frame baryon density ρ_B averaged over the positions of the individual hadrons for central Au+Au/Pb+Pb reactions at various beam energies	122
11.2	Gain and loss rates of ρ mesons for central Au+Au/Pb+Pb collisions at 2, 11 and 30 AGeV	124
11.3	Gain and loss of ρ mesons separated for collisions and decay	125

LIST OF FIGURES

11.4	Baryon density distribution at the space points where the ρ mesons decay	126
11.5	Distribution of the baryon density at which the e^+e^- -pairs from the ρ vector meson are emitted	127
11.6	Average baryon density experienced by a ρ meson as a function of the mass of the ρ meson	130
12.1	Fraction of reconstructable baryon and meson resonances as a function of baryon density	136
12.2	Probability distribution of baryon density at the production vertex for various reconstructable resonances in central ($b \leq 3.4$ fm) Au+Au collisions at 30 AGeV and 200 AGeV as a function of baryon density	138
12.3	Average transverse momentum of reconstructable or all Δ baryons and ρ mesons as a function of baryon density	139
12.4	Transverse momentum spectra for all and reconstructable resonances for central ($b \leq 3.4$ fm) Au+Au collision at 30 AGeV beam energy and 200 AGeV center of mass energy.	140

List of Tables

6.1	Included Baryons in UrQMD	68
6.2	Included Mesons in UrQMD	68
6.3	Masses, widths and branching ratios for non-strange baryon-resonances in UrQMDv2.3	74

— *All science is either physics or stamp collecting.*

Ernest Rutherford

2

Introduction

2.1 Motivation

One of the most striking questions in physics is the question of how the universe started and evolved. The most popular (and possibly through observations best supported) theory concerning the start of the universe is the so called “Big Bang Theory”, which states that the universe started roughly 14 billion years ago with a singular event called the “Big Bang”. Since then the universe is expanding. This, of course, implies that the universe was much hotter and denser in the beginning than it is now and is cooling while expanding.

According to current models and observations which are in line with those models, the universe was undergoing the evolution as schematically pointed out in Fig. 2.1. Depicted is the evolution of the universe as a function of

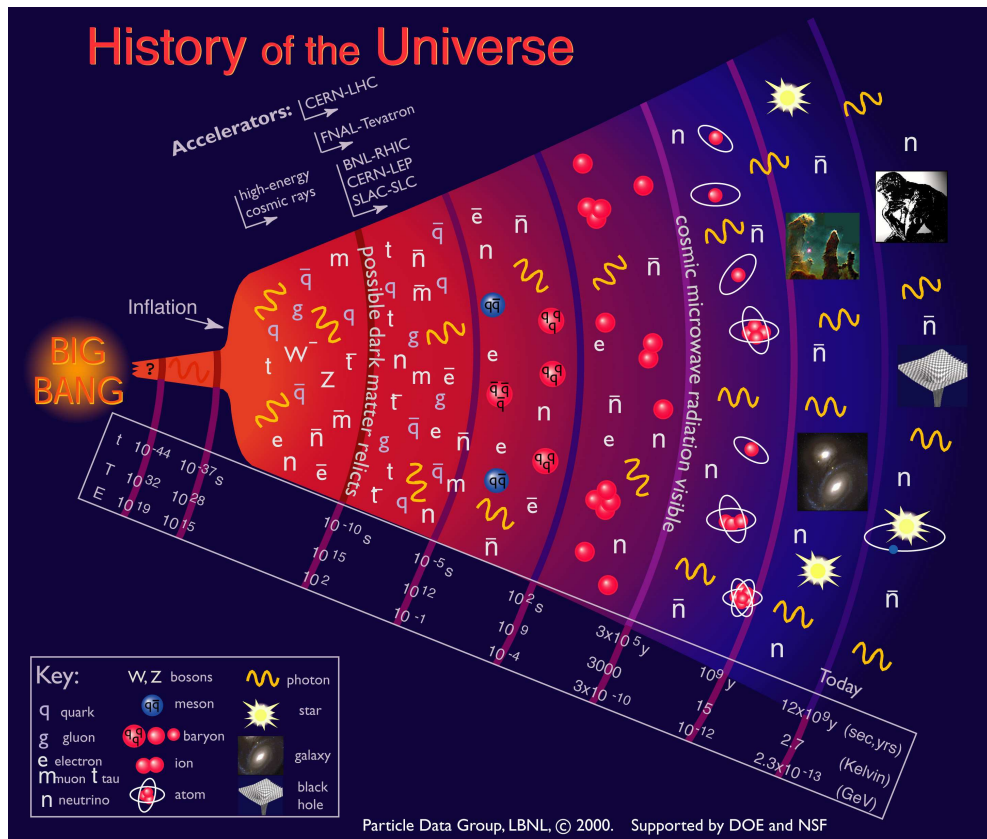


Figure 2.1: The evolution of the universe as a function of time, temperature and corresponding energy. Shown is the content of the universe at a given time.

time, temperature and corresponding energy. As one observes the content of the universe varies with time. In the first some microseconds after the Big Bang the universe consisted of quarks, gluons, leptons and photons. Later on, the quarks hadronize to mesons and baryons and even later form ions. After roughly one hundred thousand years first atoms are formed. It then took roughly one billion years to form planets, galaxies, stars and other macroscopic objects. Additionally to the age of the universe the energy and the temperature is depicted. This will play a role in the experimental investigation of similar systems, which will be discussed in the following.

Due to the uniqueness of the conditions which were realized shortly after the Big Bang the experimental investigation of such an event is challenging to say the least.

In order to create conditions similar to those existent close to the transition from quarks and gluons to hadrons one needs energy densities which are not available naturally on earth. Thus experiments with colliding high energy nuclei are performed in order to create very high energy densities, however on scales of several femtometers (fm). In order to reach such high energies the nuclei are accelerated to velocities near the speed of light and brought into collision. This of course means on the other hand that such a collision only has a duration of several fm / c which is on the order of 10^{-22} to 10^{-23} seconds.

A schematic view of a such a collision is shown in Fig. 2.2¹. The picture divides a high energy heavy ion collision into 5 stages, which are:

- initial state
- pre-equilibrium phase
- QGP phase
- hadronization
- hadronic evolution

The initial state shows two nuclei shortly before the collision. They are not shown spherically to indicate the Lorentz-contraction, which appears at (ultra-)relativistic energies. In the second picture from the left the pre-equilibrium phase is shown. Here the initial collisions of nucleons appear and first particles are formed. However the system is not equilibrated, which is assumed to happen in such collisions. The equilibrium phase is depicted in the picture labeled as “QGP and hydrodynamic expansion”. Here the formerly nucleonic matter is deconfined into quark and gluon matter (which

¹with permission of Steffen Bass

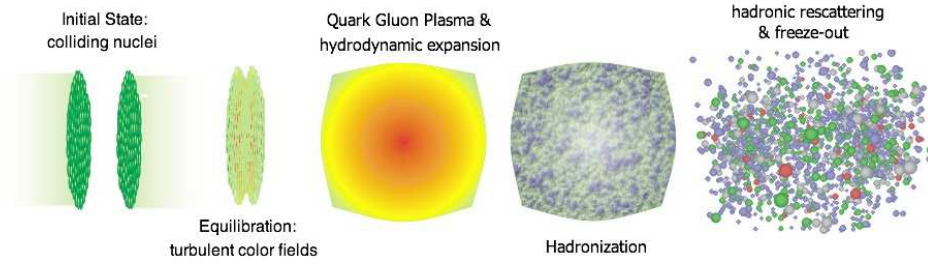


Figure 2.2: Schematic view of a heavy ion collision. From left to right the temporal evolution of such a reaction is shown.

will be explained in a bit more detail later). After the (assumed) equilibrium the quark and gluon matter needs to create hadrons again. This mechanism is not fully understood up to now and a lot of research is being performed in that direction. When the matter is hadronized again the hadrons undergo the hadronic evolution, resonances decay and finally the system freezes out and the final state can be measured in dedicated detectors.

2.1.1 Heavy Ion Physics - Goals and Concept

The overall objective of heavy ion physics is to get a better understanding of the phase diagram of nuclear matter (also referred to as the phasediagram of QCD), which is depicted in Fig. 2.3 ². It shows the temperature of the system against the baryon density. Within this schematic view of the phase diagram several phases of nuclear matter are depicted. At low baryon density and low temperature normal nuclear matter, i.e. nucleons, hadrons and nuclei are located. The point marked with “Nuclei” is at a baryon density of $1 \rho_0$, which is the ground state density of nucleons and the point in the phase diagram where non-excited nuclear is located.

If one increases the temperature or increases the density one reaches a different phase of nuclear matter (depicted e.g. as lines labelled with “RHIC / LHC” or “FAIR SIS 300”). In this state quarks and gluons are expected to be deconfined, that means they are the relevant degrees of freedom instead of

²adapted from <http://www.gsi.de/fair/experiments/CBM/Phasendiagram.jpg>

hadrons. This state of matter is called the “Quark-Gluon-Plasma” (QGP). This transition seems to coincide with another phase transition, the transition to chirally symmetric matter which will be discussed in chapter 3 in detail and possible observables of that transition will be discussed throughout this thesis.

The transition to the QGP is expected to have a critical point, where the first order phase transition turns into a so called cross-over.

At even higher densities a phenomenon called color superconductivity is expected to set in, which is however, except for astrophysical observables such as neutron stars, out of reach for experimental studies in the near and maybe distant future.

Important goals of heavy ion physics are

- to explore the phase diagram of nuclear matter and unambiguously confirm the transition to deconfined nuclear and pin down the relevant parameters
- to unambiguously show the transition to chirally symmetric matter and learn about the corresponding effects
- to create the state of the universe several microseconds after the Big Bang and link its parameters with cosmology

A collision of 2 heavy ions at center of mass energies of 2 AGeV up to 200 AGeV produce up from roughly 10 to 2000 particles. The detection of the particle yield and the identification of the different particles themselves is an interesting observable in itself, however far more interesting are observables which one can link back to the dynamics of the particles, such as momentum spectra, correlations between particles and the like. For this thesis a certain type of particles is of interest, which are resonances. Resonances are particles which decay into other particles, such create correlations between those decay products. There are several ways a

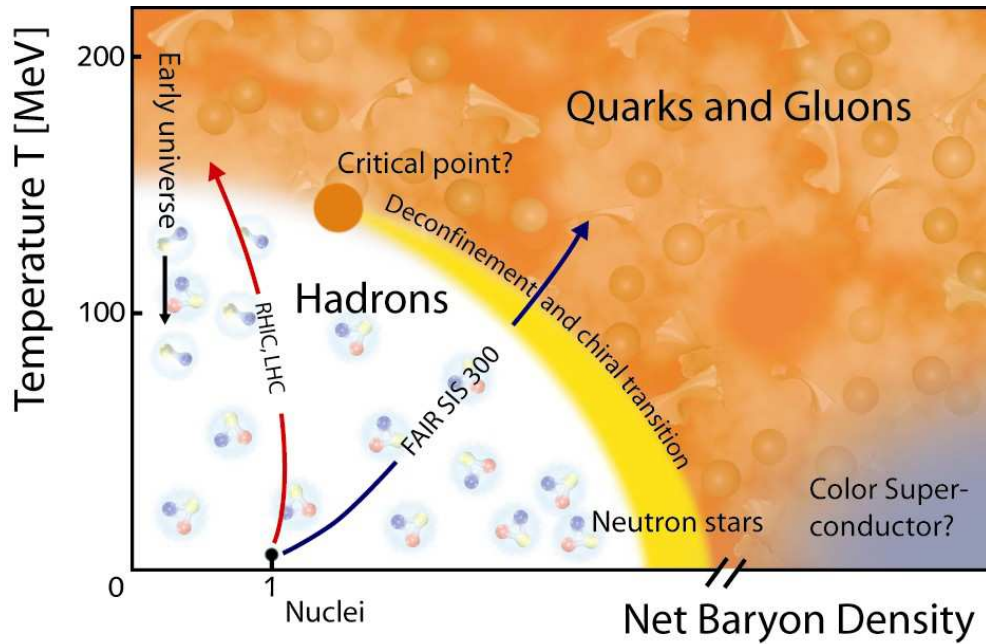


Figure 2.3: Schematic phase diagram of nuclear matter

resonance can decay, most important for the analyses presented in this work is that they can decay via the strong interaction (i.e. into other hadrons) or via the electromagnetic interaction (i.e. into pairs of leptons).

We will discuss the behaviour of resonances in hot and dense nuclear matter throughout this thesis and highlight some of the observables which are of importance in this field of physics.

2.2 Structure of this thesis

In general, this thesis is structured into introductory chapters and chapters which will discuss the new results obtained while working on this project. It is designed such, that it should be read as a whole, however each chapter can be read on its own.

In chapter 3 a short introduction into the basics of chiral symmetry is given. The basic concepts of explicit and spontaneous symmetry breaking are discussed and then the chiral symmetry transformations are explained in a bit more detail. Experimental observables such as mass shifts and the degeneracy of mesons are discussed towards the end of this chapter.

Chapter 4 introduces the physics of dileptons and will highlight the differences between hadronic and dileptonic decay channels of resonances and cover on the most relevant decays, which will be discussed later in the thesis. The calculations of the decay widths of the relevant decays are presented. The common techniques to calculate spectra are analyzed.

In the following chapter 5 an elementary introduction to the experimental techniques and the experiments which measure dilepton production is presented. Some experiments (divided into low, intermediate and high energy experiments) will be described, as well as an outlook to future experiments.

Chapter 6 explains the theoretical modeling of heavy ion collisions. A short introduction into the basics of statistical, hydrodynamical and transport models is given. The Quantum Molecular Dynamics (QMD) approach is being discussed in more detail and a description of the model used for this thesis, the UrQMD model (Ultra-relativistic Quantum Molecular Dynamics) is given. Here especially the implemented particles, the cross sections which are used for particle production and the treatment of resonances is presented in more detail.

Chapter 7 gives an overview on several resonance analyses performed in the recent past. The focus lies on experimental analyses, especially by the STAR, NA60, HADES and CLAS collaborations.

In chapter 8 an analysis of the decay channels of the a_1 meson is performed. Here the main focus lies on the feasibility of the a_1 decay analysis as an observable for chiral symmetry restoration. Mass dependent decay widths will be discussed and their influence on the measurement of the $a_1 \rightarrow \gamma\pi$ channel will be shown. This specific channel seemed like a good candidate to explore chiral symmetry, however has limitations which will be analyzed in this chapter.

Chapter 9 presents the analysis of dilepton production in elementary as well as C+C reactions at SiS energies of 1-2 AGeV. The focus of this chapter lies in the analysis of mass spectra and the comparison to experimental data from the DLS and HADES collaborations. The need for more studies in elementary collisions (theoretical as well as experimental) is pointed out.

In the following chapter 10 the analysis of C+C collision at 2 AGeV beam energy is described, but instead of analyzing mass spectra the focus lies in investigating time and density evolutions, which provides further insight into the dynamics of the system.

The following chapters deal with the probability of the detection of resonances from the high density zone of a heavy ion reaction.

Chapter 11 investigates the leptonic decay channels of resonances, and especially the ρ meson. The gain and loss terms of ρ production are discussed as well as the influence of different treatments for dilepton calculations. Finally we argue why the leptonic channel might not be ideal to discover the high density phase.

The hadronic decay channels of resonances are the focus of chapter 12. Here, the sensitivity on the high density phase and the hadronic rescattering of resonance decay products is analyzed. We investigate the dependence of the probability to reconstruct resonances on transverse momentum and

discuss why resonances with high transverse momentum might be suitable to explore the hot and dense phase of heavy ion collisions.

The thesis ends with a conclusion and an outlook.

— *The mathematical sciences particularly exhibit order, symmetry, and limitation; and these are the greatest forms of the beautiful.*

Aristotle

3

Chiral Symmetry

3.1 Explicit and spontaneous symmetry breaking

This chapter gives a brief introduction into the concept of chiral symmetry. It will by far not give a complete overview on the topic, however will introduce the general features of chiral symmetry. For a more detailed description of chiral symmetry we refer to [K97] and references therein.

Let us start with a short explanation about the differences between explicitly broken and spontaneously broken symmetries.

One refers to a explicitly broken symmetry when the equations of motion, respectively the Lagrangian of the theory are *not* invariant under a symmetry transformation. Let us highlight this by an example:

The Lagrangian

$$\mathcal{L}_0 = |\partial_\mu \Phi|^2 + m^2 |\Phi|^2 - \frac{\alpha^2}{4} |\Phi|^4 \quad (3.1)$$

is invariant under the symmetry $\Phi \rightarrow -\Phi$.

However, if one adds a term (not physically motivated in that case)

$$\mathcal{L}_{SB} = \alpha \Phi, \quad (3.2)$$

this symmetry is lost, since the Lagrangian is no longer invariant under the chosen symmetry transformation.

Since we introduced the symmetry breaking term by hand into the Lagrange density the symmetry is *explicitly broken*.

In the case of spontaneously broken symmetry the equation of motions obey a certain symmetry, however the ground-state of the system does not. Although this seems odd at the first glance it can be visualized easily by a classical analog. A very common example is the mexican hat potential, as shown in Fig. 3.1 ¹. Displayed in the top figure labeled as (a) is a symmetry potential, where the ground state is in the middle and the potential, as well as ground state are invariant under rotational symmetry. In the bottom figure labeled as (b) the ground state is no longer in the center of the potential, but some distance away. Since the center point is a (local) maximum it is unstable. This is best visualized by imagining a little ball in the center of the potential. It will roll down to the minimum (the ground state) and break the symmetry. This kind of symmetry breaking is called *spontaneous*

¹as adapted from [K97]

symmetry breaking. The breaking of the symmetry is not put in by hand into the Lagrange density, but the ground state does not obey the symmetry anymore. Some effects of the symmetry are still present though. Rotational excitations of the ball do not cost any energy (since it is moving on a level of same energy), however radial excitations will cost energy.

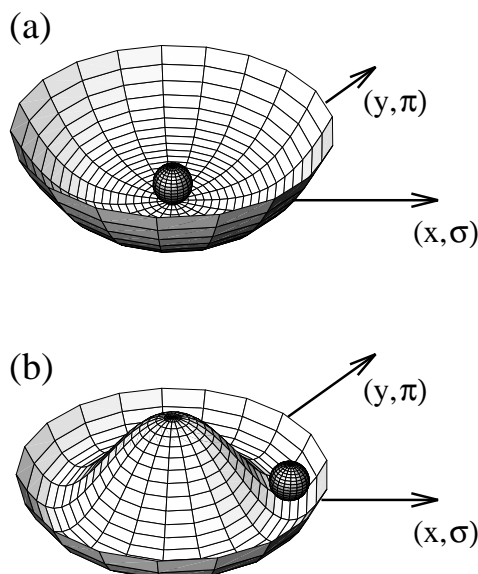


Figure 3.1: The top figure shows a symmetry ground state, whereas the bottom picture displays a ground-state with a broken symmetry. Figure is adapted from [K97].

3.2 Chiral symmetry transformations

After these general remarks, let us focus on chiral symmetry.

Chiral symmetry is a symmetry of QCD, which is exact if all quark masses were zero. For non-vanishing quark masses, which we observe in nature, the

symmetry is not exact, however due to the smallness of the quark masses it is referred to as only slightly broken.

The symmetry transformations of chiral symmetry are the following:

$$\Lambda_V : \psi \longrightarrow e^{-i\frac{\vec{\tau}}{2}\vec{\Theta}}\psi \simeq (1 - i\frac{\vec{\tau}}{2}\vec{\Theta})\psi \quad (3.3)$$

$$\bar{\psi} \longrightarrow e^{+i\frac{\vec{\tau}}{2}\vec{\Theta}}\bar{\psi} \simeq (1 + i\frac{\vec{\tau}}{2}\vec{\Theta})\bar{\psi} \quad (3.4)$$

$$\Lambda_A : \quad \psi \longrightarrow e^{-i\gamma_5\frac{\vec{\tau}}{2}\vec{\Theta}}\psi = (1 - i\gamma_5\frac{\vec{\tau}}{2}\vec{\Theta})\psi \quad (3.5)$$

$$\Rightarrow \bar{\psi} \longrightarrow e^{-i\gamma_5\frac{\vec{\tau}}{2}\vec{\Theta}}\bar{\psi} \simeq (1 - i\gamma_5\frac{\vec{\tau}}{2}\vec{\Theta})\bar{\psi} \quad (3.6)$$

Λ_V is regarded as the vector current transformation, whereas Λ_A is called the axial vector transformation. It can be shown that the Lagrangian of massless fermions is invariant under those transformations which will be done in the following.

The Lagrangian of massless fermions reads:

$$\mathcal{L} = i\bar{\psi}\not{\partial}\psi \quad (3.7)$$

When transforming this Lagrangian under the symmetries 3.3 and 3.4 it turns out that it is invariant under it.

$$i\bar{\psi}\not{\partial}\psi \longrightarrow i\bar{\psi}\not{\partial}\psi - i\vec{\Theta} \left(\bar{\psi}i\not{\partial}\frac{\vec{\tau}}{2}\psi - \bar{\psi}\frac{\vec{\tau}}{2}i\not{\partial}\psi \right) \quad (3.8)$$

$$= i\bar{\psi}\not{\partial}\psi \quad (3.9)$$

The same holds true for the symmetry transformations 3.5 and 3.6. Note that the second term vanishes because of the anti-commutation relation of the γ matrices.

$$i\bar{\psi}\not{\partial}\psi \longrightarrow i\bar{\psi}\not{\partial}\psi - i\vec{\Theta} \left(\bar{\psi} i\partial_\mu \gamma^\mu \gamma_5 \frac{\vec{\tau}}{2} \psi + \bar{\psi} \gamma_5 \frac{\vec{\tau}}{2} i\partial_\mu \gamma^\mu \psi \right) \quad (3.10)$$

$$= i\bar{\psi}\not{\partial}\psi \quad (3.11)$$

This, however, changes when we introduce a mass term to the Lagrangian:

$$\delta\mathcal{L} = -m(\bar{\psi}\psi) \quad (3.12)$$

By applying the transformations to this term one can see that $\delta\mathcal{L}$ is invariant under the vector transformation, however not invariant under the axial transformation and transforms like the following.

$$\Lambda_A : m(\bar{\psi}\psi) \longrightarrow m\bar{\psi}\psi - 2im\vec{\Theta} \left(\bar{\psi} \frac{\vec{\tau}}{2} \gamma_5 \psi \right) \quad (3.13)$$

However, since quark masses are small (roughly 5 MeV) compared to the relevant scales of QCD ($\Lambda_{QCD} \sim 200$ MeV) and the symmetry breaking term is directly proportional to the mass one refers to this symmetry as an approximate symmetry. The vector current is conserved and the axial current is only slightly broken (thus should be partially conserved).

After having established how a Lagrangian with massless fermions should transform under chiral symmetry let us discuss experimental observables. In order to do so, let us first check what the transformation properties of actual particles are, especially those given in the next step. A combination of quark fields with the right quantum numbers of the following particles is given by:

$$\begin{aligned}
 \text{pion-like state: } \vec{\pi} &\equiv i\bar{\psi}\vec{\tau}\gamma_5\psi; & \text{sigma-like state: } \sigma &\equiv \bar{\psi}\psi \\
 \text{rho-like state: } \vec{\rho}_\mu &\equiv \bar{\psi}\vec{\tau}\gamma_\mu\psi; & \text{a}_1\text{-like state: } \vec{a}_{1\mu} &\equiv \bar{\psi}\vec{\tau}\gamma_\mu\gamma_5\psi
 \end{aligned}$$

Let us now check what the chiral transformations (given above) result in when applied to those particle states.

Applying the vector transformation Λ_V to the pion results in the following:

$$\begin{aligned}
 \pi_i : i\bar{\psi}\tau_i\gamma_5\psi &\longrightarrow i\bar{\psi}\tau_i\gamma_5\psi + \Theta_j \left(\bar{\psi}\tau_i\gamma_5\frac{\tau_j}{2}\psi - \bar{\psi}\frac{\tau_j}{2}\tau_i\gamma_5\psi \right) \\
 &= i\bar{\psi}\tau_i\gamma_5\psi + i\Theta_j\epsilon_{ijk}\bar{\psi}\gamma_5\tau_k\psi
 \end{aligned} \tag{3.14}$$

This can also be written as

$$\vec{\pi} \longrightarrow \vec{\pi} + \vec{\Theta} \times \vec{\pi} \tag{3.15}$$

which is an isospin rotation with the angle Θ .

The same calculation for the ρ -like state gives:

$$\vec{\rho}_\mu \longrightarrow \vec{\rho}_\mu + \vec{\Theta} \times \vec{\rho}_\mu \tag{3.16}$$

Applying the axial transformations leads to the following:

$$\begin{aligned}
 \pi_i : i\bar{\psi}\tau_i\gamma_5\psi &\longrightarrow i\bar{\psi}\tau_i\gamma_5\psi + \Theta_j \left(\bar{\psi}\tau_i\gamma_5\gamma_5\frac{\tau_j}{2}\psi + \bar{\psi}\gamma_5\frac{\tau_j}{2}\tau_i\gamma_5\psi \right) \\
 &= i\bar{\psi}\tau_i\gamma_5\psi + \Theta_i\bar{\psi}\psi
 \end{aligned} \tag{3.17}$$

$$\vec{\pi} \longrightarrow \vec{\pi} + \vec{\Theta}\sigma \tag{3.18}$$

and for the σ -meson

$$\sigma \longrightarrow \sigma - \vec{\Theta}\vec{\pi} \tag{3.19}$$

One observes that the π and the σ are rotated into each other under the axial transformation. Also the ρ rotates into the a_1 :

$$\vec{\rho}_\mu \longrightarrow \vec{\rho}_\mu + \vec{\Theta} \times \vec{a}_{1\mu} \quad (3.20)$$

As stated before Λ_A is a symmetry of Quantum-Chromo-Dynamics. This however, would imply that states which can be rotated into each other should have the same eigenvalues. This on the other hand also would imply that those states (which we identified as different mesons, especially the ρ and a_1 meson) would have the same mass.

Checking this against experimental data however leads to a clear splitting in mass, while the ρ meson has a mass of roughly 770 MeV, the a_1 meson has a mass of 1260 MeV. This huge splitting certainly does not have its origin in the slight explicit breaking of the symmetry by the finite quark masses.

We will see in the following that it has its origin in the spontaneous breakdown of the symmetry.

Therefore we use the before-mentioned analog to link it to the theory of strong interaction. As already shown in Fig. 3.1 the x and y direction can also be written as σ and π fields. Let us assume that the effective QCD Hamiltonian (at zero temperature) has a form similar to Fig. 3.1. The rotations along the spatial axis are then the analog to the axial-vector rotations (which rotates π into σ). The ground state is not at the center of the potential but some finite distance away from it, thus one of the fields certainly has a finite expectation value. This has to be the field with the quantum numbers of the vacuum and thus will be the σ field.

From there follows that the rotations from the ground-state have to be the pionic excitations. Those however do not cost any energy, which means that the pions should be massless.

So the major predictions of *spontaneously broken* chiral symmetry are that pions are massless (due to some corrections they have a small mass, which is in agreement with data) and that the mass of the ρ and the a_1 meson is splitted by roughly a factor of $\sqrt{2}$ (for more information where that factor originates from please refer to [GL60, S69]).

However, if one could restore chiral symmetry one would expect a degeneracy of the masses of the ρ and the a_1 meson. This would lead to measuring the same masses for both particles, which also would lead to the observation that at least one particle needs to shift in mass or broaden substantially in width. It is commonly assumed that the ρ shifts (or respectively broadens) to a somewhat lower mass, which leads to the fact that the a_1 meson needs to shift to lower masses too.

We will discuss those kind of observables in the following of this thesis.

— *Electricity is actually made up of extremely tiny particles called electrons that you cannot see with the naked eye unless you have been drinking.*

Dave Berry

4

Dileptons

4.1 Dileptons as an observable for heavy ion collisions

In general the term dileptons describes a pair of a lepton and its corresponding antiparticle. Thus, three different combinations are possible, which are:

- electron / positron (e^-/e^+)
- muon / anti-muon (μ^-/μ^+)
- tau / anti-tau (τ^-/τ^+)

When referring to dileptons in the context of a heavy ion collision these pairs have the same origin, most commonly a resonance decay (e.g.

$\rho \rightarrow e^+e^-$ or a radiative process (e.g. Bremsstrahlung). The main advantage to use dileptons as an observable in heavy ion collisions is that they do not undergo final state interactions. Once created, they leave the interaction zone undisturbed and thus provide a cleaner probe than hadrons which rescatter after their production. The reason for that is the relative strength of the electromagnetic force compared to the strong force. The coupling constant of the electromagnetic force is $\alpha_{EM} = 1/137$, whereas the coupling constant of the strong interaction is $\alpha_S \sim 1$.

If one wants to measure resonant states (the ρ meson being one of the more prominent examples) one cannot measure the resonance itself due to its short lifetime. Since typical lengthscales of detectors are meters or centimeters and the usual lifetime of a hadronic resonance is on the order of several fm/c the resonance itself will not reach the detector. Thus only indirect measurements are possible. If such a resonance decays its decay products carry the information about the mass, momentum and quantum numbers (due to conservation laws). By measuring these particles one can draw conclusions about the original resonance.

However, if one measures the hadronic decay products, one only measures the final state of the collision, due to the rescattering of the daughter particles after the decay. The final state resonances are created in a dilute medium and thus hadronic decay products can escape the collision zone. This effect might be avoidable though, for a detailed discussion, see chapter 12.

Dileptons on the other hand do not undergo strong interactions and will leave the reaction without further collisions. So by measuring the dileptons from a single event one receives a time-integrated spectrum of the whole collision, since the dileptons left the interaction region immediately. For a schematic view, refer to Fig. 4.1 .

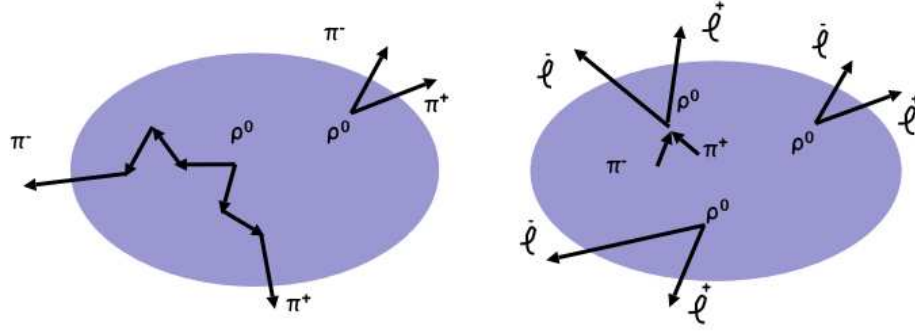


Figure 4.1: Schematic view of resonances decaying in a medium. The left-hand figure shows the decay into hadronic decay products and the subsequent scattering of those daughter particles. The right-hand picture depicts the decay into dileptons and the propagation of the leptons through the hadronic medium without further interaction.

4.2 Dilepton decays

Resonance decays into dileptons are in general divided into two classes. The first class of decays are Dalitz decays, which are 3-body-decays with another particle next to the dilepton pair being emitted. The most important (since most common) Dalitz decays below a mass of 1GeV are:

- $\pi^0 \rightarrow \gamma e^+ e^-$
- $\eta \rightarrow \gamma e^+ e^-$
- $\eta' \rightarrow \gamma e^+ e^-$
- $\omega \rightarrow \pi^0 e^+ e^-$
- $\Delta^{(0/+)} \rightarrow N e^+ e^-$

The second class of dilepton decays are the so-called direct decays, which are 2-body-decays, i.e. the resonance directly decays into the pair of lepton and antilepton. The most important direct decays below a mass of 1GeV are:

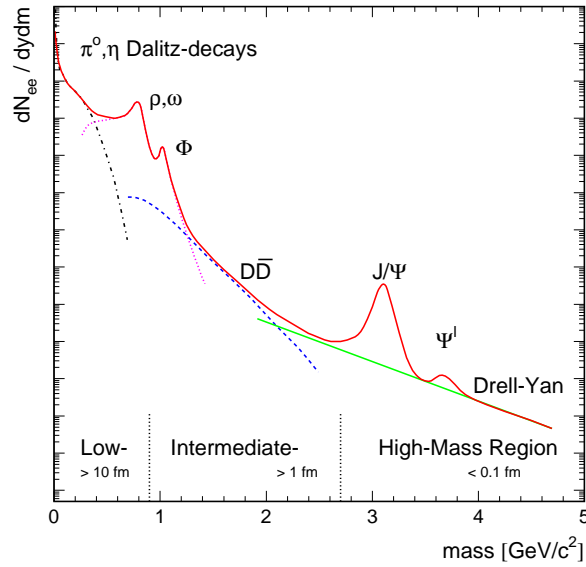


Figure 4.2: Schematic view of dilepton abundancies of different species as a function of mass. Taken from [RW00].

- $\rho^0 \rightarrow e^+e^-$
- $\omega \rightarrow e^+e^-$
- $\phi \rightarrow e^+e^-$

This region is commonly referred to as the low mass region (LMR). Shown schematically in Fig. 4.2 are the most relevant contributions to dilepton mass spectra over a mass-range from 0 to 5 GeV. In the lower mass region (less than 1 GeV in mass) the spectrum is dominated by the π^0 and η decays, with two additional peaks originating from the vector meson decay of the ρ , ω and ϕ .

In the intermediate mass region (roughly between 1 and 3 GeV in mass) the spectrum is populated with a continuum of $D\bar{D}$ decays, whereas in the high mass region (3 GeV and above) the decays of the J/Ψ and Ψ' are most prominent. Also the Drell-Yan process ($q\bar{q} \rightarrow l^+l^-$) gives a non-negligible contribution.

The investigations in this thesis focus on dileptons in the low mass region. The calculations of the widths of the various dilepton decays are in line with [L85, K93, EBB+98] and will be briefly presented in the following.

4.3 Decay widths

Decays of the form

$$P \rightarrow \gamma e^+ e^-, V \rightarrow P e^+ e^- \quad (4.1)$$

with P being a pseudoscalar meson and V a vector meson, can be decomposed into the corresponding decays into a virtual photon γ^* , $P \rightarrow \gamma \gamma^*$, $V \rightarrow P \gamma^*$, and the subsequent decay of the photon via electromagnetic conversion, $\gamma^* \rightarrow e^+ e^-$ [L85, K93, FFK00]:

$$\frac{d\Gamma_{P \rightarrow \gamma e^+ e^-}}{dM^2} = \Gamma_{P \rightarrow \gamma \gamma^*} \frac{1}{\pi M^4} M \Gamma_{\gamma^* \rightarrow e^+ e^-}, \quad (4.2)$$

$$\frac{d\Gamma_{V \rightarrow P e^+ e^-}}{dM^2} = \Gamma_{V \rightarrow P \gamma^*} \frac{1}{\pi M^4} M \Gamma_{\gamma^* \rightarrow e^+ e^-}, \quad (4.3)$$

where M is the mass of the virtual photon or, equivalently, the invariant mass of the lepton pair. The internal conversion probability of the photon is given by:

$$M \Gamma_{\gamma^* \rightarrow e^+ e^-} = \frac{\alpha}{3} M^2 \sqrt{1 - \frac{4m_e^2}{M^2}} \left(1 + \frac{2m_e^2}{M^2} \right) \quad (4.4)$$

with m_e being the electron mass and α being the fine structure constant. The widths $\Gamma_{P \rightarrow \gamma \gamma^*}$ and $\Gamma_{V \rightarrow P \gamma^*}$ can be related to the corresponding radiative widths $\Gamma_{P \rightarrow 2\gamma}$ and $\Gamma_{V \rightarrow P\gamma}$:

$$\Gamma_{P \rightarrow \gamma \gamma^*} = 2 \Gamma_{P \rightarrow 2\gamma} \left(1 - \frac{M^2}{m_P^2}\right)^3 |F_{P\gamma\gamma^*}(M^2)|^2, \quad (4.5)$$

$$\begin{aligned} \Gamma_{V \rightarrow P \gamma^*} &= \Gamma_{V \rightarrow P \gamma} \left[\left(1 + \frac{M^2}{m_V^2 - m_P^2}\right)^2 - \left(\frac{2m_V M}{m_V^2 - m_P^2}\right)^2 \right]^{3/2} \\ &\times |F_{VP\gamma^*}(M^2)|^2, \end{aligned} \quad (4.6)$$

where m_P and m_V are the masses of the pseudoscalar and vector meson respectively and $F_{P\gamma\gamma^*}(M^2)$, $F_{VP\gamma^*}(M^2)$ denote the form factors with $F_{P\gamma\gamma^*}(0) = F_{VP\gamma^*}(0) = 1$. The factor 2 in (4.5) occurs due to the identity of the two photons in the $P \rightarrow 2\gamma$ decay. The form factors can be obtained from the vector meson dominance model (VMD). In the present calculations the following parametrisations are employed [L85, LKBS96]:

$$\begin{aligned} F_{\pi^0}(M^2) &= 1 + b_{\pi^0} M^2, \\ F_{\eta}(M^2) &= \left(1 - \frac{M^2}{\Lambda_{\eta}^2}\right)^{-1}, \\ |F_{\omega}(M^2)|^2 &= \frac{\Lambda_{\omega}^2 (\Lambda_{\omega}^2 + \gamma_{\omega}^2)}{(\Lambda_{\omega}^2 - M^2)^2 + \Lambda_{\omega}^2 \gamma_{\omega}^2}, \\ |F_{\eta'}(M^2)|^2 &= \frac{\Lambda_{\eta'}^2 (\Lambda_{\eta'}^2 + \gamma_{\eta'}^2)}{(\Lambda_{\eta'}^2 - M^2)^2 + \Lambda_{\eta'}^2 \gamma_{\eta'}^2} \end{aligned} \quad (4.7)$$

with $b_{\pi^0} = 5.5 \text{ GeV}^{-2}$, $\Lambda_{\eta} = 0.72 \text{ GeV}$, $\Lambda_{\omega} = 0.65 \text{ GeV}$, $\gamma_{\omega} = 0.04 \text{ GeV}$, $\Lambda_{\eta'} = 0.76 \text{ GeV}$ and $\gamma_{\eta'} = 0.10 \text{ GeV}$. In (4.7) the abbreviations F_P and F_V have been used to denote respectively $F_{P\gamma\gamma^*}$ and $F_{VP\gamma^*}$.

The width for the direct decay of a vector meson $V = \rho^0, \omega, \phi$ to a dilepton pair varies with the dilepton mass like M^{-3} according to [LKBS96]:

$$\Gamma_{V \rightarrow e^+ e^-}(M) = \frac{\Gamma_{V \rightarrow e^+ e^-}(m_V)}{m_V} \frac{m_V^4}{M^3} \sqrt{1 - \frac{4m_e^2}{M^2}} \left(1 + \frac{2m_e^2}{M^2}\right) \quad (4.8)$$

with $\Gamma_{V \rightarrow e^+e^-}(m_V)$ being the partial decay width at the meson pole mass.

The decomposition of the $\Delta \rightarrow Ne^+e^-$ decay into the $\Delta \rightarrow N\gamma^*$ decay and subsequent conversion of the photon leads to the following expression for the differential decay width:

$$\frac{d\Gamma_{\Delta \rightarrow Ne^+e^-}}{dM^2} = \frac{\alpha}{3\pi M^2} \Gamma_{\Delta \rightarrow N\gamma^*} . \quad (4.9)$$

Here the electron mass has been neglected. The decay width into a massive photon reads [WBC+90]:

$$\begin{aligned} \Gamma_{\Delta \rightarrow N\gamma^*}(M_\Delta, M) &= \frac{\lambda^{1/2}(M^2, m_N^2, M_\Delta^2)}{16\pi M_\Delta^2} m_N \\ &\times [2\mathcal{M}_t(M, M_\Delta) + \mathcal{M}_l(M, M_\Delta)] , \end{aligned} \quad (4.10)$$

where the kinematic function λ is defined by $\lambda(m_A^2, m_1^2, m_2^2) = (m_A^2 - (m_1 + m_2)^2)(m_A^2 - (m_1 - m_2)^2)$ and M_Δ is the resonance running mass. The matrix elements \mathcal{M}_t and \mathcal{M}_l are taken from [WBC+90]. The coupling constant g appearing in the expression for \mathcal{M}_t and \mathcal{M}_l has been chosen as $g = 5.44$, in order to reproduce the value of the radiative decay width, as done e.g. in [BCEM99]. Note, that recently a more sophisticated parametrization of the Δ decay width has been derived [KF02]. However, the differences to the current parametrization are small (in the mass range with the largest difference it is on the order of 30% for the total spectra) and therefore the widely used formulas presented above have been applied.

4.4 Shining method

The “shining” method (also called time integration method) was introduced in [LK95] and [HL92b] and assumes that a resonance can continuously emit dileptons over its whole lifetime. The dilepton yield is obtained by integration

of the dilepton emission rate over time, taking the collisional broadening of each individual parent resonance into account:

$$\frac{dN_{e^+e^-}}{dM} = \frac{\Delta N_{e^+e^-}}{\Delta M} = \sum_{j=1}^{N_{\Delta M}} \int_{t_i^j}^{t_f^j} \frac{dt}{\gamma} \frac{\Gamma_{e^+e^-}(M)}{\Delta M} \quad (4.11)$$

Here $\Gamma_{e^+e^-}(M)$ is the electromagnetic decay width of the considered resonance defined in (6.2–4.10) and $t = t_i$ (t_f) the time at which the resonance appeared in (disappeared from) the system.

Thus, even resonances which formally do not *decay*, but are absorbed in another process (e.g. scattering with a proton), still emit dileptons depending on the time-span between their creation and annihilation.

For the calculations applying the “shining” method the whole time evolution of the collision is reconstructed. Each resonance is followed from the production time t_i to a final time t_f at which the resonance decays or is reabsorbed. The reabsorption cross sections are either calculated via the principle of detailed balance or are calculated via the additive quark model. For more details regarding the interactions in the UrQMD model please refer to chapter 6 and [B+98, B+99]. We implement the shining method for the short-lived vector mesons ρ and ω and the baryonic resonance Δ . Also note, that for the analysis shown here, we do not implement any explicit in-medium treatment for dilepton production. The inclusion of scattering between the particles however accounts for collisional broadening dynamically.

In chapter 9 an alternative method also has to be implemented to compare the results. Here, dileptons have been extracted at the point of decay of the resonances, as done e.g. in [SVB06]. The dilepton yield is calculated at the decay vertex from the branching ratio. Thus, in this method the contribution to the dilepton yield of the reabsorbed resonances is neglected. As shown in [VPS+08] this contribution is however small. Unless otherwise stated all calculations in this work apply the shining method for short lived resonances.

— *If your result needs a statistician then you should design a better experiment.*

Ernest Rutherford

5

Experiments

Of course all theoretical investigations of physical systems are nothing but a nice playground if you cannot compare with experimental observations. Thus, experiments and the resulting experimental data are an important part of physics, even for theoretical analyses. The obtained data allows us to constrain theoretical models, distinguish one from the other or falsify them. As stated before dileptons are a relatively rare probe in a heavy ion collision. The branching ratio of e.g. a ρ meson into dileptons is of the order of 10^{-5} , which means that (statistically) out of 10000 ρ mesons only one decays into dileptons. Furthermore you have to take the experimental acceptance and efficiency into account which results in very few dilepton pairs actually being detected.

This results into very specific experimental setups, of which some will be discussed in this chapter.

In general the common features of all the presented experiments (although some of them are more than a ‘pure’ dilepton experiment) are very good triggering systems, excellent lepton identification and methods to suppress the background. As mentioned before, dileptons are a rather rare probe of heavy ion collisions, thus good triggering is essential in order to distinguish the interesting events from the non-interesting events. Since you need to detect dileptons in an event to mark it as ‘interesting’ this obviously goes hand in hand with lepton identification. Finally you have to analyse the selected events and distinguish leptons which actually originate from resonance decays and those which are uncorrelated. Uncorrelated dileptons can originate from single lepton decays of resonance, but also by matching two leptons from different dileptonic decays (e.g. in a event where two ρ mesons decay and you match the leptons incorrectly, i.e. matching e_1^+ and e_2^- from the decays $\rho_1 \rightarrow e_1^+ e_1^-$ and $\rho_2 \rightarrow e_2^+ e_2^-$). There are several techniques for solving this problem, one of the most used being the technique of matching leptons from different events, which are by definition uncorrelated. This spectrum does not have any correlated leptons included. By subtracting this so called ‘mixed event background’ from the spectrum where all leptons within the event have been matched with each other one obtains the spectrum with only the relevant correlations left. For more information please refer to [DFN84].

In the following some experiments designed for dilepton studies will be presented. However note that this list is not extensive and does not give a very detailed but rather a superficial overview over several possible experimental setups. The most important detectors will be described, however for more information we refer to the experimental publications.

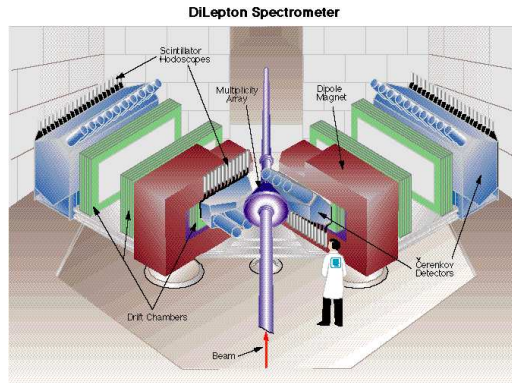


Figure 5.1: Schematic view of the DLS experiment. Picture taken from [DLS].

5.1 Experiments at low energies

DLS

The DLS experiment (**Di-Lepton Spectrometer**) is an experimental setup which took data from 1986 to 1993 at the Bevalac accelerator in Berkeley, USA. It consisted of two identical spectrometer arms, which have been placed at an angle of 40° . The two-angle setup suppresses the background contribution from dilepton pairs with small opening angle, i.e. dileptons from π^0 decay (with a typical opening angle of $15\text{-}25^\circ$) and even more important dileptons from photon conversion (which have a typical opening angle of $\sim 1^\circ$).

Each of the two arms is equipped with a dipole magnet system, with a Cerenkov Counter, a Drift Chamber and a Hodoscope in front of it. Behind the magnet system two additional driftchambers, another Cerenkov Counter and another Hodoscope is positioned.

The main physics motivation of the DLS experiment has been the analysis of dileptons in the low mass region. A discrepancy to theoretical calculations has been found, which lead to various speculations and follow-up experiments (especially the HADES experiment, presented next). This discrepancy is often referred to as the “DLS puzzle”.

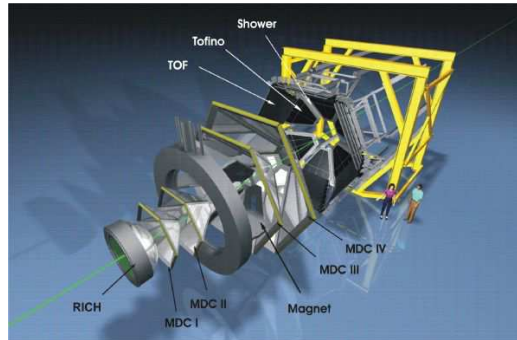


Figure 5.2: Schematic view of the HADES experiment. Picture taken from [HADES].

HADES

The HADES (**H**igh **A**ccceptance **D**i-**E**lectron **S**pectrometer) experiment is located at GSI, Darmstadt. It is still taking data and is currently being upgraded to be a part of the Facility for Antiproton and Ion Research (FAIR). The HADES setup consist of a Ring Imaging Cherenkov detector (RICH), which is a gas radiator for electron identification. It covers the full azimuthal angle. After the RICH the first set of Multiwire Driftchambers (MDC) are positioned, which are used for the determination of the trajectories of the leptons, as well as event characterization and angular distributions. The next part of the experimental setup are superconducting toroidal magnets. The magnetic field is needed to obtain the particle momenta, which are being measured inside the magnetic field. After the magnets the second set of MDCs is located. The final detectors of the HADES setup is a multiplicity / electron trigger array, which consists of granular pre-shower detectors and two walls of scintillator detectors: a time-of-flight (TOF) at angles above 45° and a TOFINO wall at angles below 45° .

For a recent overview of the experiment please refer to [A+09] and references therein. For more studies regarding the physics investigated with that experiment, refer to chapters 9 and 10.

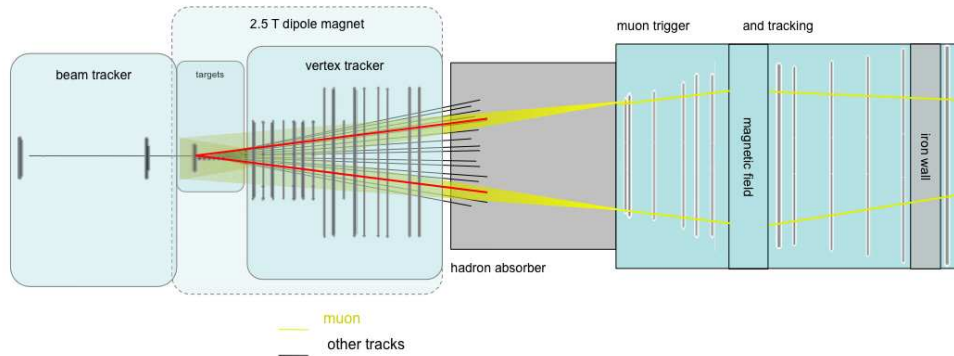


Figure 5.4: Schematic view of the NA60 experiment. Picture taken from [NA60].

NA60

The NA60 experiment is a fixed-target-experiment located at CERN-SPS. The experiment was specifically designed with the purpose to detect muons in heavy ion collisions. Its excellent resolution and rare probe detection capabilities made it possible to measure dileptons with unprecedented accuracy at SPS energies of 158 AGeV.

The general layout is shown schematically in Fig. 5.4. The first detector is a beam tracker, which is positioned before the target. The target itself and the vertex tracker right behind it are located in a 2.5T magnetic field, produced by a dipole magnet surrounding the tracking device. After this first part of the tracking a hadron absorber is positioned. As shown schematically in Fig. 5.4 the muon tracks (yellow) pass the absorber, the other tracks (red, black) are being stopped in the absorber (a 5.5 meter block of mainly carbon). After the hadron absorber more muon triggering and tracking devices are positioned. The great accuracy of the detector originates in the possibility to connect the tracks from the tracking before absorption and the tracking after the absorption of hadrons. One of the outstanding discoveries of the NA60 collaboration was the broadening of the ρ spectral function, as reported in [A+06b].

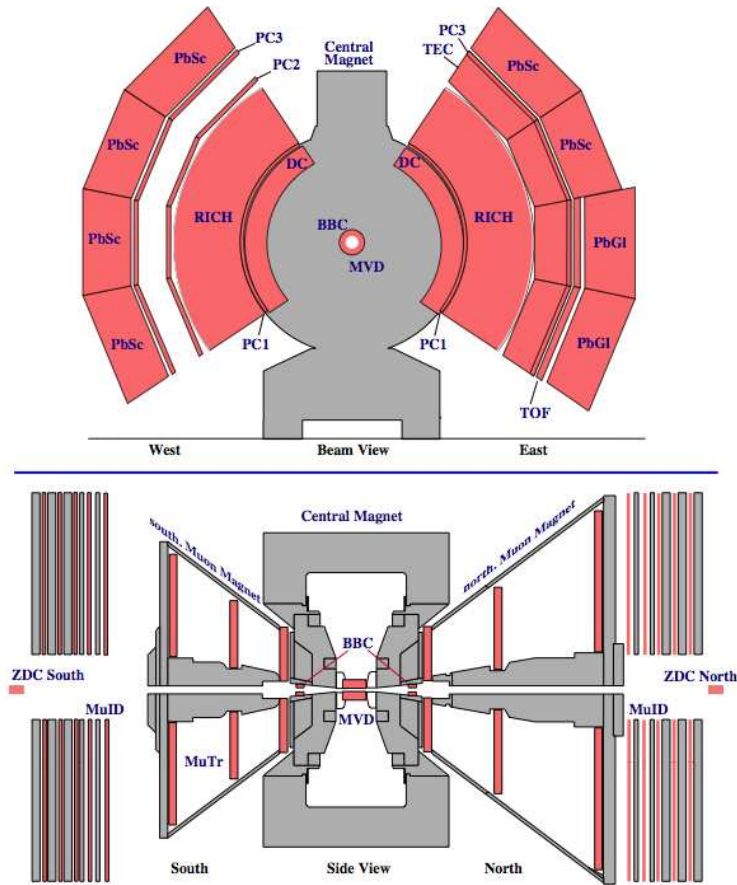


Figure 5.5: Schematic view of the PHENIX experiment. Picture taken from [PHENIX].

5.3 Experiments at high energy

PHENIX

The **P**ioneering **H**igh **E**nergy **N**uclear **I**nteraction **e**Xperiment (PHENIX) (shown schematically in Fig. 5.5) is located at the Relativistic Heavy Ion Collider (RHIC) at the Brookhaven National Lab on Long Island. It is one of the two large experiments at the RHIC (the other being STAR, the two smaller ones BRAHMS and PHOBOS) and was designed to study nuclear matter under extreme conditions, i.e. very large temperature and pressure. It is expected that under the extreme conditions, which are present in

relativistic nuclear collisions at RHIC a new state of matter is formed, which is called the quark gluon plasma.

The detectors are positioned in a multiple arm setup, with two central arms and two muon arms. The first detector in the central arm (as seen from the beamline) are the driftchambers. Those are responsible for measuring the particles momentum and position. The position is more precisely measured in the pad chambers, which are located in the next layer. In the adjacent layer the RICH detectors are positioned, which measure the electrons produced in the collision. In the next layer the two arms differ, while the west arm has two more Pad Chamber detectors, the east arm has a Time Expansion Chamber (TEC), which is responsible for particle identification and momentum measurements.

The final layer of detectors in the central arms are lead scintillators in the west arm, whereas the east arm only is half covered with lead scintillators. The other half is covered with a Time of Flight detector and lead glass detectors right afterwards.

The other two arms are dedicated to the measurement of muons. The main detectors in those two arms are the Muon Tracking Detector, the Muon Identifier and the Muon Piston Calorimeter.

The RHIC program in general was very rich on discovering interesting physics. An extensive list of the discoveries would go beyond the scope of this work, so only a few highlights will be mentioned. The PHENIX collaboration contributed to discoveries regarding the energy loss of high energy particles (jets) in dense matter, investigated the flow pattern of particles created in heavy ion collisions, measured low mass dileptons created in high energy reactions and contributed to the understanding of direct photon physics in nuclear collisions.

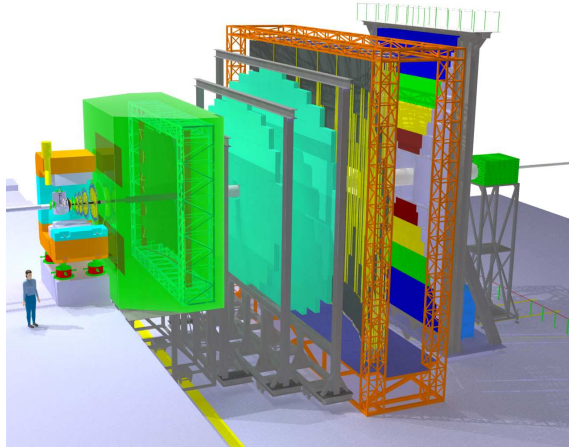


Figure 5.6: Schematic view of the CBM experiment with absorber. Picture taken from [CBM].

5.4 Future experiments

CBM

The CBM (**C**ompressed **B**aryonic **M**atter) experiment is located at the FAIR facility and is expected to have a first beamtime roughly in 2015. It is planned as a fixed-target experiment. Its main goals are performing an excessive energy scan in the energy region where the baryon density is highest. This is a complementary approach to the LHC and RHIC physics, where the goal is to reach high temperatures at low baryon density.

The great advantage of the CBM experiment is that it will be able to investigate hadronic as well as leptonic decay channels. Currently two different setups are planned, which are depicted in Fig. 5.6 and 5.7. Fig. 5.6 shows the setup, which will be used for measuring electrons. It shows a micro vertex detector in the target region, which is surrounded by a dipole magnet. The next detector in line is the Silicon Tracking System, followed by a Ring Imaging Cherenkov Detector (RICH), which is responsible for electron identification. Followed by that are the Transition Radiation Detectors (TRD) and a Time-Of-Flight Wall (TOF). The final detectors in the setup for elec-

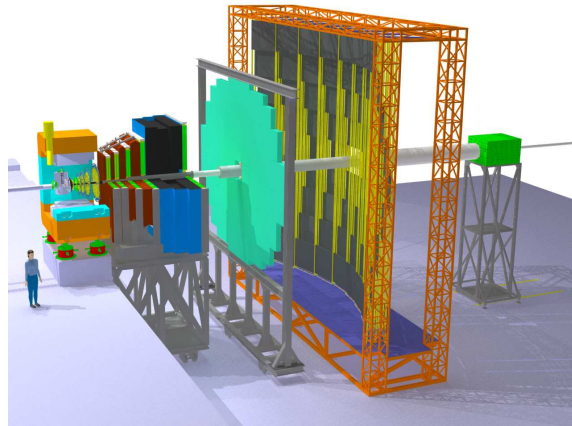


Figure 5.7: Schematic view of the CBM experiment without absorber. Picture taken from [CBM].

trons are an electromagnetic calorimeter (EMCAL) and a Projectile-Spectator Detector, which in that case is a Zero-Degree-Calorimeter (ZDC).

The second setup is designed to investigate the muonic decay channels of resonances and is depicted in Fig. 5.7.

The first three parts of the experiment are exactly identical to the electron setup, namely the Micro-Vertex-Detector, the Dipole Magnet and the Silicon Tracking System. However, since muons have a longer mean free path in material the RICH is replaced by a Muon Detection System with a dedicated tracking system attached. One important task of the muon detection system is to filter out the hadrons, which is usually done by hadron absorbers, in the case of CBM a meter-wide iron absorber. This system is being followed by the Time-Of-Flight Wall and the Zero-Degree-Calorimeter, just as in the electron setup.

The idea of having two different setups in one experiment is the possibility to exchange certain parts of it and measure electrons and muons in the same experiment. This will have the advantage that one can cross check results within the same experimental setup and thus reduces systematic errors.

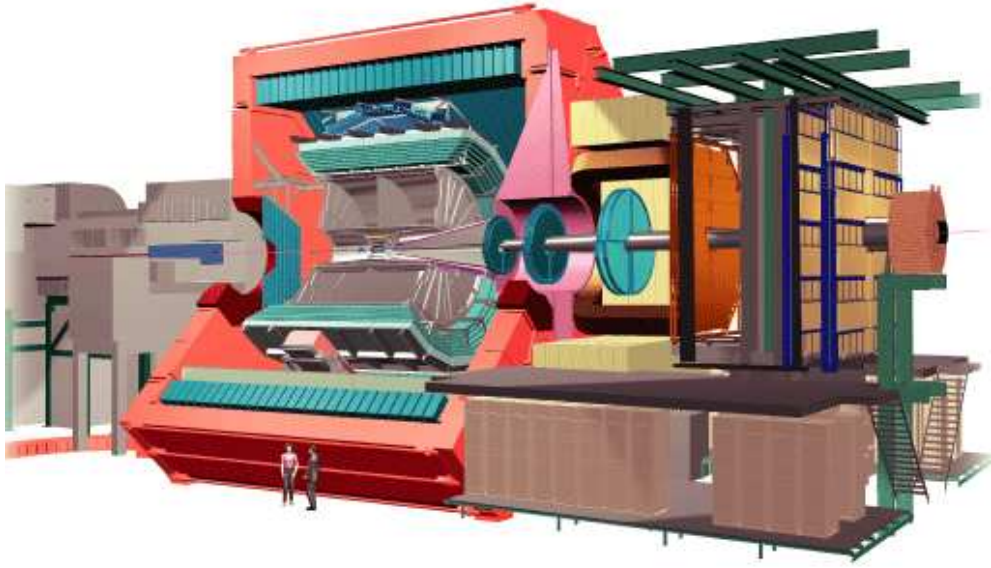


Figure 5.8: Schematic view of the ALICE experiment. Picture taken from [ALICE].

ALICE

Although not a heavy ion collider by design the LHC has a heavy ion program with one designated heavy ion detector. The ALICE (**A Large Ion Collider Experiment**) experiment is a multi-purpose heavy ion experiment with a broad range of possible measurements, thus allowing to measure various observables within one experiment. We will only highlight several of the detectors used in this experiment, which is schematically shown in Fig. 5.8. For more information please refer to the technical design reports, which can be found at [ALICE].

The experiment is partially embedded into the L3 magnet. The innermost detector is the Inner Tracking System (ITS), which is responsible for the detection of primary and secondary vertices. The detector surrounding the ITS is the Time Projection Chamber (TPC), which is one of the central detectors in the ALICE experiment. It measures (via the energy loss per length) the particle type, as well as the momentum of the particles. Directly adjacent to the TPC is the Transition Radiation Detector (TRD). This

detector is mainly responsible for the distinction of pions and electrons. The next detector is the Time of Flight Wall (TOF), which measures the particle speed. Since the momentum is already known from the measurement in the TPC, one can calculate particle properties with that knowledge, e.g. the mass of the particle. The next layer of detectors is split into several system, thus each covers a smaller solid angle than the detectors mentioned before. The High Momentum Particle Identification (HMPID) is a detector which is responsible for the measurement of high momentum particles, in the momentum range, which is not covered by the other detectors.

The Photon Spectrometer is roughly the same distance away from the collision point, and is an electromagnetic calorimeter for the measurement of direct photons and photons from decays. Shown on the right in Fig. 5.8 are the muon chambers and the muon triggering system. As also discussed in the experiments above the ALICE experiment also features a ZDC, which will measure the spectator nucleons and thus will give a measure of the centrality of the collision.

The ALICE experiment is currently in the phase of commissioning and will be operational once the LHC program starts.

— *Do not put too much confidence in experimental results until they have been confirmed by theory.*

Sir Arthur Eddington

6

Theoretical Models for Heavy Ion Collisions

The governing theory for strongly interaction systems is Quantum Chromo Dynamics. However, due to the complexity of the system in a heavy ion collision one cannot solve the equations of motion exactly. This holds true even for low energy collisions. It is therefore necessary to simplify the equations in order to make sure they remain solvable.

Therefore models are applied and usually numerically realized to simulate the collision and gather information about the dynamics and physical quantities of the system created and evolving in such collisions. It is no trivial task to find the model which is most suitable for the problem at hand. Different models emphasize different aspects of physics, however they also

neglect different aspects of physics. Thus the choice of the approximation is an important one, since there is so far no kind of theoretical investigation which models the complexity of a heavy ion collision without any approximation.

Three different and commonly used types of such models are:

- Statistical Models
- Hydrodynamical Models
- Transport Models

In the following we will describe the main features of all 3 models very briefly and then focus on a more detailed description of the model used for this work, the UrQMD transport approach.

6.1 Statistical models

Thermodynamical, or statistical models assume particle emission from a thermally equilibrated source and therefore neglect the non-equilibrium-dynamics of a heavy ion collision. Thus they might be suitable to describe bulk features of such collisions, such as yields, ratios of yields and so on, however they are unsuitable to describe dynamical quantities, such as time evolutions or the dynamics of resonances in a heavy ion collision.

The most commonly used statistical model describes the system as a grand-canonical ensemble of non-interacting particles in equilibrium at a given freeze-out temperature T . For an infinite volume the particle densities are given by

$$n_i = \frac{g_i}{2\pi^2} \int_0^\infty \frac{p^2 dp}{e^{(E_i(p)-\mu_i)/T} \pm 1} \quad (6.1)$$

with n_i being the particle density, g_i the spin degeneracy factor, p the momentum and E the energy. The temperature T and the chemical potential μ are the two parameters of the model to describe particle ratios. Since equation 6.1 assumes the infinite volume limit, which might not given in a heavy ion collision, this model usually calculates ratios of particles, since in that case the volume cancels.

The thermal model has been applied to various energies and collision systems over the years, ranging from e^+e^- reactions over proton-proton interaction on to heavy ion collisions. It is surprising that a single approach assuming a thermalized system can describe experimental data in a centrality range from elementary to most central heavy ion collisions. One should however note that these kind of models are giving a much better description of data for stable particles (like protons, pions and the like) than compared to resonances. Thus they are less suitable for the investigation of the dynamics and evolution of resonant states and are mostly used to provide estimates to average temperatures and chemical potentials of heavy ion collisions.

For a (non-complete) list results of those models, please refer to [CORW06, ABBM+08, BMSWX95, BMSWX96, CSSO90, DMQC91, DMO91, CS93, LRT94, KTBF06, DMOR92, CR99] and references therein.

Let us further stress the point of treatment of resonances in those models. As an example we will follow the line of argument of [TR01, TR03, S03, TR04].

The starting point of resonance calculations within the statistical model to assume that the particles (it is assumed that their masses is higher than the

average temperature of the system, which is true for all resonances) fill the available phase space of the form of the relativistic Boltzmann distribution

$$\frac{d^2 N}{dm_T^2 dY} \propto g \prod_{i=1}^n \lambda_i \gamma_i m_T \cosh(y) e^{-E/T}, \quad (6.2)$$

where g is the degeneracy factor, λ_i denotes the fugacity, γ_i denotes the so-called phase space occupancy parameter for the quarks. E is the energy, whereas T describes the temperature. On the l.h.s. m_T describes the transverse mass of the particles and Y is the rapidity. When considering ratios of the type $K^*(892)/K$ or Λ^*/Λ , where the chemical composition of the particles involved in the ratio is the same one can neglect the fugacity and the equilibrium parameters.

Let us now check the decay products of resonances. We assume we have a decay like $R \rightarrow 1 + 2$, where R is the resonance and 1 and 2 are the decay products. Knowing the distribution of the resonances (with the properties M , M_T , Y) one can derive the properties of their decay products (with the properties m , m_T and y for particle 1 and m_2 for particle 2) as shown in the following (for more information we refer to [TR01]):

$$\frac{dN_1}{dm_T^2 dy} = \frac{g_r b}{4\pi p^*} \int_{Y^-}^{Y^+} dY \int_{M_T^-}^{M_T^+} dM_T^2 J \frac{d^2 N_R}{dM_T^2 dY}$$

$$J = \frac{M}{\sqrt{P_T^2 p_T^2 - (ME^* - M_T m_T \cosh \Delta Y)^2}} \quad (6.3)$$

g_r labels the degeneracy factor of the resonance, whereas b label the relevant branching ratio into the relevant decay channel. ΔY denotes the difference of the resonance rapidity = $Y - y$, \sqrt{s} is the combined invariant mass of all decay products except the one labelled 1. $E^* = \frac{1}{2M}(M^2 - m^2 - m_2^2)$ and $p^* = \sqrt{E^{*2} - m^2}$ are the energy and momentum of the first decay particle in the resonance rest frame.

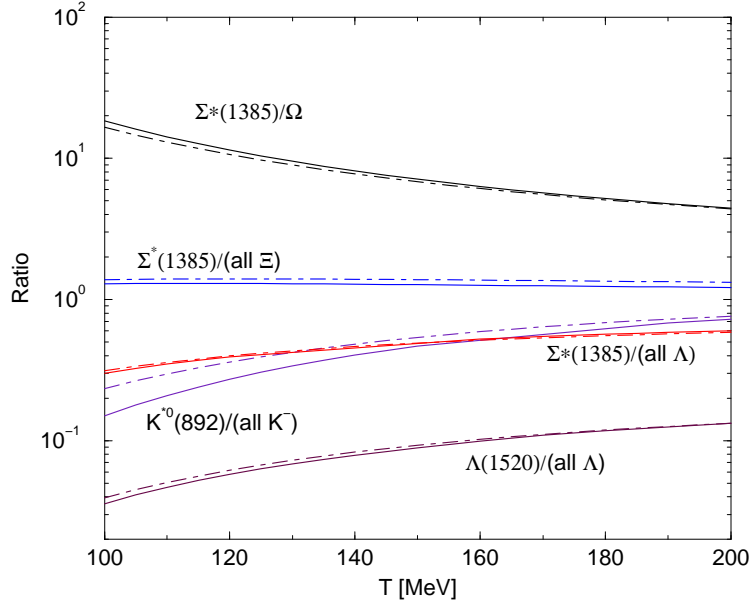


Figure 6.1: Thermal particle ratios at production as a function of temperature. Dashed lines depict the same ratios within a central rapidity interval of $\Delta y = \pm 0.5$. Taken from [TR01].

For further information on the exact details of the integration procedure we refer to [SSU93, AKNS85].

Fig. 6.1 depicts the ratio of resonances to non resonance contribution for several combinations as a function of temperature. The focus in this analysis (taken from [TR01]) is on strange resonances. One observes that the general trend is very much dependent on the ratio observed. Whereas the Σ^*/Ω ratio decreases as a function of temperature the Σ^*/Ξ ratio stays rather constant. All other ratios increase as a function of temperature. Note however, that these ratios are without the effect of rescattering. Those are the pure statistical ratios calculated in this approach at the point of production. The observed (in this thesis called reconstructable) ratios differ depending on centrality, time of the hadronic evolution etc.

In order to estimate the effect of rescattering the authors of [TR01] argue the following: Consider the decay of the (generic) resonance N^* in a gas of nucleons or pions with the decay product labeled as p_1 and p_2 .

$$N^* \rightarrow p_1 p_2 \quad (6.4)$$

The chance to reconstruct the resonance in an invariant mass analysis depends upon the probability that both decay products leave the reaction zone undisturbed. If one of the decay products scatter in the further evolution of the system the resonance signal is lost. These interaction depend on the cross section of the decay product with the relevant particles (here pions, nucleons and antinucleons are considered), the density and the speed of the decay particle relative to the typical fireball particles.

The reaction rate is then

$$P_{1/2} = (\sigma_{1/2\pi}\rho_\pi + \sigma_{1/2N}\rho_N + \sigma_{1/2\bar{N}}\rho_{\bar{N}})\left(\frac{R}{R+vt}\right)^3\langle v \rangle, \quad (6.5)$$

where σ denotes the cross section of particle 1 or 2 with the given particle of the fireball, ρ denotes the density of the fireball particles, R is the fireball radius at hadronization and v is the averaged flow velocity. Note that the cross section are energy averaged, which is not applicable if one of the decay particles is for example a pion. Here the cross section with nucleons and other pions is very much energy-dependent, since the resonant production of Δ baryons and ρ mesons are heavily dependent on energy.

To estimate the relevant densities the relativistic Boltzmann approximation is used, thus the nucleon density is given by

$$\rho_N = \frac{g}{(2\pi\hbar c)^3} 4\pi m^2 (\lambda_q \gamma_q)^3 T K_2\left(\frac{m}{T}\right) \quad (6.6)$$

and the pion density is given in the massless particle limit

$$\rho_\pi = \frac{A\pi^2}{90}T^3. \quad (6.7)$$

Here, $K_2(\frac{m}{T})$ is the second modified Bessel function, the factor A is an effective degeneracy factor, which is used to fix the entropy of the system and especially of the baryons.

The temperature and the size of the fireball are tightly connected, the larger the fireball, the lower the temperature. This behavior is modeled such, that the size of the fireball is given by

$$R = 8 fm \cdot 145/T[\text{MeV}]. \quad (6.8)$$

The population equations for the scattering loss abundance N_i are given in [TR01] with P_i given as in equation 6.5 :

$$\begin{aligned} \frac{dN_i}{dt} &= \frac{1}{\tau}N_{N^*} - N_iP_i, \quad i = 1, 2 \\ \frac{dN_{N^*}}{dt} &= -\frac{1}{\tau}N_{N^*}, \end{aligned} \quad (6.9)$$

Figure 6.2 depicts the observable particle ratio as a function of temperature for different values of the lifetime of the phase of hadronic rescattering. Shown are the ratios $\Lambda^*(1520) / \text{all } \Lambda$, $\Sigma^*(1385) / \text{all } \Lambda$ and $K^{*0} / \text{all } K^-$. The problem of this way of presenting the ratios is that the explanation can be manifold. Assuming you trust to model enough to confront the calculations with experimental data, you will have several values of temperature and lifetime of the hadronic evolution which will fit that one value. In order to pin down the relevant temperatures and lifetimes you have to measure several ratios and compare them with experimental values. This is however beyond the scope of this thesis and we refer to the relevant publications [TR01, TR03, S03, TR04] and references therein.

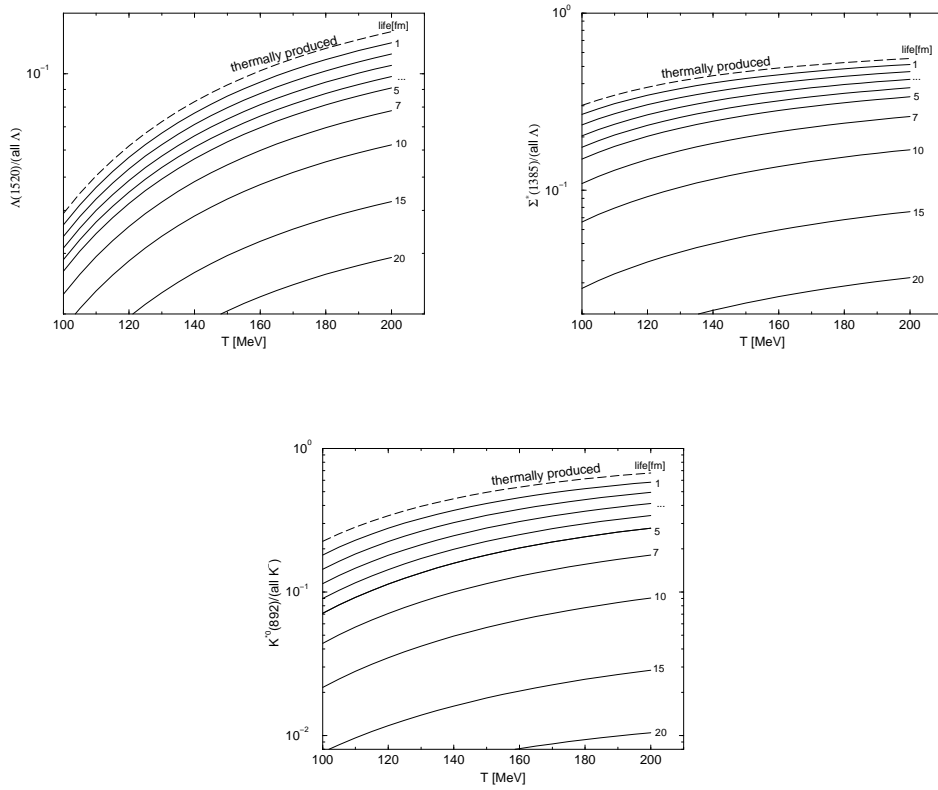


Figure 6.2: Observable particle ratios (top left: $\Lambda^*(1520) / \text{all } \Lambda$, top right: $\Sigma^*(1385) / \text{all } \Lambda$, bottom: $K^{*0} / \text{all } K^-$) as a function of temperature. The different lines depict different evolution times after chemical freeze-out, the time of that phase is given in fm/c. Taken from [TR01].

6.2 Hydrodynamics

The properties of nuclei, as well as nuclear fusion and fission is being described by hydrodynamical calculations since the early stages of this field of science. The description of nuclear reactions with these methods date back to the 1950's, however the application to heavy ion reactions started in the 1980's (see e.g. [CS81, TW80, BFB+83, KRR83]).

The basic assumption of hydrodynamics are the conservation laws in their covariant form

$$\partial_\mu N^\mu = 0 \quad (\text{charge conservation}) \quad (6.10)$$

$$\partial_\mu T^{\mu\nu} = 0 \quad (\text{energy-momentum conservation}) \quad (6.11)$$

$$\partial_\mu S^\mu \geq 0 \quad (\text{2nd law of thermodynamics}). \quad (6.12)$$

In ideal hydrodynamics a local thermal equilibrium is assumed, i.e. $f(x, p) = f_{eq}(x, p)$, with f being the distribution function of particles. The energy momentum tensor and the charge then reads as follows

$$T^{\mu\nu} = \frac{1}{(2\pi)^3} \int \frac{d^3p}{E} p^\mu p^\nu f(x, p) \quad (6.13)$$

$$= (\epsilon + p)u^\mu u^\nu - pg^{\mu\nu} \quad (6.14)$$

$$N^\mu = \frac{1}{(2\pi)^3} \int \frac{d^3p}{E} p^\mu f(x, p) \quad (6.15)$$

$$= nu^\mu \quad (6.16)$$

with u^μ being the fluid velocity, p being the pressure and ϵ being the energy density. Together with the first law of thermodynamics $Ts = p - \mu n + \epsilon$ (which is valid, since a local thermal equilibrium is assumed), it follows that the entropy is conserved. In contrast to ideal hydrodynamics fluids with non-

vanishing viscosity are described by the theory of non-ideal hydrodynamics. The conservation laws still apply, however the distribution function is shifted from its equilibrium value

$$f(x, p) = f_{eq}(x, p) + \delta f(x, p). \quad (6.17)$$

Consequently terms to describe viscosities (bulk and shear viscosity), entropy production and more are coming into play.

Describing the models in detail or even giving an exhaustive list of references would go beyond the scope of this thesis, so for more information the reader is referred to [KH03] and references therein.

6.3 Transport models

Since statistical and hydrodynamical models of heavy ion reactions only describe bulk properties of the collisions it would be appealing to have an approach which models the individual particles and their momenta and positions (and of course all other relevant information) and also provides the information on binary collisions themselves. This kind of approach has been developed under the framework of transport theory and thus is usually referred to as a transport approach. Transport approaches rely on the solution of the covariant Boltzmann equation, usually in some kind of approximation (one of them, the QMD approach, will be discussed in the following section). Currently used models are for example

- HSD [CB99]
- RQMD [S+92]
- UrQMD [B+98, B+99]
- AMPT [LKL+05]

- BAMPS [XG05]
- ZPC [Z98]
- MPC [MG00]

where the latter three are parton cascade models, which model parton dynamics rather than hadron dynamics. However, the general features still apply to them.

The most basic transport equation is the Vlasov equation, which reads

$$Df(\vec{r}, \vec{v}, t) = \frac{\partial f}{\partial t} + \vec{v} \frac{\partial f}{\partial \vec{r}} + \frac{\vec{F}}{m} \frac{\partial f}{\partial \vec{v}} = 0 \quad (6.18)$$

where $f(\vec{r}, \vec{v}, t)$ is the phase space density and \vec{F} an outer force, e.g. an electromagnetic field. This equation has no term describing collisions, so it is not adequate to apply it in a heavy ion transport model. But it is of importance to obtain it as a classical limit without collisions.

The next step is to include collisions, which is done by the collision term, usually referred to as I_{coll} , which will be discussed in the following.

The Vlasov equation with the collision term then becomes the Boltzmann equation, which reads

$$\frac{\partial f}{\partial t} + \vec{v} \frac{\partial f}{\partial \vec{r}} + \frac{\vec{F}}{m} \frac{\partial f}{\partial \vec{v}} = I_{coll}, \quad (6.19)$$

and can be rewritten as

$$\frac{\partial f}{\partial t} + \vec{v} \frac{\partial f}{\partial \vec{r}} + \frac{\vec{F}}{m} \frac{\partial f}{\partial \vec{v}} = \int \int (f' f'_1 - f f_1) |\vec{v} - \vec{v}_1| \frac{d\sigma}{d\Omega'}(\vec{v}, \vec{v}') d\Omega' d^3 v_1 \quad (6.20)$$

where f and f_1 are the phase space densities, σ the cross section between the target and projectile particle and Ω the solid angle.

This equation is still purely classical and has not built in any quantum mechanical effect.

Contrary to hydrodynamics, where it is assumed that the mean free path is 0, the assumed mean free path in transport theory (without collision term) is infinity. This is certainly not fully applicable if one includes a collision term and the mean free path highly depends on the colliding nuclei, the centrality and the beam energy. However, it is valid to a good approximation.

6.4 UrQMD

In this section an overview over the UrQMD-model is given. For more details please refer to [B+98, B+99]. Before describing this specific model in detail a brief review on the Quantum Molecular Dynamics (QMD) approach is given. For more information on that particular approach we refer to [A86, A91]. In the QMD approach each nucleon is represented by a gaussian wave packet, given by the following expression:

$$\phi_i(\vec{x}; \vec{q}_i, \vec{p}_i, t) = \left(\frac{2}{L\pi} \right)^{3/4} \exp \left\{ -\frac{2}{L} (\vec{x} - \vec{q}_i(t))^2 + \frac{1}{\hbar} i \vec{p}_i(t) \vec{x} \right\} \quad (6.21)$$

The parameter L describes the spatial extension of the wave packet, \vec{q}_i and \vec{p}_i are the time-dependent parameters of the equation. The total n -body wave function is then the product of the coherent states:

$$\Phi = \prod_i \phi_i(\vec{x}, \vec{q}_i, \vec{p}_i, t) \quad (6.22)$$

With the Hamilton operator of the form

$$H = \sum_i T_i + \frac{1}{2} \sum_{ij} V_{ij} \quad (6.23)$$

and $\langle V_{ij} \rangle$ being the potential of the form $\langle V_{ij} \rangle = \int d^3x_1 d^3x_2 \phi_i^* \phi_j^* V(x_1, x_2) \phi_i \phi_j$ the Lagrangian and the equations of motions then read

$$\mathcal{L} = \sum_i \left[-\dot{\vec{q}}_i \vec{p}_i - T_i - \frac{1}{2} \sum_{j \neq i} \langle V_{ik} \rangle - \frac{3}{2Lm} \right] \quad (6.24)$$

$$\dot{\vec{q}}_i = \frac{\vec{p}_i}{m} + \nabla_{\vec{p}_i} \sum_j \langle V_{ij} \rangle = \nabla_{\vec{p}_i} \langle H \rangle \quad (6.25)$$

$$\dot{\vec{p}}_i = -\nabla_{\vec{q}_i} \sum_{j \neq i} \langle V_{ij} \rangle = -\nabla_{\vec{q}_i} \langle H \rangle. \quad (6.26)$$

These are the equations of motion which need to be solved numerically. Instead of the time evolution of a complicated n-body Schrödinger equation the problem is reduced to $6(N_P + N_T)$ equations, where N_P and N_T are the numbers of projectile and target nuclei respectively. Although it is easier than compared to solving the full n-body Schrödinger equation it still is a complicated task, which is very time-consuming, especially when calculating the collision of large nuclei at high energies.

In general, the UrQMD approach can be broken down into three pieces.

- Initialising of the initial state (mostly 2 nuclei)
- Propagation of the nucleons and the produced particles
- Realisation of the binary scatterings and decay of the non-stable particles

The initial conditions for nucleus nucleus collision are set by two Wood-Saxon-distributions “filled” with the respective nucleons. After the initialization the actual collisions occur.

Within the UrQMD approach all particles will be propagated to the next collision (or decay) and then the collision term will be evaluated. According to the collision term and the cross sections for the specific binary scatterings new particles are produced, particles change their momentum etc. After that the next reaction will be calculated, all particles will be propagated to the according points in space and time and again the collision term will be evaluated. This goes on until the (user-given) final time or until no more collisions happen and all particles can propagate freely. This method allows a fine grating in time without defining any time-steps. The advantages are that one does not omit collisions because the time-steps are chosen too large and one does not waste computing time when no collisions take place (which might happen in an approach with pre-defined time-steps). For details on the collision term please refer to [B+98, B+99] The collision criterium itself is purely geometrical and reads:

$$\pi d^2 \leq \sigma_{tot} \tag{6.27}$$

which means that the distance d between the two particles in the two particle frame has to be less than the total cross section, which is the classical definition of the cross section. One problem of this method is, that one might still omit collisions. As shown in [KBH+95] the time ordering of the collisions will be dependent on the reference frame. One can solve this problem with a 8+1 dimensional covariant dynamics like for example in the RQMD model [SSG89]. In the UrQMD model the problem is addressed by an invariant formulation of the collision criterium.

6.4.1 Particle species

In order to get a quantitative description of heavy ion collisions it is important to include as many known particle types as possible. Therefore all measured baryons included in the Particle Data Book in its version of 1996 [B+96] up to a mass of 2.25 GeV are taken into account.

Of course the implementation of this many particles leads to several problems. The higher mass resonances are measured only with quite poor statistics and therefore the error bars are very large. Following from that the choice of the parameters is not unambiguous within the experimental error bars. Also one has to use certain approximations on production cross sections, because of the uncertainty in the experimental data. Therefore assumptions are used, e.g. that the matrix elements for non-strange baryon resonances can be divided into 6 classes: $NN \rightarrow N\Delta_{1232}$, $NN \rightarrow NN^*$, $NN \rightarrow N\Delta^*$, $NN \rightarrow \Delta_{1232}\Delta_{1232}$, $NN \rightarrow \Delta_{1232}N^*$ and $NN \rightarrow \Delta_{1232}\Delta^*$, where Δ^* denotes higher resonances of the Δ_{1232} .

Particle production in UrQMD is realized by resonance excitations and decay of resonances and at higher energies via string excitation and fragmentation. The included particles are listed in tables 6.1 and 6.2. In addition to those particles all antiparticle states are implemented as well. More details on particle production and particle species can be found in [B+98, B+99].

nucleon	Δ	Λ	Σ	Ξ	Ω
N_{938}	Δ_{1232}	Λ_{1116}	Σ_{1192}	Ξ_{1317}	Ω_{1672}
N_{1440}	Δ_{1600}	Λ_{1405}	Σ_{1385}	Ξ_{1530}	
N_{1520}	Δ_{1620}	Λ_{1520}	Σ_{1660}	Ξ_{1690}	
N_{1535}	Δ_{1700}	Λ_{1600}	Σ_{1670}	Ξ_{1820}	
N_{1650}	Δ_{1900}	Λ_{1670}	Σ_{1775}	Ξ_{1950}	
N_{1675}	Δ_{1905}	Λ_{1690}	Σ_{1790}	Ξ_{2025}	
N_{1680}	Δ_{1910}	Λ_{1800}	Σ_{1915}		
N_{1700}	Δ_{1920}	Λ_{1810}	Σ_{1940}		
N_{1710}	Δ_{1930}	Λ_{1820}	Σ_{2030}		
N_{1720}	Δ_{1950}	Λ_{1830}			
N_{1900}		Λ_{1890}			
N_{1990}		Λ_{2100}			
N_{2080}		Λ_{2110}			
N_{2190}					
N_{2200}					
N_{2250}					

Table 6.1: Included Baryons in UrQMD. All baryons in the Particle Data Book up to a mass of 2.25 GeV are built in.

0^{-+}	1^{--}	0^{++}	1^{++}
π	ρ	a_0	a_1
K	K^*	K_0^*	K_1^*
η	ω	f_0	f_1
η'	ϕ	f_0^*	f_1'
1^{+-}	2^{++}	$(1^{--})^*$	$(1^{--})^{**}$
b_1	a_2	ρ_{1450}	ρ_{1700}
K_1	K_2^*	K_{1410}^*	K_{1680}^*
h_1	f_2	ω_{1420}	ω_{1662}
h_1'	f_2'	ϕ_{1680}	ϕ_{1900}

Table 6.2: Mesons included in UrQMD, sorted according to spin, parity and c-parity

6.4.2 Cross sections

Whenever possible total cross sections are implemented by parametrizing experimental data. Therefore one can normalize the sum of the partial ones to the sometimes better known total cross section. For several reactions the cross sections are not explicitly measured or parametrized. In that case it can be derived using the following principles.

- **Isospin invariance:**

Strong interaction is independent under change of isospin of the particles. For example $\sigma(n + \pi^- \rightarrow \Delta^-)$ and $\sigma(p + \pi^+ \rightarrow \Delta^{++})$ are equal.

- **Detailed balance:**

By stating that the matrix element is invariant under exchange of the final and initial state ($|M_{fi}| = |M_{if}|$) one can calculate (see for example [P87]) the cross section for the reaction $C+D \rightarrow A+B$ if the cross section for the reaction $A+B \rightarrow C+D$ is known.

One obtains

$$\sigma(C + D \rightarrow A + B) = \frac{\langle p_{AB}^2 \rangle}{\langle p_{CD}^2 \rangle} \frac{g_A g_B}{g_C g_D} \sigma(A + B \rightarrow C + D) \quad (6.28)$$

where g_A and g_B denote degeneracy factors for spin and isospin and $\langle p^2 \rangle$ is the momentum of the particles in the equal momentum frame. One problem with detailed balance occurs, since UrQMD treats only binary collisions. This leads to a violation of detailed balance in many-body-decays (e.g. $2 \rightarrow 3$ processes), where there is no back-reaction channel implemented.

- **Hadron universality - additive quark model:**

The additive quark model [BZK71] states, that the cross section for particle production at high energies is nearly independent of the hadron

species and only depends on the quark content of the scattering particles. The total cross section is then given as (in mb)

$$\sigma_{total} = 40 \cdot \left(\frac{2}{3}\right)^{n_M} \cdot (1 - 0.4n_1^s)(1 - 0.4n_2^s) \quad (6.29)$$

with n_M as the number of incoming mesons and n^s as the ratio of strange to non-strange quarks in the first or second hadron. Of course this model is no longer applicable at threshold energies and totally breaks down for resonance production, since the cross section is energy dependent. But for very large center of mass energies it is in reasonable agreement to experimental data.

Another application of the additive quark model is to rescale cross sections. If for example the cross section σ_{CD} is known one can approximate the cross section σ_{AB} with

$$\sigma_{AB}(\sqrt{s}) = \sigma_{CD} \frac{\sigma_{AB}^{aqm}}{\sigma_{CD}^{aqm}} \quad (6.30)$$

6.4.3 Meson production and resonance decays

In the UrQMD model the formation of most light mesons at low energies is modeled as a multi-step process that proceeds via intermediate heavy baryon and meson resonances and their subsequent decay. The probability for a resonance to decay into a specific channel is determined by the branching ratio, i.e. by the ratio between the partial decay width for the decay into the exit channel and the total decay width of the resonance, both of which depend on the resonance running mass. In the UrQMD model, the full decay width $\Gamma_{tot}(M)$ of a resonance is defined as the sum of all partial decay widths and depends on the mass of the excited resonance:

$$\Gamma_{tot}(M) = \sum_{br=\{i,j\}}^{N_{br}} \Gamma_{i,j}(\mu) \quad . \quad (6.31)$$

The partial decay widths $\Gamma_{i,j}(\mu)$ for the decay into the exit channel with particles i and j is given by:

$$\Gamma_{i,j}(\mu) = \Gamma_R^{i,j} \frac{\mu_R}{\mu} \left(\frac{\langle p_{i,j}(\mu) \rangle}{\langle p_{i,j}(\mu_R) \rangle} \right)^{2l+1} \frac{1.2}{1 + 0.2 \left(\frac{\langle p_{i,j}(\mu) \rangle}{\langle p_{i,j}(\mu_R) \rangle} \right)^{2l}} , \quad (6.32)$$

here μ_R denotes the pole mass of the resonance, $\Gamma_R^{i,j}$ its partial decay width into the channel i and j at the pole and l the decay angular momentum of the exit channel; $\langle p_{i,j}(M) \rangle$ is the momentum of the decay products in the rest frame of the resonance. If the outgoing particles are stable particles with a well-defined mass, then $\langle p_{i,j} \rangle$ coincides with the standard momentum of the decay products in the rest frame of the resonance. If the outgoing particles are resonances, the width of their mass distribution is taken into account and $\langle p_{i,j} \rangle$ is determined as integral over the mass distribution of the respective resonance. For further details we refer to [B+98]. The resonance parameters (pole masses, total and partial decay widths at the pole) are within the limits of [Y+06]. However, in many cases only crude estimates for $\Gamma_R^{i,j}$ are given in [Y+06]. For non-strange baryon-resonances, all masses, full widths and decay probabilities used in UrQMDv2.3 are listed in table 6.3 and have been fixed along the years.

Baryon resonances can be produced both in baryon-baryon and meson-baryon collisions. For the baryon-baryon cross sections an effective parametrization based on simple phase space considerations is used; the cross section has the general form:

$$\sigma_{1,2 \rightarrow 3,4}(\sqrt{s}) \sim (2S_3 + 1)(2S_4 + 1) \frac{\langle p_{3,4} \rangle}{\langle p_{1,2} \rangle} \frac{1}{(\sqrt{s})^2} |\mathcal{M}(m_3, m_4)|^2 . \quad (6.33)$$

The matrix element $|\mathcal{M}(m_3, m_4)|^2$ is assumed to have no spin-dependence but may depend on the masses of the outgoing particles. As already noted in Section 6.4.1 the excitation of non-strange baryon resonances is subdivided into 6 classes in the UrQMD approach: $NN \rightarrow N\Delta_{1232}$, $NN \rightarrow NN^*$, $NN \rightarrow N\Delta^*$, $NN \rightarrow \Delta_{1232}\Delta_{1232}$, $NN \rightarrow \Delta_{1232}N^*$ and $NN \rightarrow \Delta_{1232}\Delta^*$.

Here the Δ_{1232} is explicitly listed, whereas higher excitations of the Δ resonance have been denoted as Δ^* . For each of these classes specific assumptions are made with regard to the form of the matrix-element $|\mathcal{M}(m_3, m_4)|^2$; free parameters were tuned to experimental measurements, when available. Form and values of the matrix-element for each class can be found in [B+98]. The cross section depends also on the momenta of the in- and outgoing particles in the two-particle rest-frame $\langle p_{i,j} \rangle$. Again, if the particles are resonances, the width of their mass distribution is taken into account on the determination of $\langle p_{i,j} \rangle$.

Meson-baryon collisions are treated as two-stage processes, i.e. first the meson is absorbed by a nucleon or a baryonic resonance forming a new resonance state with subsequent decay. Meson-baryon cross sections are proportional to the partial decay width of the reverse process; for example, the total meson-baryon cross section for non-strange particles is given by

$$\begin{aligned} \sigma_{tot}^{MB}(\sqrt{s}) &= \sum_{R=\Delta, N^*} \langle j_B, m_B, j_M, m_M \| J_R, M_R \rangle \frac{2S_R + 1}{(2S_B + 1)(2S_M + 1)} \\ &\times \frac{\pi}{p_{CMS}^2} \frac{\Gamma_{R \rightarrow MB} \Gamma_{tot}}{(M_R - \sqrt{s})^2 + \frac{\Gamma_{tot}^2}{4}} \end{aligned} \quad (6.34)$$

with the total and partial \sqrt{s} -dependent decay widths Γ_{tot} and $\Gamma_{R \rightarrow MB}$. Meson final state interactions are assumed to be mediated by the re-excitation of resonances, according to Eq. (6.34).

The cross section for a specific exit channel $MB \rightarrow R \rightarrow M'B'$ can be obtained by replacing the total width Γ_{tot} in Eq. (6.34) by the respective partial decay width $\Gamma_{R \rightarrow M'B'}$. This implies that the full M' production cross section in MB reactions is modelled as an incoherent sum over all resonances of Breit-Wigner type amplitudes. The same approximation has been used in other works [SFF+03, PM01]. The resonance R , however, enters as a dynamical degree of freedom in the UrQMD model; in particular, between creation in $MB \rightarrow R$ and decay $R \rightarrow M'B'$ the resonance is propagated and in medium, can undergo final state interactions. Further details can be

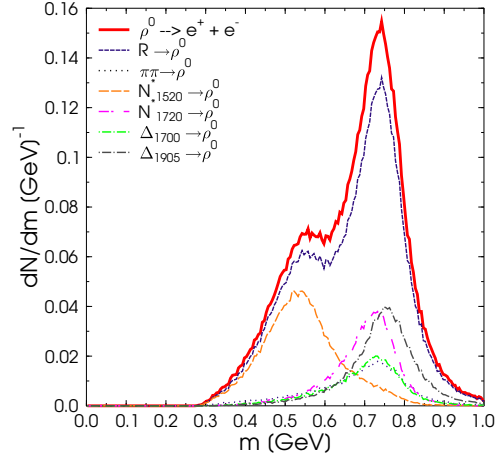


Figure 6.3: ρ meson mass spectrum as an example for baryon resonance contributions. Shown are different contributions from various baryon resonance decays.

found in [B+98]. Analogous considerations yield for meson production in NN collisions.

A comparison between the exclusive and inclusive cross sections for the production of neutral π^0 , η , ρ^0 , ω mesons in pp reactions obtained within the UrQMD model and experimental data can be found in [B+99].

An interesting (and very important feature) regarding resonance decays is the feed-down via specific decay channels. This can be for example shown with the ρ meson mass spectrum. Shown in Fig. 6.3 is such a spectrum for 2 AGeV C+C collisions. Different lines depict different contributions to the spectrum from the respective baryon resonance decays. It is of special importance to include such kinematical effects into theoretical contributions, since they might mimic effects which can be related to different physics, such as the chiral phase transition. Another such effect will be discussed in chapter 8.

CHAPTER 6. THEORETICAL MODELS FOR HEAVY ION COLLISIONS

resonance	mass	width	$N\pi$	$N\eta$	$N\omega$	$N\rho$	$N\pi\pi$	$\Delta_{1232}\pi$	$N_{1440}^*\pi$	ΛK	ΣK	$f_0 N$	$a_0 N$
N_{1440}^*	1.440	350	0.65				0.10	0.25					
N_{1520}^*	1.515	120	0.60			0.15	0.05	0.20					
N_{1535}^*	1.550	140	0.60	0.30			0.05		0.05				
N_{1650}^*	1.645	160	0.60	0.06		0.06	0.04	0.10	0.05	0.07	0.02		
N_{1675}^*	1.675	140	0.40					0.55	0.05				
N_{1680}^*	1.680	140	0.60			0.10	0.10	0.15	0.05				
N_{1700}^*	1.730	150	0.05			0.20	0.30	0.40	0.05				
N_{1710}^*	1.710	500	0.16	0.15		0.05	0.21	0.20	0.10	0.10	0.03		
N_{1720}^*	1.720	550	0.10			0.73	0.05			0.10	0.02		
N_{1900}^*	1.850	350	0.30	0.14	0.39	0.15				0.02			
N_{1990}^*	1.950	500	0.12			0.43	0.19	0.14	0.05	0.03		0.04	
N_{2080}^*	2.000	550	0.42	0.04	0.15	0.12	0.05	0.10		0.12			
N_{2190}^*	2.150	470	0.29			0.24	0.10	0.15	0.05	0.12			
N_{2220}^*	2.220	550	0.29		0.05	0.22	0.17	0.20		0.12			
N_{2250}^*	2.250	470	0.18			0.25	0.20	0.20	0.05	0.12			
Δ_{1232}	1.232	115	1.00										
Δ_{1600}^*	1.700	350	0.10					0.65	0.25				
Δ_{1620}^*	1.675	160	0.15			0.05		0.65	0.15				
Δ_{1700}^*	1.750	350	0.20			0.25		0.55					
Δ_{1900}^*	1.840	260	0.25			0.25		0.25	0.25				
Δ_{1905}^*	1.880	350	0.18			0.80		0.02					
Δ_{1910}^*	1.900	250	0.30			0.10		0.35	0.25				
Δ_{1920}^*	1.920	200	0.27					0.40	0.30	0.03			
Δ_{1930}^*	1.970	350	0.15			0.22		0.20	0.28	0.15			
Δ_{1950}^*	1.990	350	0.38			0.08		0.20	0.18	0.12			0.04

Table 6.3: Masses, widths and branching ratios for non-strange baryon-resonances in UrQMDv2.3. Masses are given in GeV and the widths in MeV.

— *It would be better for the true physics if there were no mathematicians on earth.*

Daniel Bernoulli

7

Resonances as a probe of heavy ion collisions

In order to analyze the interior of a hot and dense environment one needs probes which are sensitive to the medium investigated. Resonances are such a probe. Their properties are sensitive to the medium itself (i.e. its temperature and density). In heavy ion collisions they are produced inside the fireball and, depending on lifetime, might decay in the fireball as well and thus are an ideal probe to study the characteristics of the medium.

This chapter will highlight some of the more recent experimental and theoretical results of studies on resonances. The intention of this chapter is to give a short overview on resonance physics. It is by far not a exhaustive

list of this field of physics, but will rather give some examples of ongoing research of the recent past.

Let us start by pointing out the experimental findings at the Relativistic Heavy Ion Collider (RHIC).

The thermal model (which will be explained in some more detail in chapter 6) is in rather good agreement with the ratios of stable particles which have been measured at RHIC. However, this is not necessarily the case if you compare the experimental results with ratios containing resonances. As seen in Fig. 7.1 a clear deviation is visible.

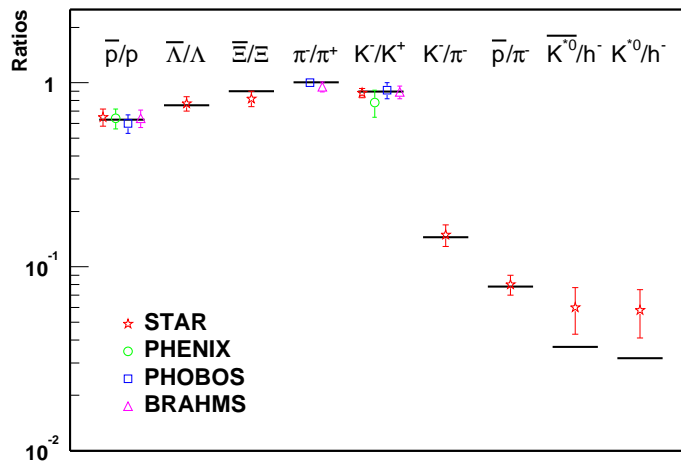


Figure 7.1: Thermal model calculations for particle ratios compared with experimental data from the various RHIC experiments. Figure taken from [BMMRS].

This effect might have several sources. On the hand there is the rescattering of decay products, which makes it hard to give an estimate on the fraction of observable resonances. On the other hand there is an effect which is called regeneration, which states the fact that particles, even after chemi-

cal freezeout can still form resonances. By doing so, they do not change the chemical composition of the system, however correlate particles.

The effect of rescattering can be studied in collisions of different centrality. This has been done by the STAR experiment and the result is presented in Fig. 7.2. One observes a trend towards lower values than the p+p reference. This is not true for the ϕ/K ratio, which has its origin in the long lifetime of the ϕ . There is more evidence for this behavior, for more information we refer to [M08] and references therein.

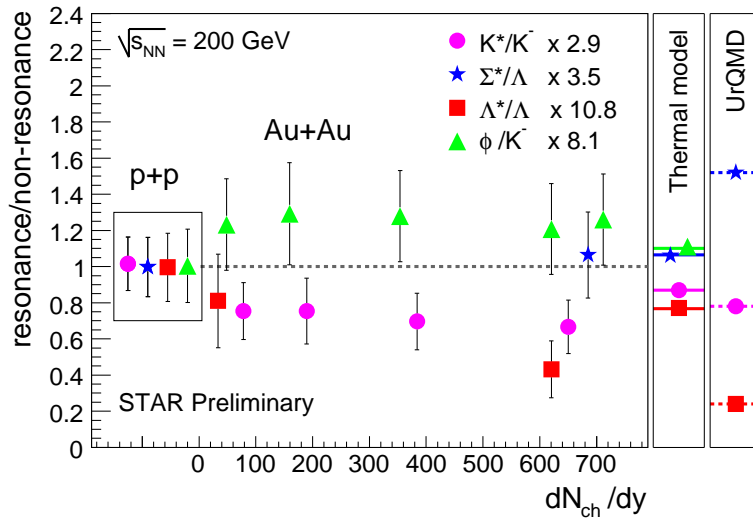


Figure 7.2: Resonance over non-resonance ratio as a function of charged particles of the collision. All data has been normalized to the p+p data. Figure adapted from [M07a].

The analysis of the above mentioned ratios of resonance to non-resonance can shed some light on the dynamics of the collision, for example it can be used to estimate the timespan between the chemical freeze-out (where the chemical composition of the system is fixed) and the thermal freeze-out (where the kinematical variables of the collision are fixed). For more information on that, please refer to [MTR02].

Apart from understanding the dynamics of heavy ion reactions, resonances are a useful tool to probe the medium itself. Especially vector mesons are sensitive to the density and temperature of the surrounding

hadronic medium, a behavior which has been scratched in chapter 3.

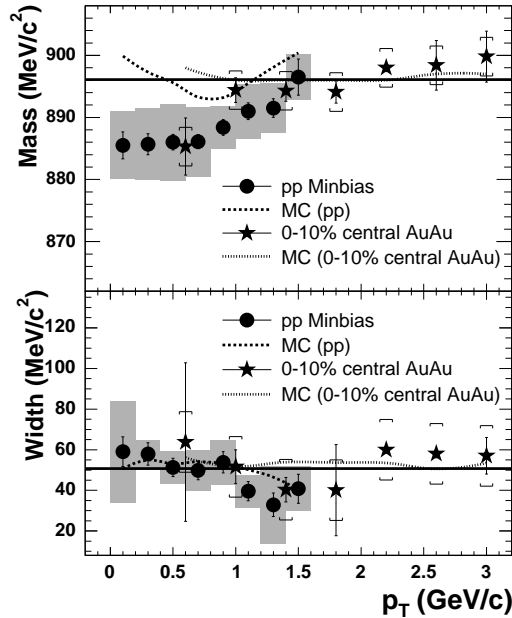


Figure 7.3: K^{*0} meson mass and width as a function of transverse momentum as measured by the STAR experiment. One observes a modification in p+p and peripheral nuclear collisions as compared to the vacuum value. Figure adapted from [A+05a].

Also modification of masses has been measured by the STAR experiment at RHIC (see e.g. [A+05a, A+08a]).

Reported in Fig. 7.3 is the mass (top figure) and the width (bottom figure) of the K^{*0} meson as measured by the STAR collaboration in p+p and peripheral nuclear reactions. One observes a modification in the mass from the vacuum values even in small nuclear systems, which are depicted as the full lines. This modification is especially visible in the low p_T region. The measurements for the width agree within error-bars with the reference value, however the quality of the data is not sufficient to draw any conclusions in any direction.

The STAR experiment (among other experiments at RHIC, which are not mentioned in this brief overview) reconstructed the ρ meson as well. One of

the findings is shown in Fig. 7.4. The investigated collision systems are d-Au and minimum bias and high multiplicity proton proton collisions, depicted is the mass of the ρ^0 . The shaded area indicates the value measured in previous measurements of the NA27 collaboration [A+91]. Even in those small systems one observes a change in the meson mass as function of transverse momentum, which certainly attributes to either dynamical effects or medium-induced changes in the properties of the particles.

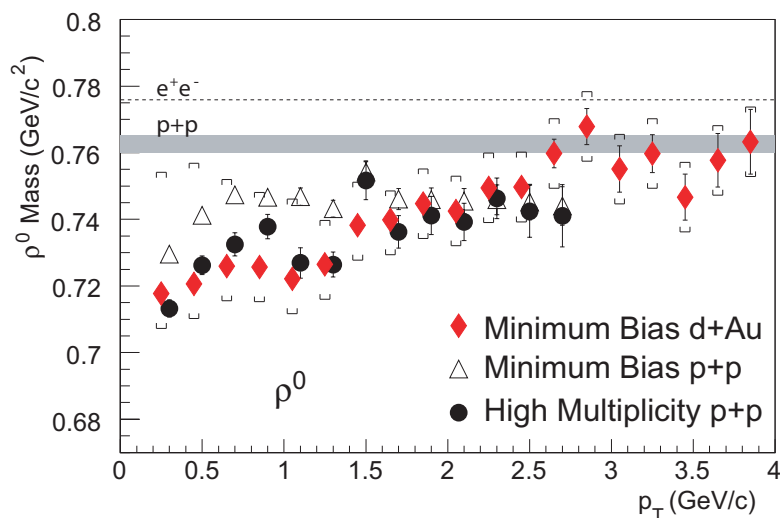


Figure 7.4: ρ^0 meson mass and width as a function of transverse momentum as measured by the STAR experiment in d-Au and p+p collisions. One observes a clear modification in d-Au collisions as compared to the vacuum value and the values measured in p+p. Figure adapted from [A+08a].

When going down in energy (and thus taking a step from the RHIC experiments to the SPS experiments) the modification of meson mass spectra are still an active field of research.

Especially the recent data from the NA60 collaboration [A+06b] presented in Fig. 7.5 stresses that vector mesons are sensitive to the density and/or temperature profile of heavy ion collisions. Since the paper by Brown and Rho in 1992 [BR91] it was expected that vector mesons shift their mass when brought into a hadronic medium. Special focus was on the ρ meson, since it is a very broad state and thus might be more sensitive to the environment.

However, more recent calculations have shown that a broadening of the spectral function (which can be linked to the mass spectrum) might occur as well. The measurement clearly favors a calculation with a broadened spectral function indicated by the dashed line. It even lead to the statement that the so called “Brown-Rho” scaling is ruled out, which lead to controversy in the past [BR05a, BR05b].

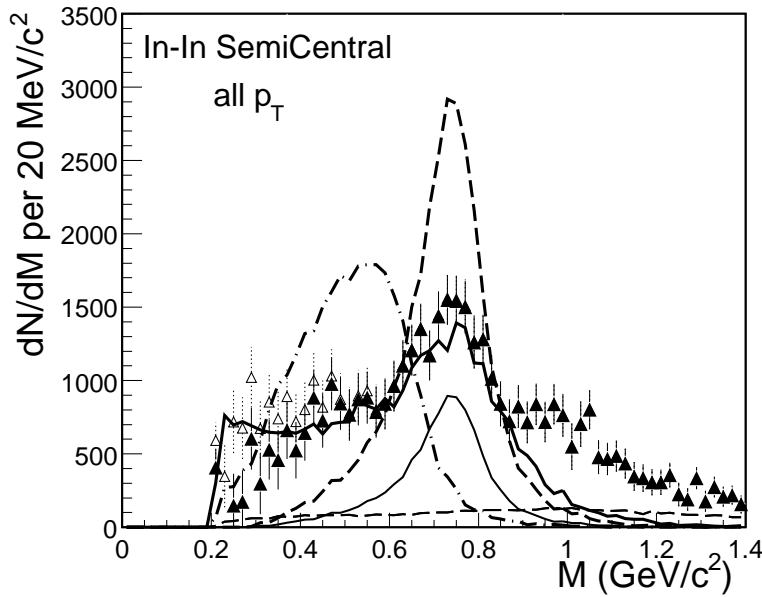


Figure 7.5: NA60 result on the ρ meson spectral function measured in semi-central In-In collisions at 158 AGeV beam energy. One observes a clearly modified resonance curve. The dashed line shows a calculation with a broadened spectral function, whereas the dashed-dotted line depicts a shifted mass spectrum. Figure taken from [A+06b].

Another way to identify mass shifts or respectively broadening of those spectra is by measuring the total dilepton mass spectrum and comparing that to calculations. This has been done for example by the DLS and HADES collaboration at relatively low beam energies of 1-2 AGeV and will be discussed in chapters 9 and 10. Just like in the case of the NA60 experiment the dilepton spectrum is measured, however there is no exact distinction made between the various contributing sources. Mass-ranges for certain decays are known, however exact yields and widths are then

extracted by comparison to theoretical investigations.

Fig. 7.6 shows such a mass spectrum for C+C collisions at 2 AGeV beam energy (top figure) and the deviations from several calculations (bottom figure). Again a deviation from the baseline calculations is visible, which might be identified with a possible signature of a mass shift of the resonances in the mass region where the deviation occurs. This special measurement will be discussed in more detail in chapter 9.

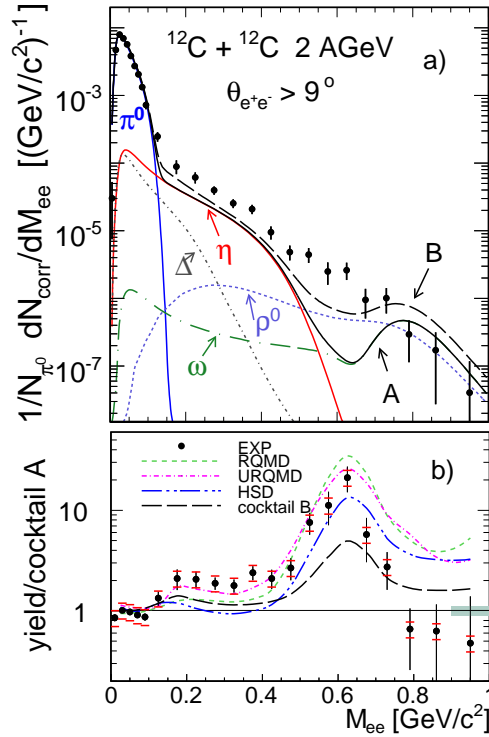


Figure 7.6: Dilepton spectrum for 2 AGeV C+C collisions measured by HADES (top). The bottom figure depicts the difference to several calculations and thermal cocktails. Figure adapted from [A+07].

The modification of mass spectra is also of interest in photon-induced reactions.

Fig. 7.7 reports one of the results of the CLAS collaboration [W+08]. Depicted is the mass spectrum for several vector mesons, as measured with a Fe-Ti target in photon induced reaction. The advantage in those collisions is, that one does not have to deal with rather complicated evolutions and non-equilibrium dynamics, but instead investigates cold nuclear matter. The effect is expected to be less pronounced than in nucleus-nucleus reactions, however the CLAS collaboration concludes that their data is consistent with no mass shift and a broadening which is compatible with collisional broadening alone. This is in direct contradiction to previous measurements in similar systems by the KEK group [N+06] and thus lead to another debate, which is not resolved yet.

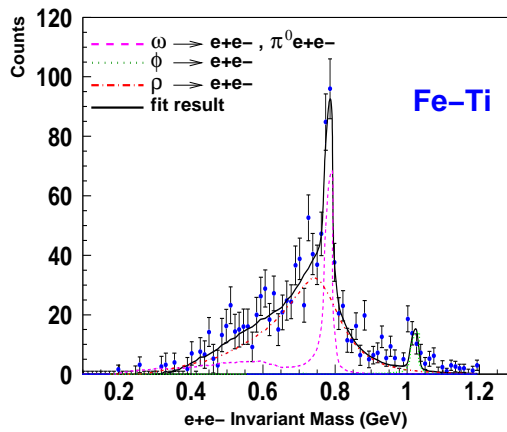


Figure 7.7: e^+e^- spectrum for photon induced reactions as measured by CLAS. Also shown are fits to the data from a hadronic cocktail. Figure taken from [W+08].

However, it is impossible to point out all (recent) measurements in detail and is certainly beyond the scope of this work. Thus we refer to the original publications for more information and continue with presenting the analyses which have been performed during the work on this thesis.

— *In physics, you don't have to go around making trouble for yourself - nature does it for you.*

Frank Wilczek

8

The a_1 meson as a signature for chiral symmetry restoration

8.1 The a_1 as an observable for chiral symmetry restoration

As already mentioned in the introduction of this thesis it is one of the main goals of relativistic heavy ion physics to reach densities and temperatures high enough to restore chiral symmetry [BGS99]. Chiral symmetry is a symmetry of quantum chromodynamics, which is exact if quark masses are zero and approximate if quark masses are small. It is spontaneously broken in nature, but expected to be restored at sufficiently high densities and temperatures. The restoration of chiral symmetry implies a change in the

spectral functions of vector mesons (e.g. the ρ meson) and leads to a degeneracy of the spectral functions of the ρ and its chiral partner, the a_1 meson. This means that the masses of the chiral partners become equal in the case of full chiral symmetry restoration or approach each other in the case of a partial restoration of the symmetry.

Especially the recently observed broadening of the ρ meson spectral function by the NA60 collaboration and the corresponding dilepton mass spectrum has been interpreted as a signal of chiral symmetry restoration [KB93, BR95, CBRW98, RW00, CB99]. In fact, the NA60 collaboration measured the ρ meson spectral function in In+In systems at the highest SPS energy of 158 AGeV and observed a deviation from the vacuum Breit-Wigner distribution [A+06b]. This has triggered various theoretical investigations [RRM06, RR07, vHR06]. In summary these studies suggest that some in-medium effects have to be considered, but a conclusive interpretation of the data is still under discussion.

Also the HADES collaboration has recently presented first results on di-electron spectra in light systems at low beam energies (C+C at 2 AGeV) [A+07], for a detailed analysis refer to the next chapter. Here a deviation from the hadronic vacuum cocktail is visible in the mass region of 500 to 700 MeV. This has been discussed as a possible observation of partial chiral symmetry restoration and the resulting change in the ρ meson spectral function. Similar data has also been measured by the CERES experiment at CERN in massive nuclear reactions at high energy [M06]. In spite of the ongoing experimental and theoretical efforts, there are numerous effects that have to be taken into account for a full understanding of data. Thus, it is questionable that a mass shift of the ρ meson alone can be regarded as a “smoking gun” signal of chiral symmetry restoration [VB06a, SVB06]. Therefore a more robust signature of chiral symmetry restoration is needed.

Theory predicts that in the case of a full restoration of chiral symmetry the spectral functions of the ρ meson and its chiral partner the a_1 meson become degenerate. The important point is that this statement is indepen-

dent of any mass shift or broadening. Thus, it has been proposed over the recent years to measure the a_1 mass spectrum in a hot and dense medium and compare it to the mass spectrum of the ρ meson [R03]. If the degeneracy would be observed it is expected to serve as an unambiguous experimental signal for the detection of chiral symmetry restoration in the hot and dense medium.

Here we argue that the measurement of the a_1 (1260) meson may not result in straightforward insights for the understanding and the detection of the chirally restored phase. We discuss the decay kinematics of the a_1 meson and argue that an apparent mass shift, or respectively a broadening of the mass spectrum may originate from mass dependent branching ratios. This effect is not unique to heavy ion reactions, but is qualitatively independent of energy and system size. Furthermore, we predict a_1 mass spectra for Au+Au and p+p collisions at 20 and 30 AGeV beam energy. The p+p calculations can serve as a vacuum reference. These systems and energies are experimentally accessible at FAIR, NA61 and the critRHIC program in the near future.

8.2 Experimental reconstruction

Experimentally, the reconstruction of resonances is challenging. One often applied technique is to reconstruct the invariant mass spectrum for single events. Then, an invariant mass distribution of mixed events is generated (here, the particle pairs are uncorrelated by definition). The mixed event distribution is subtracted from the invariant mass spectrum of the single (correlated) events. As a result one obtains the mass distributions and yields (after all experimental corrections) of the resonances by fitting the resulting distribution with a suitable function (usually a Breit-Wigner function peaked around the pole mass of the respective resonance) [A+05a, W07]. If a daughter particle (re-)scatters before reaching the detector the signal for the experimental reconstruction is lost. Especially for strongly interacting

decay products this effect can be sizeable. In addition, due to the statistical nature of the reconstruction, detailed information on the particle properties and their origin are difficult to obtain. Also possible deviations from a Breit-Wigner distribution can be overseen due to a possible dependence on the background subtraction.

Thus, we apply a different technique for the extraction of resonances from the model. We follow the individual decay products of each decaying resonance (the daughter particles). If the daughter particles do not rescatter in the further evolution of the system, the resonance is counted as “reconstructable”. The advantage of this method is that it allows to trace back the origin of each individual resonance to study their spatial and temporal emission pattern. It also allows to explore the reconstruction efficiency in different decay branches.

The decay channels of the a_1 meson are not fully experimentally investigated and details of the branching ratios are unknown [Y+06]. However, a most promising decay channel for the investigation of the restoration of chiral symmetry seems to be the decay $a_1 \rightarrow \gamma\pi$, due to the fact that the photon does essentially not interact with the surrounding (hadronic) medium. A study of all other decay channels would imply to study three particle correlations or respectively correlations between resonances and stable particles, which is very tedious, if not impossible in large systems — however, see also the discussion at the end of this chapter. Thus, experimentally, the $a_1 \rightarrow \gamma\pi$ channel seems the only feasible candidate to measure the a_1 meson in heavy ion collisions, even though the pion undergoes final state interactions.

One problem is that the branching ratio into this certain decay channel is still not very well known. For the present study, we employ a partial width of $\Gamma_{a_1 \rightarrow \gamma\pi} = 640\text{keV}$, resulting in a branching ratio of $BR_{a_1 \rightarrow \gamma\pi} = 0.0016$, in line with [Y+06]. Further experimental studies in elementary systems would be helpful to obtain more precise quantitative results in theoretical investigations.

In Fig. 8.1 the mass spectrum of the a_1 meson for p+p collisions at 20 and 30 AGeV obtained from the UrQMD calculation is shown. One observes a clear peak around the pole mass of the a_1 meson. Note that this mass spectrum is narrower than the one obtained experimentally from τ decays [S+05], and we also like to refer to [WL07] for a detailed discussion of the a_1 spectral shape.

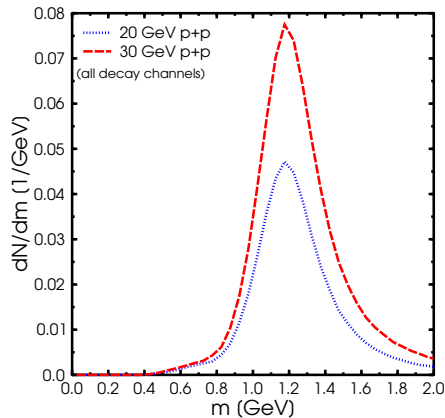


Figure 8.1: Mass distribution of a_1 mesons in proton-proton collisions at $E_{lab} = 20$ (dotted line) and 30 AGeV (dashed line) as obtained from UrQMD calculations. No trigger on a specific decay channel has been applied.

In Fig. 8.2 the mass spectrum of a_1 mesons for central ($b \leq 3.4$ fm) Au+Au collisions at 20 (full line) and 30 AGeV (dotted line) as obtained from UrQMD calculations is depicted. As in the p+p case one observes a peak around the pole mass (although slightly shifted to lower masses for kinematic reasons discussed in [BS04]).

8.3 Mass dependent branching ratios

What happens now if one explicitly triggers on the decay channel $a_1 \rightarrow \gamma\pi$ that seems most suitable for the study of the a_1 in heavy ion reactions? As discussed in [B+98, S95] the branching ratios of resonances depends on the mass of the decay products. The total decay width $\Gamma_{tot}(M)$ of a resonance

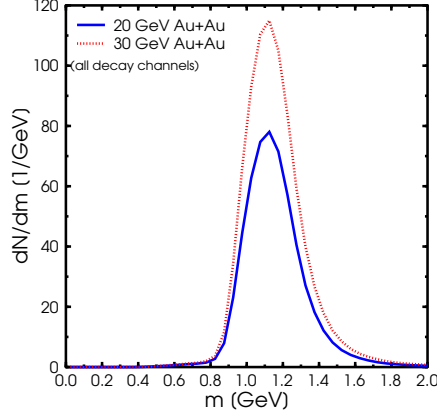


Figure 8.2: Mass distribution of a_1 mesons in central Au+Au collisions ($b \leq 3.4$ fm) at 20 (full line) and 30 AGeV (dotted line) as obtained from UrQMD calculations.

is defined as the sum of all partial decay widths and depends on the mass of the excited resonance:

$$\Gamma_{tot}(M) = \sum_{br=\{i,j\}}^{N_{br}} \Gamma_{i,j}(M), \quad (8.1)$$

where $\Gamma_{i,j}(M)$ is the partial decay width, M is the mass of the resonance and the summation over N_{br} denotes a summation over all possible decay channels. The partial decay widths $\Gamma_{i,j}(M)$ for the decay into the exit channel with particles i and j is given by [B+98, S95]:

$$\begin{aligned} & \Gamma_{i,j}(M) \quad (8.2) \\ &= \Gamma_R^{i,j} \frac{M_R}{M} \left(\frac{\langle p_{i,j}(M) \rangle}{\langle p_{i,j}(M_R) \rangle} \right)^{2l+1} \frac{1.2}{1 + 0.2 \left(\frac{\langle p_{i,j}(M) \rangle}{\langle p_{i,j}(M_R) \rangle} \right)^{2l}} \end{aligned}$$

here M_R denotes the pole mass of the resonance, $\Gamma_R^{i,j}$ its partial decay width into the channel i and j at the pole and l the decay angular momentum of the exit channel. $\langle p_{i,j}(M) \rangle$ denotes the momentum of the decay products

in the center of momentum frame. Note, however, that this equation does not include most sophisticated quantum mechanical effects but serves as a well known and often assumed phenomenological description of the underlying mass dependence of hadronic decays. To implement the full quantum mechanical description is beyond the scope of this work and has to our knowledge not been included in any other transport models.

Fig. 8.3 shows the branching ratio of the a_1 meson as a function of the mass of the a_1 as obtained from UrQMD calculations, wherein the definitions 8.1 and 8.2 are implemented including the finite width of decay particles. Filled squares depict the branching ratio of a_1 mesons into the exit channel $\rho\pi$, whereas open squares depict the branching ratio into $\gamma\pi$. Also shown is a normalized Breit-Wigner distribution (full line) and the normalized mass spectrum of the a_1 meson as obtained from proton-proton collisions at 20 AGeV from UrQMD. One observes that at masses lower than 600 MeV the decay channel of $a_1 \rightarrow \gamma\pi$ dominates because the decay channel into $\rho\pi$ is kinematically suppressed. At masses greater than 600 MeV the $\rho\pi$ decay channel is dominantly populated and the contribution from the $\gamma\pi$ channel becomes less important. Depicted in Fig. 8.3 are only two of the possible decay channels listed in [Y+06]. All other exit channels consist of even heavier decay products and are therefore negligible for this analysis.

After these semi-quantitative discussions, it is clear that a non-trivial a_1 mass spectrum has to be expected in the full UrQMD calculation, if a trigger on the $\gamma\pi$ exit channel is employed. By folding the branching ratio of $a_1 \rightarrow \gamma\pi$ and the Breit-Wigner distribution shown in Fig. 8.3 one expects a distorted mass spectrum. Let us therefore test this effect within the full transport model calculation.

Fig. 8.4 shows the mass spectrum for those a_1 mesons which can be (in principle) reconstructed in the $a_1 \rightarrow \gamma\pi$ decay channel. The thick lines depict the results for Au+Au collision at 20 or 30 AGeV respectively. The thin lines depict the mass spectrum as obtained from p+p collisions at the

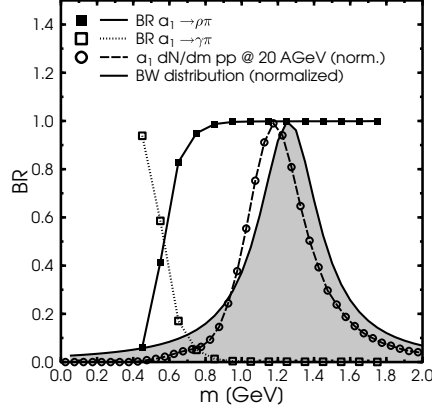


Figure 8.3: Mass dependent branching ratios for the a_1 meson with the two exit channel of $\gamma\pi$ and $\rho\pi$ as calculated from UrQMD. Filled squares depict the branching ratio of a_1 mesons into the exit channel $\rho\pi$, whereas open squares depict the branching ratio into $\gamma\pi$. Below a mass of 600 MeV the decay channel $a_1 \rightarrow \rho\pi$ is kinematically suppressed and the channel $a_1 \rightarrow \gamma\pi$ dominates. At masses above 600 MeV the branching ratio into $\rho\pi$ increases steeply. The grey shaded area depicts a normalized Breit-Wigner distribution around the a_1 pole mass, whereas the circles depict the normalized mass spectrum of the a_1 meson as obtained from UrQMD calculations for p+p collisions at 20 AGeV.

same energies. Note that the p+p curves have been scaled up for better visibility.

One observes a clear double peak structure, with one peak centered around the pole mass and one peak in the range of 400-600 MeV. This enhancement is seen in both the Au+Au and the p+p case, indicating that it may not be a unique effect seen in heavy ion collisions. Thus, a possible a_1 mass shift due to chiral symmetry restoration might be difficult to distinguish from a scenario without mass shift but including mass dependent branching ratios.

Another caveat to the detection of the chirally restored phase is the underlying baryon density distribution of the event. Although the photon does not underlie hadronic interaction, the pion still does. Thus it is important to investigate the density profile the decayed a_1 mesons originate from. The

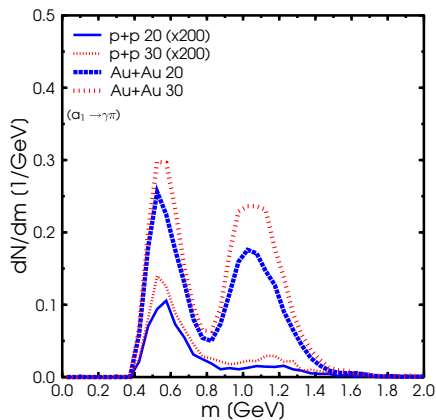


Figure 8.4: Mass distribution of a_1 mesons which can be reconstructed in $\gamma\pi$ correlations in nucleus-nucleus and proton-proton collisions at 20 and 30 AGeV. Note that the p+p curves have been multiplied by a factor of 200 for better visibility.

baryon density is averaged over all hadron positions and is calculated locally in the rest frame of the baryon current as $\rho_B = j^0$ with $j^\mu = (\rho_B, \vec{0})$. For more information regarding the density calculation refer to the Appendix. Fig. 8.5 depicts the density normalized to nuclear ground state density (ρ/ρ_0) of the point where the a_1 meson decayed into $\gamma\pi$. Full lines depict the distribution for a_1 mesons where the pion is in principle reconstructable, i.e. it does not interact in the further evolution of the system. Dashed lines depict all a_1 mesons which have decayed into $\gamma\pi$.

One observes that reconstructable a_1 mesons originate from relatively low density areas (on the average they decay at a density of 0.63 (20 AGeV)- 0.8 (30 AGeV) ρ_0 in the case where the pion can be reconstructed).

8.4 Distribution in space and time

Let us finally discuss the time and space the a_1 mesons decay. In Fig. 8.6 the a_1 meson mass spectrum is shown at different times during a Au+Au

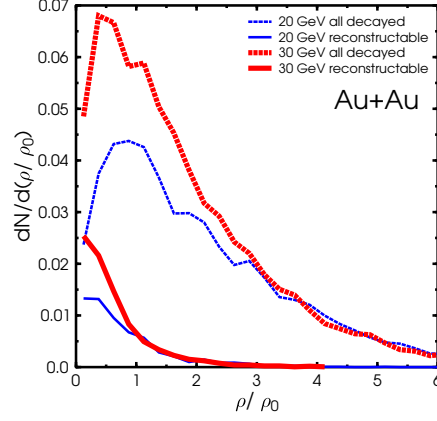


Figure 8.5: Baryon density distribution of a_1 mesons which decay into $\gamma\pi$ for central Au+Au collisions at 20 and 30 AGeV. Full lines depict those a_1 mesons where the pion does leave the medium without further interaction, dashed lines depict all a_1 mesons which have decayed (without a trigger on being reconstructable). Thick lines depict Au+Au collisions at 30 AGeV beam energy, thin lines depict Au+Au collisions at 20 AGeV beam energy.

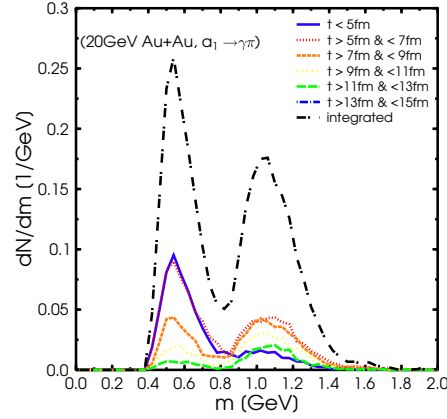


Figure 8.6: The a_1 meson mass spectrum for 20 AGeV Au+Au collisions evaluated during different times of the collision. The full line depicts decays at times before 5 fm/c, the dotted line decays between 5 and 7 fm/c. The dashed-dotted line shows the integrated mass spectrum. For the other lines the reader is referred to the legend.

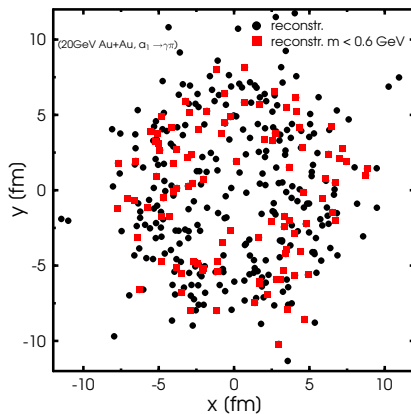


Figure 8.7: Scatterplot of the space-distribution (in x-y-plane) of $a_1 \rightarrow \gamma\pi$ decays. Circles depict a_1 mesons which can be reconstructed experimentally (i.e. the pion does not undergo final state interaction). Squares depict the reconstructable a_1 mesons which have a mass of less than 600 MeV.

collision at 20 AGeV. The full line depicts decays at times before 5 fm/c, the dotted line decays between 5 and 7 fm/c. The dashed-dotted line shows the integrated mass spectrum. For the other lines please refer to the plot's legend. One observes that the low mass part of the spectrum mainly originates from early times (below 7 fm/c). The a_1 production in this region is mainly driven by string decays, whereas at later times the production via $\rho\pi$ scattering sets in. The average center of mass energy of a string in a 20 AGeV p+p collision is 2.635 GeV. Since one has to conserve baryon number at least 938 MeV are reserved for baryon production, leaving roughly 1.6 GeV for particle production. After allocating momenta (and the probable production of pions and the corresponding momenta), this leaves roughly several hundred MeV for resonance production. This effect leads to a slight shift in the a_1 meson mass spectrum, which results in the effects which have been discussed earlier. Fig. 8.7 shows the points in space where reconstructable a_1 mesons decay. Filled circles depict reconstructable a_1 mesons without a mass-cut, whereas squares depict those a_1 mesons with a mass of below 600 MeV. One observes that there is a slight bias towards the surface of the reaction zone. This is

in line with the observation that the density at those points is rather low, which enables the pion to leave the reaction zone undisturbed.

The fact that reconstructable a_1 mesons decay at low densities coupled with the decay kinematics discussed above might make the a_1 meson a difficult messenger of chiral symmetry restoration. Measuring the a_1 from correlations of ρ mesons and pions might be more robust, however is experimentally even more demanding. One still faces the problem of the low density decays, but the $\rho\pi$ channel will avoid the problem of mass dependent branching ratios. But since the ρ meson decays mostly into pions it is required to study 3-particle correlations when analysing the hadronic decay products. However, one might also consider the electromagnetic decay products of the ρ meson.

Indeed, the HADES (and later the CBM) experiment offer the unique possibility to measure correlations between ρ mesons and pions, where the ρ meson is reconstructed via the decay channel $\rho^0 \rightarrow e^+e^-$. These measurements might indeed provide a novel and up to now unexplored route to obtain insights into the transition from the chirally broken to the chirally restored phase.

— *The electric light invades the dunnest deep of Hades. Cries
Pluto, 'twixt his snores: "O tempora! O mores!"*

Ambrose Bierce

9

Dilepton production at SiS energies - mass spectra

In the last decades large experimental and theoretical efforts have been directed to the investigation of dilepton production in heavy ion collisions [XKL90, WBC+90, WCMS90, WCM93, M94, LK95, CEK95, SK96, A+95, LKB95, RCW96, KLBS96, LKBS96, RCW97, FP97, CBRW98, P+97, BCRW98, EBB+98, SFF+03, A+06b, A+08b, A+07, A+08c, CFSF06, SVB06, THWA07, RGR+08, BC08, VPS+08, SCF+08]. Dileptons represent a particularly clean and penetrating probe of the hot and dense nuclear matter due to the fact that, once produced, they essentially do not interact with the surrounding hadronic matter. The analysis of the electromagnetic response of the dense and hot medium is tightly connected to the investigation of the in-medium modification of the vector meson properties. Vector

mesons can directly decay into a lepton-antilepton pair. One therefore aims to infer information on the modifications induced by the medium on specific properties of the vector meson, such as its mass and/or its width, from the invariant mass dilepton spectra.

A first generation of ultra-relativistic heavy ion collision experiments performed in the nineties observed an enhancement of dilepton production in heavy systems at low invariant mass as compared to conventional hadronic cocktails and models [A+95, M94]. The enhancement could be later explained by the inclusion of an in-medium modified ρ meson. At that time two possible scenarios, a dropping of the ρ meson mass according to the Brown-Rho scaling hypothesis [BR91] and the Hatsuda and Lee sum rule prediction [HL92a], or a “melting” of its spectral function as expected within many-body hadronic models [RCW97, FP97, PPL+98, LWF02], have been offered in attempt to explain these data [LKB95, KLBS96, LKBS96, RCW96, CBRW98]. If on the one side these experiments clearly showed the need for an inclusion of in-medium effects, on the other side it could not be decided, on the basis of the experimental data, whether the additional strength at lower invariant masses was due to a dropping of the vector meson mass or to the broadening of its spectral function. A first answer in this direction came from the measurements performed by the NA60 Collaboration [A+06b]. The data strongly favour the broadening over the dropping mass scenario. A similar conclusion is suggested by recent higher resolution CERES data [A+08b].

At lower bombarding energies dileptons have been measured by the DLS Collaboration at BEVALAC [P+97]. The most striking result of the DLS experiment was an observed enhancement at lower invariant masses in nucleus-nucleus collisions at 1 AGeV with respect to the corresponding theoretical spectra resulting from transport calculations [BCRW98, EBB+98, SFF+03]. Differently to the ultra-relativistic case, none of the in-medium scenarios which had successfully explained the ultra-relativistic heavy ion collision data could account for the observed enhancement [BCRW98, EBB+98] (this is known as the DLS puzzle). In the meanwhile the HADES spectrometer has been built at GSI with the aim of performing a systematic study of dilepton

production in elementary, as well as heavy ion reactions. First HADES data have recently been presented [A+07, A+08c], accompanied by a growing related theoretical activity [CFSF06, SVB06, THWA07, BC08, SCF+08].

The systems analysed here have been chosen according to the HADES program. For those systems for which the HADES data and detector filter function are available a direct comparison to the data is performed. The additional calculations are given as predictions which can be compared to experimental data in the near future.

9.1 Isospin asymmetry in η production

Before commenting on dilepton production, let us comment on meson production first. In the analysis of dilepton spectra in nucleus-nucleus collisions performed with the UrQMD model in [EBB+98], the dilepton yield originating from the η Dalitz decay was found about a factor two lower than in [BCRW98] and [H+97]. In the latter, the η channel had been determined from the measurements of the TAPS Collaboration. As already anticipated in [EBB+98], the discrepancy could be attributable to the fact that the asymmetry in the η production in pp and pn reactions (η production cross sections in pn reactions are about a factor five higher than in pp reaction) had been neglected in the calculations. Such asymmetry has been introduced for the present analysis (see Fig. 9.1).

The inclusion has been performed, as in [TCE+97], at the level of the production cross section of the $N^*(1535)$ resonance. For the C+C reactions under study the η multiplicity obtained within the UrQMD model is now consistent with the value measured by the TAPS Collaboration [A+97], as shown in Fig. 9.2.

The experimental constraint imposed by the TAPS measurements on the η Dalitz contribution to the dilepton spectra in nucleus-nucleus collisions is thus respected by our calculations. Especially for C+C collisions at 2 AGeV,

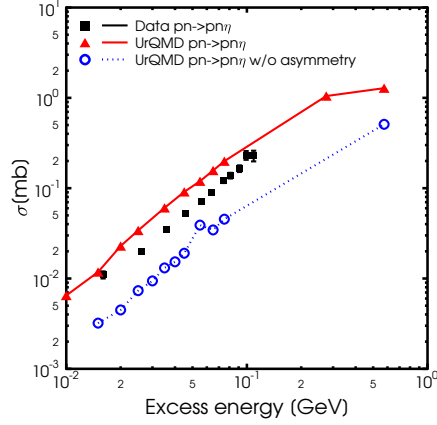


Figure 9.1: The η production cross section from pn reactions as a function of the excess energy. The UrQMD results obtained with the novel introduction of the isospin asymmetry in the η production cross section (triangles) are compared to experimental data [C+98]. The circles refer to calculations which neglect such asymmetry and are shown for completeness.

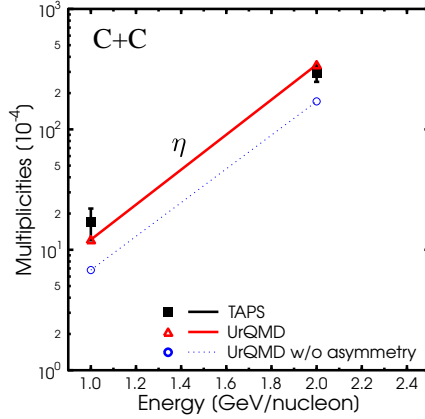


Figure 9.2: Average η multiplicity in C+C reactions at 1 AGeV and 2 AGeV from UrQMD (triangle) in comparison to the values reported by the TAPS Collaboration [A+97]. The circles refer to the standard calculations which neglect the isospin asymmetry in the η production cross section and are shown for completeness.

this is very important since, as we will see, the η decay plays an important role in determining the spectra in the low mass region.

The energy dependence of the exclusive $pn \rightarrow pn\eta$ cross section as shown in Fig. 9.1 provides a reasonable description of the data, however a finer parametrization, as e.g. in [BC08], might be required in future studies of dilepton production in elementary pn reactions. Especially for those cases where fixing the η contribution with high precision is mandatory in order to achieve an unique interpretation of the experimental data in the low mass region a re-tuning is necessary. However, pn reactions are not the major subject of this work, and the new prescription used here for the treatment of η production provides sufficient robustness for the dilepton studies presented in the next sections.

9.2 ρ production

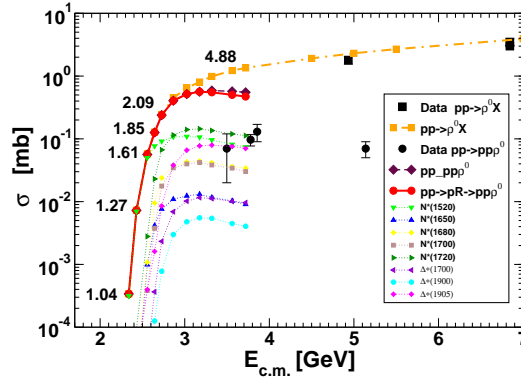


Figure 9.3: Cross sections for ρ^0 meson production in pp collisions. Calculations are shown for inclusive ($pp \rightarrow \rho^0 X$) and exclusive ($pp \rightarrow pp\rho^0$) in comparison to experimental data [FM MR84]. The contribution of the most important resonances to the resonant exclusive production is additionally shown.

Figure 9.3 shows the cross sections for the inclusive ($pp \rightarrow \rho^0 X$) and exclusive ($pp \rightarrow pp\rho^0$) production of the neutral ρ meson in pp collisions, in comparison with experimental data from [FM MR84]. The points corre-

sponding to the energies scanned by the DLS pp program are labelled by the corresponding laboratory energies to simplify the readability of the figure in view of later discussions. The resonant contribution to the exclusive production, important at the energies relevant for this analysis, is separately shown. Moreover, the contribution of the most important resonances is explicitly shown. To specify the order of the relative scale, the contribution of some of the less important resonance is shown too. The full list of resonances which couple to the ρ meson in the UrQMD model is given in Table 6.3 together with the values of the respective branching ratios in the $N\rho$ decay channel as used in UrQMD v2.3. Some of the values for the branching ratios differ from the ones used in UrQMD v1.0 [B+98, EBB+98]. However, the same values are used since UrQMD v1.1. Above the threshold for meson production by string fragmentation and decay, the $pp \rightarrow pp\rho^0$ reaction channel is additionally populated by processes involving strings.

Unless explicitly specified, in the following we will discuss in terms of laboratory energies. One observes that in collisions at laboratory energies of 1.04 - 2.09 GeV the ρ meson production is determined by the excitation of Δ^* and N^* resonances in reactions $pp \rightarrow pN^*$ and $pp \rightarrow p\Delta^*$ and the inclusive production of the ρ meson coincides with the exclusive production. In particular, the latter is practically saturated by the contribution of the $N^*(1520)$ resonance up to beam energies of 1.61 GeV. On the contrary, at 4.88 GeV, the inclusive production dominates by far the exclusive production. The first datapoints on inclusive production are well reproduced by the model, but are far away from the energies spanned by the DLS and the HADES experiments. The exclusive production, on the contrary, is systematically overestimated.

Poor and often contradictory experimental information is available on the production cross sections of N^* and Δ^* resonances. For example, in the case of the $N^*(1520)$ resonance a reduction of the cross section currently used in UrQMD by a factor 3 is possible in comparison to the experimental data [FMMR84] and results even in a smaller value of the weighted least mean square for that specific channel. We will discuss this possible source of indetermination more in detail in Section 9.6.

9.3 Elementary reactions

9.3.1 Comparison to DLS measurements

Before addressing heavy ion collisions we consider dilepton production in elementary reactions. The latter are very important to gain a better understanding of the various processes contributing to the dilepton production and of their relative weights. Note however that the model does not describe dilepton production quantummechanically correct. It does not account for quantummechanical interferences between the various subprocesses producing dileptons. However a comparison within the same model between elementary reactions and heavy ion reactions is still a valuable analysis to be done and thus will be presented in the following section. In the energy range of interest for this work there exist measurements from the DLS [W+98] and HADES Collaboration.

Differential dilepton cross sections have been calculated with the present model for pp reactions at beam energies of 1.04, 1.27, 1.61, 1.85 , 2.09 and 4.88 GeV. The results are presented in Fig. 9.4 in comparison to the DLS data [W+98]. In order to perform the comparison, the DLS acceptance filter and mass resolution have been included. For collisions at 1.04–2.09 GeV the agreement with the available data is generally reasonable in the region $M \leq 0.45$ GeV, where the π^0 , Δ and η Dalitz decays dominate, a systematic overestimation of the data is observed at higher masses. Especially at 2.09 GeV a clear overestimation of the dilepton cross section around the vector meson peak is present, a result which is analogous to the findings of [BC08]. This might be due to an insufficient modelling of the production rate of high mass resonances in $pp \rightarrow pN^*$, $pp \rightarrow p\Delta^*$ collisions. At bombarding energy of 4.88 GeV an inversion of this trend is observed and data are underestimated by the model calculations in the low invariant mass region but well described in the vector meson region. This is not a contradiction. The main difference lies in the fact that at 4.88 GeV the exclusive production of the ρ meson does

not significantly affect the inclusive production. The latter, on the other side, determines the ρ meson yields in the reactions at 1.04–2.9 GeV.

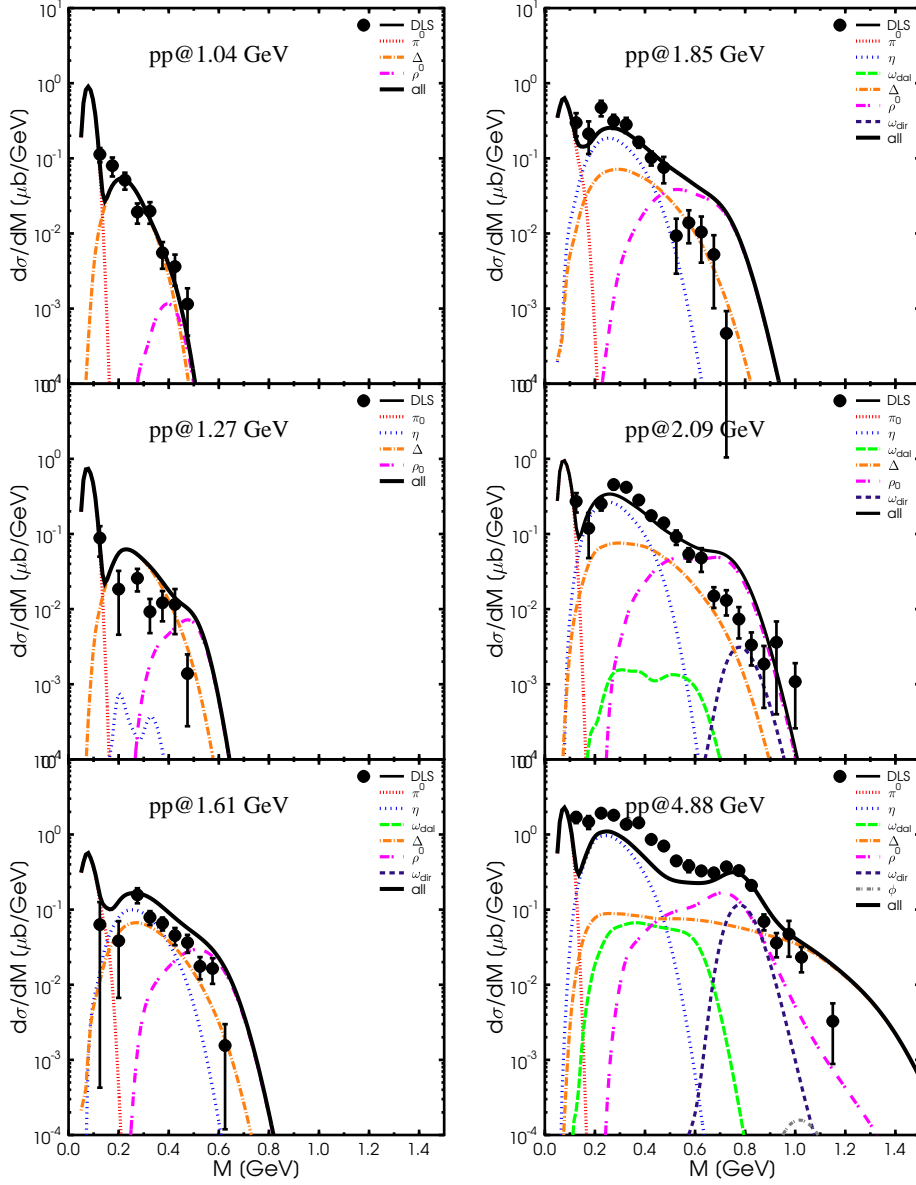


Figure 9.4: UrQMD model calculations for dilepton spectra from pp reactions at 1.04, 1.27, 1.61, 1.85, 2.09 and 4.88 GeV in comparison to the DLS data [W+98], including the DLS acceptance filter and mass resolution. The different color lines display individual channels in the transport calculation, as indicated in the legend.

9.3.2 Predictions for HADES

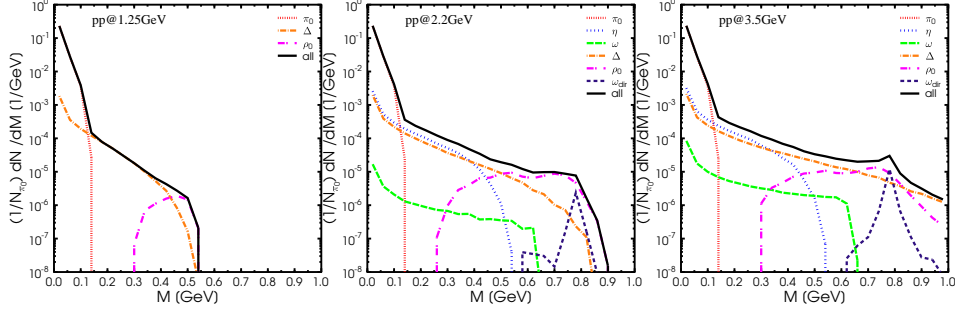


Figure 9.5: UrQMD model calculations for dilepton spectra from p+p collisions at beam energies of 1.25 GeV (left panel), 2.2 GeV (middle panel) and 3.5 GeV (right part). The different color lines display individual channels from the transport calculation, as indicated in the legend.

The HADES physic program includes measurement of pp reactions at 1.25 GeV, 2.2 GeV and 3.5 GeV which we want to discuss here. In Fig. 9.5, UrQMD calculations for the three energies are presented. The beam energy $E = 1.25$ GeV is below the $pp \rightarrow pp\eta$ threshold and is therefore optimal for studying the contribution from Δ Dalitz. For $M > 0.45$ GeV a noticeable contribution from $\rho^0 \rightarrow e^+e^-$ is visible. This result differs from other calculations [BC08], where the contribution from the direct decay of the ρ meson is not seen at the lowest energy. This is due to the omission of an explicit treatment of ρ meson production via resonant mechanism in [BC08], where a simplified parametrization of the $pp \rightarrow \rho X$ (vacuum) cross section of the form $\sigma(pp \rightarrow \rho X) \sim \int 2.2 \left(\frac{s}{s_0(M)} - 1\right)^{1.47} \left(\frac{s}{s_0(M)}\right)^{-1.1} A(M) dM$ has been employed. Here $A(M)$ denotes the meson spectral function and the integration is performed within the appropriate kinematical limits. Close to the physical threshold for ρ meson production, $\sqrt{s_{\text{th}}} = 2m_N + 2m_\pi$, such omission results in smaller values of the cross section than those of this work and of other resonance model based approaches (see e.g. [TCE+97, FKM03, SFF+03]). In our model, this contribution arises naturally due to the possibility for baryonic resonances to decay into ρ . At rather low energies, this leads to the emission of a ρ meson with a mass distribution strongly

biased by energy constraints. Here, the ρ mesons originates in particular from the decay of the $N^*(1520)$ resonance. For this chain the threshold is only $M = 2m_\pi$ and not m_ρ^{pole} . Early investigations on the role of the $N^*(1520)$ resonance for subthreshold ρ meson production were performed in [BCEM99, BK99, VB06a].

For higher beam energies all decays are possible as for the nucleus nucleus system. Both for 2.2 GeV and 3.5 GeV the dilepton spectra in the lower mass regime are dominated by the long-lived resonances and the Δ resonance. For higher masses the direct decay of the ρ meson becomes more important and the double peak shape of the e^+e^- -pairs originating from ρ is visible. At a beam energy of 3.5 GeV the contribution from the direct ω decay leads to a visible peak in the dilepton spectrum at $M \approx 0.8$ GeV.

9.4 Dilepton yields in C+C collisions

In this Section we present calculations for dilepton spectra in minimum bias C+C reactions at 1.0 AGeV and 2.0 AGeV and compare them to the data resulting from the measurements performed by the HADES Collaboration [A+07, A+08c]. In order to make the comparison with the experimental data, the filter function provided by the HADES Collaboration has been implemented [A+07, A+08c]. In agreement with the treatment of the experimental data, dilepton events with opening angle $\Theta_{e^+e^-} \leq 9^\circ$ have been rejected and the spectra have been normalised to the mean π^0 multiplicity.

We first discuss the results obtained applying the “shining” method for the extraction of the dilepton yield and address Fig. 9.6, where the contributions to the spectra of the different channels are additionally explicitly shown. Both spectra are dominated by the π^0 decay for invariant masses $M \leq m_\pi$.

In the case of C+C at 2 AGeV the η and Δ Dalitz decays dominate for $m_\pi \leq M \leq 0.5$ GeV with comparable magnitude. The present result for the

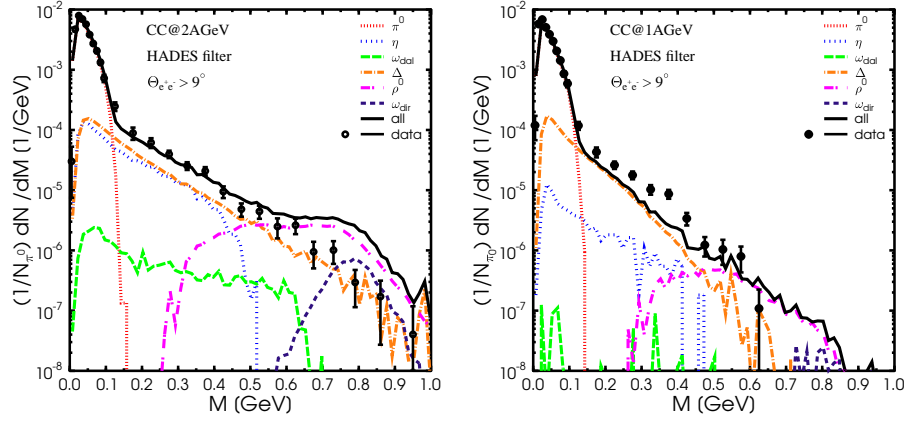


Figure 9.6: UrQMD model calculations for dilepton spectra from C+C collisions at beam energies of 2 AGeV (left) and 1 AGeV (right) in comparison to HADES data [A+07]. The different color lines display individual channels in the transport calculation, as indicated in the legend.

Δ Dalitz contribution to the spectra is quantitatively similar to the result of [BC08], whereas in [THWA07] and [SCF+08] a smaller contribution was found. For an explanation on the different treatments of the Δ Dalitz decay we refer to the original publications. The direct decay of the ρ meson starts to play a sizable role for $M \geq 0.5$ GeV. Due to the rapid decrease of the Δ Dalitz contribution, the relative importance of the ρ meson direct decay channel grows with increasing invariant mass, from being at first comparable to the Δ Dalitz to becoming the dominant contribution in the region of the vector meson peak. The low invariant mass region of the spectrum ($M < 0.5$ GeV) is successfully described by the UrQMD calculations. However, an overestimation of the data is observed at higher masses. A qualitatively analogous result has been found in the analysis of [BC08], where the “vacuum” calculation for C+C at 2 AGeV resulted in an overestimation of the data in the region of the vector meson peak. However, the enhancement being more localised around the peak than in our case and about a factor 1.5 lower at $M \sim m_{peak}$. The difference lies in the contribution originating from the direct ρ meson decay, suggesting a probably different value of ρ meson multiplicity.

The spectrum obtained assuming that dileptons are emitted at the decay vertex of the parent resonance is shown in Fig. 9.7 and compared to the result of Fig. 9.6. The two results present no sizable differences, indicating that the methods to extract dileptons are essentially equivalent when looking at time integrated yields at low energies. The reason for that lies in the smallness of the yield originating from reabsorbed resonances if compared to the emission from decaying resonances [VPS+08]. The effect of absorption processes on the dilepton spectrum is analysed in the following chapter.

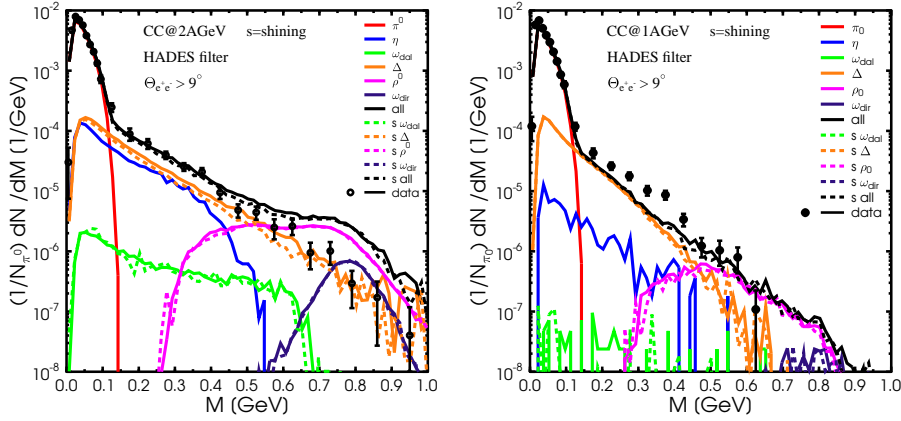


Figure 9.7: UrQMD model calculations for dilepton spectra from C+C collisions at beam energies of 2 AGeV (left) and 1 AGeV (right) in comparison to HADES data [A+07]. The full lines correspond to determination of the dilepton yield at the decay vertex of the parent particle. The dashed lines correspond to the dilepton yield resulting from the application of the shining method. The different color lines display individual channels in the transport calculation, as indicated in the legend, with s indicating the shining method.

Unfortunately no inclusive data on ρ meson production cross section are available at the energies of interest for this work. Whether the here observed overestimation of the HADES data is due to an overestimation of the ρ meson multiplicities from the nucleon-nucleon collisions or to the lack of a full treatment of the in-medium properties in the present approach, or both, cannot be decided on the basis of this experimental data. A comparison of the

mass differential dilepton cross section for pp reactions to existing DLS data has been performed and discussed in the previous section. The analysis suggested that the meson multiplicity might be indeed slightly overshoot. Due to the low resolution of the DLS data, it is for the moment not possible to make exact quantitative conclusions. In this respect, the forthcoming HADES data on dilepton production in elementary reactions will be extremely helpful to indirectly constrain vector meson multiplicities.

At 1 AGeV a systematic underestimation of the data is observed in the mass region $0.2 < M < 0.4$ GeV with a maximum discrepancy at $M \approx 0.38$ GeV. The result is qualitatively in line with previous investigations of dilepton production in 1 AGeV nucleus-nucleus collisions which link back in time to the DLS era [BCRW98, EBB+98, SFF+03]. Quantitatively, however, the discrepancy between the theoretical and experimental spectra spans here between a factor 1.5 and 2 from $M = 0.225$ GeV to $M = 0.325$ and is then at most of a factor 3 at $M = 0.375$ GeV, whereas discrepancies of a factor four had emerged from the studies performed in the nineties [BCRW98, EBB+98]. Enhanced bremsstrahlung cross sections in line with one boson exchange calculations by Kaptari and Kämpfer [KK06] have been recently proposed as possible explanation of the DLS puzzle [BC08]. The issue is however quite controversial. For pn reactions the cross sections of [KK06] differ up to a factor four from previous calculations [SBCM89, SM03]. In [KK06] and [SM03] the same couplings have been used, but differences can originate due to a different prescription used by the groups to restore gauge invariance in the effective theory. Since the way this restoration can be achieved is not unique, there are no straight arguments which favor one calculation over the other. To investigate this discrepancy, dilepton production in nucleon-nucleon collisions has been recently revisited within a fully relativistic and gauge invariant framework [SM08]. For the various contributions analyzed— pp bremsstrahlung, pn bremsstrahlung, as well as contributions with the Δ isobar intermediate state—the authors of [SM08] found cross sections smaller than those in [KK06]. In pn collisions at beam energies of 1.04 and 2.09 GeV, in particular, differences in the bremsstrahlung contribution by factors rang-

ing between 2 and 3 were found. Future HADES measurements of dilepton spectra in elementary, especially pn , collisions will help to shed light into this new puzzle.

9.5 Predictions for Ar+KCl

In this section we consider the reaction Ar+KCl at 1.75 AGeV, recently measured and currently analyzed by the HADES Collaboration. The predictions presented here refer to minimum bias calculations and have been obtained adopting the shining method. All spectra are normalised to the pion multiplicity.

The invariant mass differential dilepton spectrum is shown in Fig.9.8.

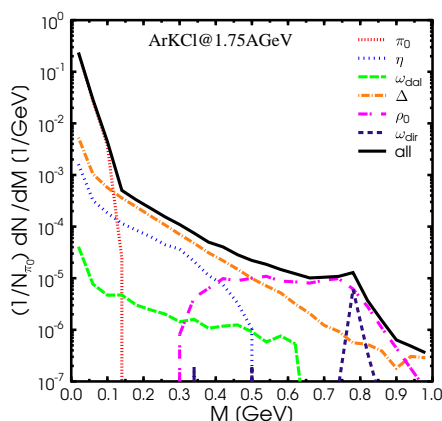


Figure 9.8: UrQMD model calculations for dilepton invariant mass spectra from Ar+KCl collisions at beam energy of 1.75 AGeV. The calculations were performed with the shining method.

Compared to C+C at 2 AGeV we observe a smaller contribution of the η resonances relatively to the e^+e^- -pairs originating from the Δ Dalitz decay. Up to a dilepton mass of 0.4 GeV the biggest contribution to this mass spectrum occurs from the long-lived mesons η and π^0 and the baryonic res-

onance Δ . Considering the contribution originating from vector mesons it is visible that the ω Dalitz decay again plays only a subordinate role, while the e^+e^- -pair production from ω direct decay becomes important for higher invariant mass, such that in the (unfiltered) dilepton spectrum a peak at $M \approx 0.8$ GeV is visible. The direct decay of the vector meson ρ dominates the mass spectrum for $M > 0.5$ GeV.

9.6 Investigating effects of baryon resonance production cross sections

In this Section we investigate the effect that an eventual overestimation of the $pp \rightarrow p\Delta^*$ and $pp \rightarrow pN^*$ cross sections would have on the ρ^0 meson and, consequently, dilepton production. The main concern is to understand whether the main features of the results presented by far will be altered and where more experimental input is needed. However, for the results presented in this work (apart from this section) the cross sections presented in Fig. 9.3 are used.

Due to the lack of high quality data and to explore the effects of this change, we divide all $pp \rightarrow p\Delta^*$ and $pp \rightarrow pN^*$ cross sections by a factor 3 with exception for the $pp \rightarrow pN^*(1535)$ cross section which is constrained by the η production. This procedure is surely too crude, but provides a rough estimate of the consequences that an eventual insufficient modelling of the hitherto used $pp \rightarrow p\Delta^*$ and $pp \rightarrow pN^*$ cross sections might have on the model calculations for dilepton spectra. The results obtained with the modified values of the $pp \rightarrow p\Delta^*$ and $pp \rightarrow pN^*$ cross sections are shown in Fig. 9.9 and Fig. 9.10. We observe that the model calculations of the exclusive ρ^0 meson production cross sections moves closer to the experimental data and the DLS data are well described in all mass range. In particular, the peak previously observed in the dilepton spectra for pp collisions at 2.09 GeV vanishes to a large extent. We notice that the readjustment of the exclusive production of the ρ^0 meson does only weakly alter the inclusive production at

laboratory energy of 4.88 GeV, neither the respective result for the dilepton spectra.

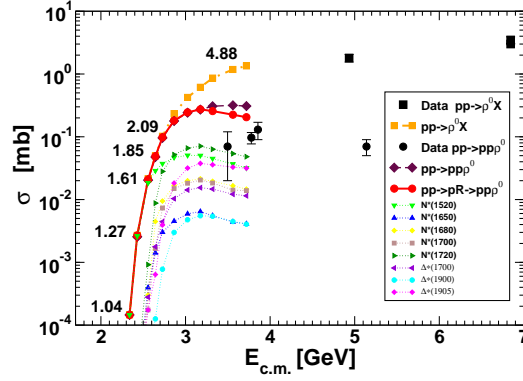


Figure 9.9: Same as Fig. 9.3, but for a smaller value of the $pp \rightarrow p\Delta^*$ and $pp \rightarrow pN^*$ cross sections, as explained in the text.

However, the main features of our results remain. In particular, the contribution to the dilepton spectrum from ρ^0 mesons at the lowest energies, although reduced, is still visible and distinguishable. Concerning the reaction C+C at 2 AGeV, we observe that the HADES data remain overestimated in the peak region even when the readjusted cross sections are used, as shown in Fig. 9.11.

Many processes, such as multiple scattering, backwards reactions, Fermi motion, etc. . . distinguish a heavy ion collision from a simple superposition of elementary reactions occurring at the same beam energy. It is also clear that in the local equilibrium limit particle production would be statistical and information on the employed elementary cross sections would be lost. In the present case, which can be seen as an intermediate regime between the two limiting cases of an elementary reaction and an equilibrated system, we find that a small readjustment of some particular cross sections can still affect the dilepton spectrum, but differences are smaller than in the elementary case.

9.6. INVESTIGATING EFFECTS OF BARYON RESONANCE
PRODUCTION CROSS SECTIONS

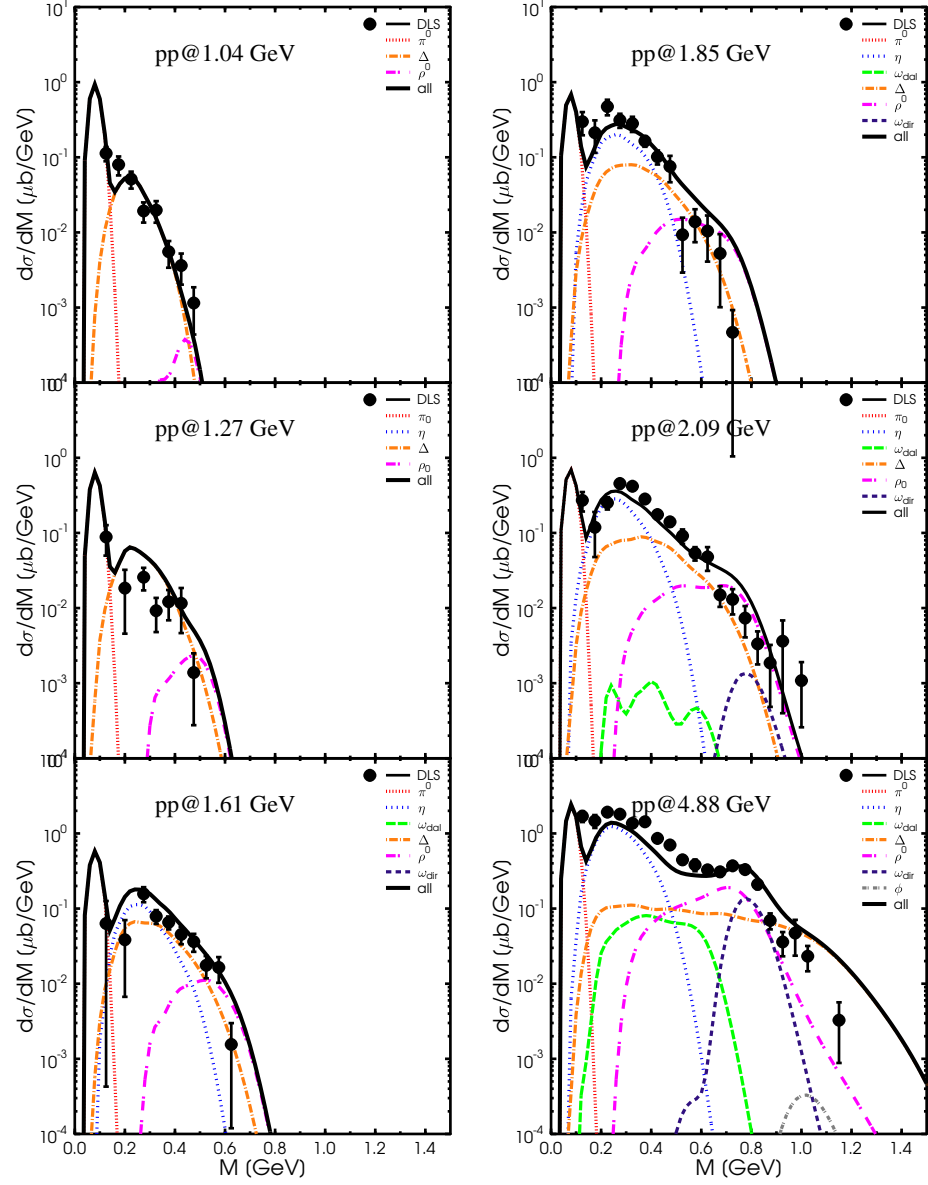


Figure 9.10: Same as Fig. 9.4, but for a smaller value of the $pp \rightarrow p\Delta^*$ and $pp \rightarrow pN^*$ cross sections.

To further investigate the dynamics and the evolution of the analyzed systems presented in this chapter we will discuss density and time evolutions in the following chapter.

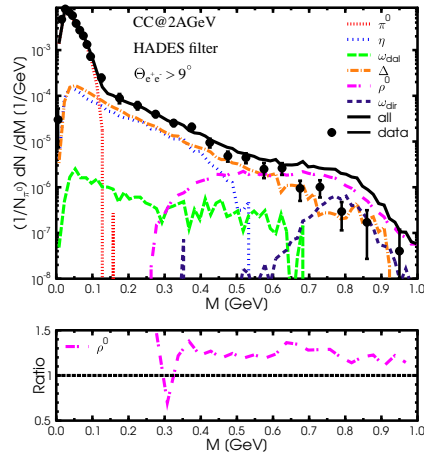


Figure 9.11: Upper panel: Same as Fig. 9.6, but for a smaller value of the $pp \rightarrow p\Delta^*$ and $pp \rightarrow pN^*$ cross sections. Lower panel: Ratio between the ρ^0 contribution to the dilepton spectra of Fig. 9.6 and Fig. 9.11.

— *If anybody says he can think about quantum physics without getting giddy, that only shows he has not understood the first thing about them.*

Niels Bohr

10

Dilepton production at SiS energies - time evolution

In this chapter we investigate the dependence of the dilepton signal on the reaction evolution time including the corresponding densities. Aim of this analysis is to trace the dilepton emission in time to identify the different stages and density regimes of the heavy ion collision from which dileptons originate. The study is performed for minimum bias C+C reactions at 2 AGeV.

10.1 Time evolution

Let us focus our discussion on the contributions of the vector mesons and the Δ resonance. The remaining contributions, π^0 and η Dalitz decays, although large, do not play a central role in the physics one aims to explore with dilepton experiments and can be viewed as some sort of standard “background”. The left panel of Fig. 10.1 shows the dilepton multiplicities as a function of the time at which the parent particle has been created. In the right panel, the multiplicities are shown as a function of the evolution time of the heavy ion reaction. In the latter, the continuous emission of dileptons from the parent particle is explicitly shown, whereas in the former the integrated value is shown. In other words, from a particle which lives from time t_i till time t_f , dileptons are emitted with the rate

$$\frac{dN^{e^+e^-}(t)}{dt} = \begin{cases} \Gamma^{e^+e^-}/\gamma & \text{for } t_i \leq t \leq t_f \\ 0 & \text{otherwise} \end{cases} \quad (10.1)$$

Here t denotes the time in the frame of the evolving system (center of mass frame of the nucleus-nucleus collision). The Lorentz factor γ connects a time interval in this system to the corresponding one in the rest frame of the emitting particle. For each particle, the function of t (10.1) is plotted in the right panel of Fig. 10.1 and corresponds to a straight line going from t_i to t_f . The corresponding integral

$$\int_{t_i}^{t_f} \frac{dN^{e^+e^-}(t)}{dt} dt = \Gamma^{e^+e^-} \tau \quad (10.2)$$

where $\tau = (t_f - t_i)/\gamma$ is the life-time of the particle, gives the total number of dilepton emitted by the particle (created at $t = t_i$) and is reported in the left panel of Fig. 10.1.

We observe that:

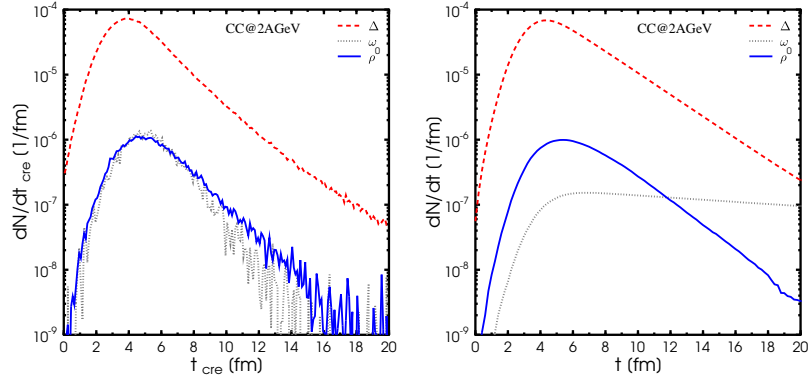


Figure 10.1: Dilepton multiplicity and rate for minimal bias C+C collisions at beam energies of 2 AGeV as a function of the time at which the parent particle made its first appearance in the evolving system (left panel) and corresponding averaged dilepton rate as a function of the evolution time of the heavy ion collision (right panel).

- Most dileptons originate from particles created within the first 8 fm. The emission is maximal from vector mesons created at about 5 fm and Δ resonances created at slightly earlier time (about 3.5 fm). This is understandable if one considers that in the resonance model vector mesons arise from the decay of baryonic resonances. Since the baryonic resonances have a typical total width of the order of 100-200 MeV, their decay takes typically place about 1-2 fm after their creation.
- In the case that the parent particle is a relatively short lived particle, e.g. a Δ resonance or a ρ meson, most dileptons are emitted within the first 10 fm, with a maximum around 6 fm. Later, for $t > 6$ fm, the dilepton emission strongly decreases with increasing time. On the contrary, if the parent particles is a long lived particle, e.g. a ω meson, dileptons are emitted continuously at an almost constant rate for $t > 6$ fm. This is due to the fact that those ω mesons which happened to survive the various absorption processes live relatively long and emit dileptons during their whole life-time.

In Fig. 10.2 the role of absorption on the reduction of the dilepton signal is shown. The observed yield is compared to the yield expected from a vacuum-like picture in which the parent resonance, after being produced, does not interact further up to its decay, here simply denoted by “full weight” scenario. For a detailed discussion of the different prescriptions for dilepton production see [VPS+08]. The total dilepton signal from vector mesons is reduced by a factor of 1.5 (for the ρ meson) - 2 (for the ω meson) due to reabsorption. Especially in the case of the ω meson the “potential” dilepton signal of those particles which are absorbed (labelled by ω_{abs} in Fig 10.2) is strongly suppressed (roughly by a factor 20).

10.2 Density evolution

Next, we investigate the influence of the baryon density locally present on the electromagnetic response of the system, as depicted in Fig. 10.3. It is clear that a particle propagating through a high density zone of the system will interact, with a certain probability, with the particles present in its surroundings. Absorptive interactions, e.g. $\rho N \rightarrow N^*(1520)$, will lead to the disappearance of the parent particle from the system within shorter times than its vacuum mean lifetime (determined by its decay width). As a consequence of its shorter lifetime, the total dilepton yield from the particle will be reduced with respect to the yield expected if the particle would be present in the system until its decay and emit dileptons for a time interval τ_{dec} . In particular, the number of dileptons expected to be emitted by a parent particle created in a space-time point characterised by a local baryon density ρ_{cre} is analysed. The result is reported in Fig. 10.2 (right).

We observe that between 13% and 20% of dileptons originate from particles created at densities $\rho_{cre} > \rho_0$ and that absorption reduces the potential dilepton yield from these particles by a factor 1.5. This effect is particularly strong in the case of the ω meson. It is evident from the previous analysis

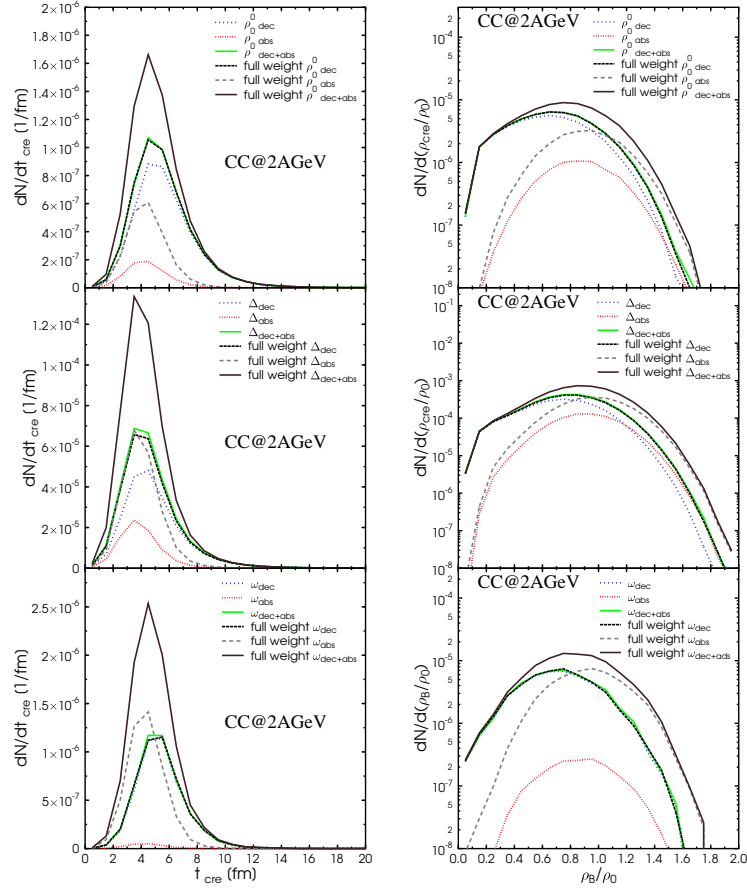


Figure 10.2: (Left) Dilepton multiplicity from minimal bias C+C collisions at beam energies of 2 AGeV as a function of the time at which the parent particle made its first appearance in the evolving system. The dashed lines denote calculations where the full branching ratio into dileptons is attached to both the decay and the absorption vertices.

(Right) Dilepton multiplicity from minimal bias C+C collisions at beam energies of 2 AGeV as a function of the local density present in the space-time point at which the parent particle has been created. The dashed lines denote calculation where the full branching ratio into dileptons is attached to both the decay and the absorption vertices.

that the parent particles seem to be characterised by relatively short lifetimes in the high density phase.

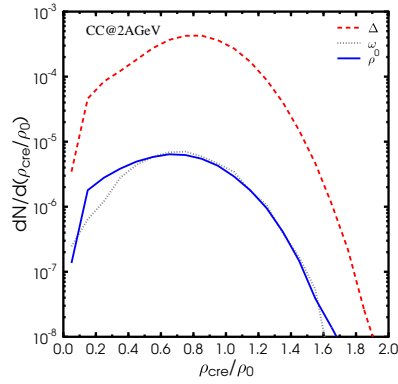


Figure 10.3: Dilepton multiplicity from minimal bias C+C collisions at beam energies of 2 AGeV as a function of the local density present in the space-time point at which the parent particle has been created.

To further evaluate the density profiles of resonances and dileptons in heavy ion collisions we will perform an energy scan in the next chapter. We will further motivate why the ρ meson is of particular interest and discuss different methods to calculate dileptons.

— *Things on a very small scale [like electrons] behave like nothing that you have any direct experience about. They do not behave like waves, they do not behave like particles, they do not behave like clouds, or billiard balls, or weights on springs, or like anything that you have ever seen.*

Richard Feynman

11

How sensitive are ρ mesons to the hot and dense stage of heavy ion collisions?

11.1 The change of ρ meson properties as an observable in heavy ion collisions

Quantum-Chromo-Dynamics (QCD) predicts that the properties of hadrons change when they are brought into a (hot and/or dense) nuclear environment [HL92a, BR91]. This modification is due to the interaction with the surrounding medium which eventually leads to chiral symmetry restoration at high baryon densities and/or high temperatures [RW00]. The experimental verification of this theoretical prediction is one of the most challenging questions in modern strongly interacting matter physics.

Among the non-strange mesons the ρ meson plays a dominant role in these investigations. It has a short lifetime and therefore it has a large probability to decay inside the reaction zone when created in heavy ion collisions. It couples strongly to nuclear resonances and, most important, it has a non-negligible chance to decay into dileptons which leave the interaction zone essentially without any further interaction. Thus, the dilepton channel seems to offer a unique chance to study the high baryon density properties of the ρ meson. However, we will discuss a novel development in the next chapter.

Theoretically the question of how the spectral function of the ρ meson changes in the medium is still under active discussion. There is certain theoretical evidence that the ρ meson is broadened if put into the nuclear medium [P95, RCW96, RCW97]. In contrast, Hatsuda and Lee predicted a lowering of the ρ meson mass in a nuclear environment based on QCD sum rules calculations [HL92a]. A result which has also been found by Brown and Rho [BR91, LKB95, BR02]. On the other hand, more recent calculations indicate that the pole mass of the ρ meson remains almost unchanged in the nuclear medium [vHR06, RR07, DTZ07]. However, these calculations rely on specific assumptions on the coupling strength of the ρ meson to the nuclear resonances and on the branching ratios whose validity can presently only be proven by comparison to experimental data. For the present status of the theoretical spectral function calculations for vector mesons we refer to [GLL+07, R07, SCF+08] and references therein.

Experiments have been launched to verify these theoretical predictions. In proton-nucleus collisions [N+06, O+01] at 12 GeV a decrease of the ρ meson mass with increasing baryon density ρ_B as $m(\rho_B)/m(0) = 1 - 0.09\rho_B/\rho_{B0}$ - about half of the value predicted by theory - but without an increase of the ρ meson's width has been reported. The CLAS collaboration reports that the experimental data of photon-induced reactions is compatible with no shift of the ρ meson pole mass and no additional broadening to the theoretically estimated collisional broadening [WDNW07]. In contrast, the dilepton data in In+In collisions at 158 AGeV [A+06b] are best described using essentially the free ρ meson pole mass but a considerable broadening of the spectral

function. At lower energies of 2 AGeV the HADES collaboration has recently published dilepton spectra [A+07]. Here, a deviation from the yield calculated from a hadronic cocktail fit in the vicinity of the ρ meson mass is visible but due to the many sources of dileptons there is no conclusive explanation for that suppression yet (see also the previous chapters of this thesis). How much of these different experimental findings can be exclusively attributed to the different environments, i.e. cold nuclear matter in proton-nucleus reactions, an expanding meson dominated fireball after a possible phase transition from a quark gluon plasma in high energy nucleus-nucleus collisions at the SPS or a baryon dominated expansion in reactions at about 2 AGeV is still a matter of debate.

11.2 Approaches to model dileptons from ρ mesons

To link the final state dilepton data to the in-medium spectral functions of the hadrons detailed quantitative theoretical simulations of the baryon density distribution at the ρ meson production and decay/absorption point are necessary. This allows then to calculate dilepton spectra from the simulations. Unfortunately, up to now different approaches are used to convert the calculated hadron spectra into dileptons. In general four different approaches can be identified:

- Explicit propagation of stable particles, baryon and meson resonances, decays of resonances into other mesons (especially baryonic resonances into ρ mesons), as well as $\pi\pi \rightarrow \rho$ scattering. Dileptons are emitted continuously from vector mesons and baryon resonances with their respective locally given total width while the resonances are propagated (“shining”) [KS96, EBB+98, CB99, CBJ00, BC08, SSV+09],
- Explicit propagation of stable particles, baryon and meson resonances, decay of resonances into other mesons (especially baryonic resonances

into ρ mesons), as well as $\pi\pi \rightarrow \rho$ scattering. Dileptons are only emitted at the point of decay (not absorption) of the hadronic resonance [SVB06],

- Explicit propagation of nucleons, pions and nucleon resonances while vector meson degrees of freedom are not propagated explicitly. Dileptons are produced via the eVMD model from nucleonic resonances at the point of the decay of the nucleonic resonances. This model assumes dilepton production via intermediate ρ/ω states [CFSF06, SCF+08],
- Explicit propagation of nucleons, pions, kaons and Δ resonances. Dileptons are produced by decay of nucleonic resonances according to the branching ratios. This is supplemented by the dilepton production from mesonic resonances, which are calculated by folding the \sqrt{s} distribution of the elementary nucleon-nucleon collisions with the mesonic production cross sections and the corresponding branching ratios into dileptons [THWA07].

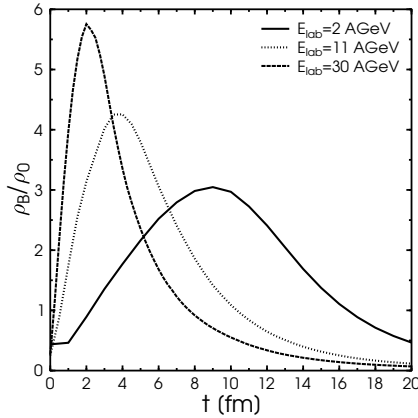


Figure 11.1: Time evolution of the local rest frame baryon density ρ_B averaged over the positions of the individual hadrons for central Au+Au/Pb+Pb reactions at various beam energies.

While the first method is sensitive to all stages of the collision and allows for a dynamical treatment of the collisional broadening, the other methods

rely on the actual decay of the meson or baryon resonance. Thus, the different approaches probe different baryon density regimes and might therefore provide different results for the extracted dilepton rates. Another problem is posed by the implementation of bremsstrahlung especially at low beam energies. This discussion has recently been revived by the calculations of [SM03, KK06, THWA07, BC08].

In this situation it is necessary to study the general differences between the above discussed approaches and explore the baryon density probed by the ρ meson in the FAIR energy regime. This helps to provide a theoretical error margin for further detailed model studies on the change of the in-medium spectral functions at these energies.

We perform this study for massive nuclear reactions in the energy range of $2A \text{ GeV} \leq E_{\text{lab}} \leq 30A \text{ GeV}$. This range marks the expected transition towards chiral symmetry restoration, but also the transition from baryon dominated to meson dominated matter. Dedicated facilities to explore this energy domain are the FAIR project at GSI [AGK+08] and the critRHIC program at BNL [S06].

For this study we again apply the UrQMD approach which has been described in detail in chapter 6. Although being a vacuum property approach, one should note however that the particle properties are dynamically modified in a hot and/or dense medium due to the coupling of the ρ meson to the surrounding hadrons (at SIS energies especially the baryon resonances are important [VB06a]). The ρ meson is assumed to have a lifetime according to an exponential distribution with a mean lifetime τ of $1/\Gamma_{\text{pole}} \simeq 1/150 \text{ MeV}$, in addition collisional broadening is implicitly taken into account for the calculation of dileptons by the interaction of the ρ meson with the evolving medium.

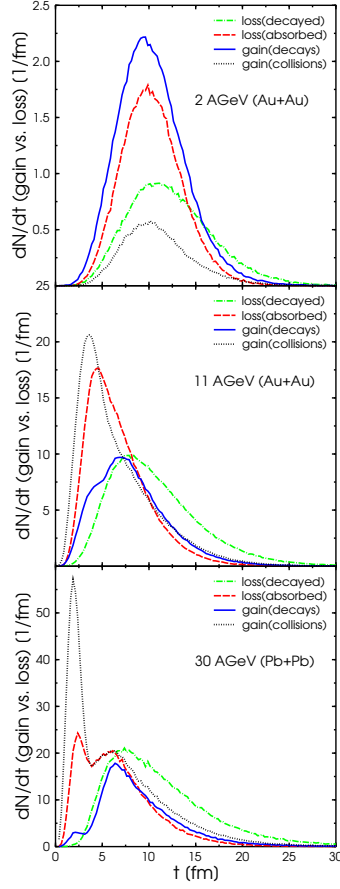


Figure 11.2: Gain and loss rates of ρ mesons separated gain from collisions (“gain(collisions)”), gain from decay (“gain(decays)”) and loss due to absorption (“loss(absorbed)”) and loss in decays (“loss(decayed)”). From top to bottom we display central Au+Au/Pb+Pb collisions at 2, 11 and 30 AGeV.

11.3 Density calculation

Let us start the discussion by displaying the time evolution of the baryon density in central Au+Au/Pb+Pb reactions at 2, 11 and 30A GeV (see Fig. 11.1). The baryon density is averaged over all hadron positions and is calculated locally in the rest frame of the baryon current (Eckart frame) averaged over the position of every baryon as $\rho_B = j^0$ with $j^\mu = (\rho_B, \vec{0})$. Details on the calculation of the baryon density are discussed in the Appendix. Note

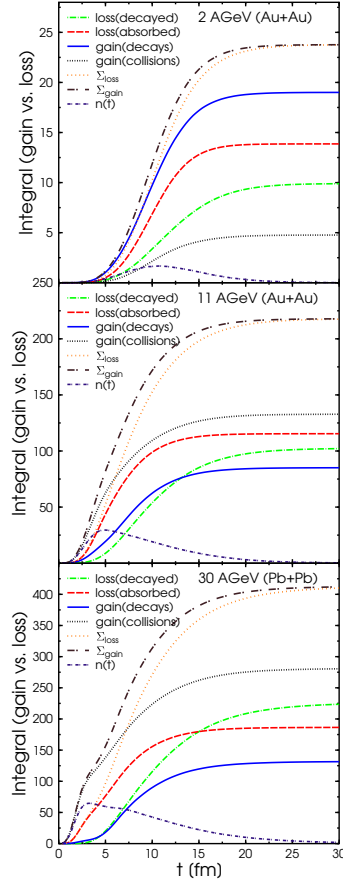


Figure 11.3: Gain and loss of ρ mesons separated for collisions and decay. From top to bottom we display central Au+Au/Pb+Pb collisions at 2, 11 and 30 AGeV. We show as well the difference of gain and loss, the number of ρ mesons present in the system as a function of time. From top to bottom we display central Au+Au/Pb+Pb collisions at 2, 11 and 30 AGeV.

that the maximal baryon density grows with increasing beam energy. The question to be asked is, how sensitive are dilepton observables on the high baryon density stage of the collisions?

11.4 Gain and loss rates of ρ mesons

In order to investigate this question, we first review the different production and loss mechanisms for the ρ meson. In UrQMD the ρ meson can be produced from the decay of a high mass (meson or baryon) resonance or directly in a collision of two particles (e.g. $\pi + \pi \rightarrow \rho$) which includes also the production from string fragmentation. The ρ meson is destroyed by two different mechanisms. It can decay (“loss (decayed)”, e.g. $\rho \rightarrow \pi^+\pi^-$) or it can be absorbed in collisions (“loss (absorbed)”, e.g. $\rho + \pi \rightarrow a_1$).

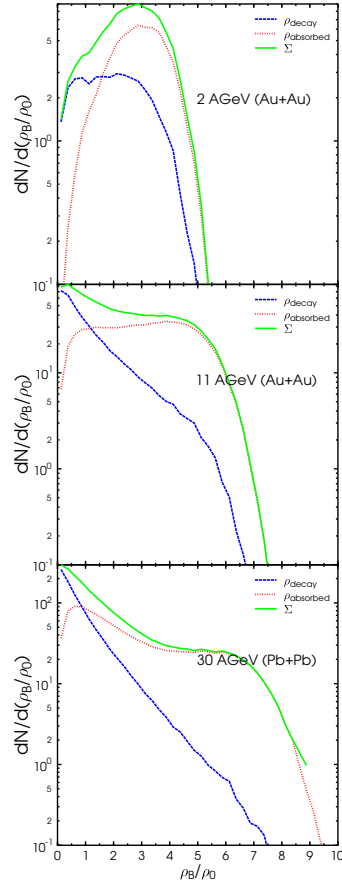


Figure 11.4: Baryon density distribution at the space points where the ρ mesons decay. From top to bottom we display central Au+Au/Pb+Pb collisions at 2, 11 and 30 AGeV.

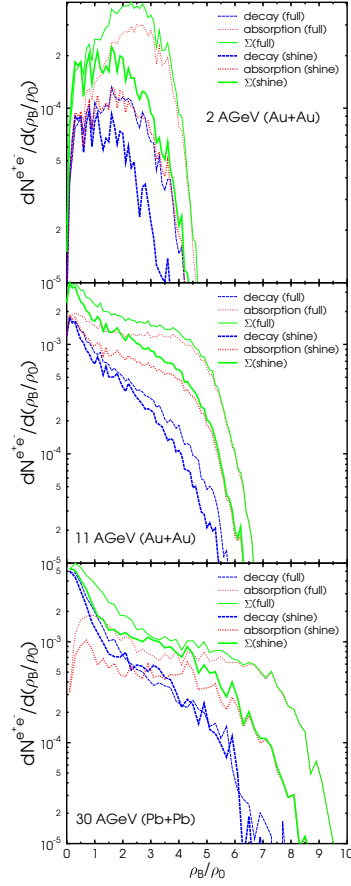


Figure 11.5: Distribution of the baryon density at which the e^+e^- -pairs from the ρ vector meson are emitted. The thin lines denote calculation where the full branching ratio into dileptons is attached to both the ρ decay and the ρ absorption vertices. The thick lines indicate the results obtained by the shining method with continuous emission of dileptons. From top to bottom we display central Au+Au/Pb+Pb collisions at 2, 11 and 30 AGeV.

In Fig. 11.2 we show the respective gain and loss rates of ρ mesons separated for the different contributions for central Au+Au and Pb+Pb reactions at $E_{\text{lab}} = 2, 11$ and $30A$ GeV. The different processes ¹ in which a ρ meson is produced are denoted as “gain (collisions)” or “gain (decays)” (meaning the stem from the decay of another resonance). The loss term differentiates also

¹All processes where the number of in-going ρ mesons equals the number of outgoing ρ mesons have been discarded from the analysis as they provide only a trivial off-set.

between ρ mesons which have decayed “loss (decayed)” and those which are absorbed in collisions “loss (absorbed)” as discussed above.

At 2A GeV, one observes that the production rate of ρ mesons is dominated by the decay of resonances ($\sim 80\%$, full line) as compared to the formation in a s-channel $\pi\pi$ scattering ($\sim 20\%$, dotted line). This observation is in line with the expectations that a dominant production channel for the ρ meson in low and intermediate energy heavy ion collisions is the decay of baryon resonances [WSSG95]. A previous detailed analysis of the ρ meson production channels at 2A GeV within the UrQMD approach, found in [VB06a] confirms this interpretation in detail. The maximum of the ρ meson production rate coincides with the maximum baryon density around $t \sim 9$ fm. However, these ρ mesons are subject to frequent interactions with the surrounding baryons resulting in rather short life times of the ρ mesons as indicated by the large absorption rate (dashed line). Only towards the end of the high density stage (when the ρ absorption processes, e.g. $\rho + B \rightarrow B^*$ cease) ρ mesons can decay directly as denoted by the dashed-dotted line. In the present model ρ meson absorption accounts for the main loss of ρ mesons, while the decay accounts for only 30% of the ρ meson loss. It is clear that these features might lead to different time-dependent dilepton yields, depending on the method with which the dilepton rates are extracted from the numerical simulation.

At higher energies (11A GeV, 30A GeV) this low energy line of arguments changes. Here one observes two distinct phases for the production and decay/absorption of the ρ meson. Initially ρ meson production from collisions proceeding either via string formation and fragmentation or via meson-meson scattering dominates the gain term (dotted line). However, also the absorption probability is rather high in this stage of the reaction resulting in a quick re-absorption of the ρ meson (dashed line). For dilepton calculations it becomes clear that only a “shining” approach has the potential to provide information on this stage, whereas the approaches which depend on the decay of the resonance do not allow to extract this information. However, also at higher energies, the production of ρ mesons from resonance decays in the

late stage of the reaction is sizeable. This is evident because the sequential processes $NN \rightarrow B^* + X$, $B^* \rightarrow \rho + X$ will need a certain time and therefore trigger on later stages of the reaction. Thus, the ρ meson production from baryon resonance decays again leads towards a self-triggering of ρ meson production and subsequent decay at rather moderate densities, even at energies of $11A$ GeV and $30A$ GeV.

To gauge our assumptions for the absolute importance of the different processes the integrated ρ meson rates are shown in Fig. 11.3. The nomenclature is the same that has been used in Fig. 11.2. The temporal evolution of the integrals for three values of beam energies from $E_{\text{lab}} = 2A$ GeV to $E_{\text{lab}} = 30A$ GeV is calculated. In addition, the sum of the gain (Σ_{gain}) and the sum of the loss terms (Σ_{loss}) are displayed. If one subtracts the sum of the loss terms from the sum of the gain terms one gets the yield ($n(t)$) of ρ mesons which is present at each time of the collision.

As discussed above, at the lowest energy the gain via resonance decays dominates over the gain from direct ρ meson production due to kinematical constraints. However, this behaviour reverses already at $E_{\text{lab}} = 11A$ GeV. At the highest energy ($E_{\text{lab}} = 30A$ GeV) displayed already a factor of 2.5 more ρ mesons are produced in collisions than in decays of other resonances. For the loss term we observe a dominance of the absolute value of decayed ρ mesons at $E_{\text{lab}} = 30A$ GeV.

Let us investigate the baryon density distribution at the space-time position of the ρ meson decay and absorption in more detail. Fig. 11.4 shows the probability distribution of the baryon density at the instant of the ρ decay (dashed line), ρ absorption (dotted line) and for the sum of both (full line).

At $2A$ GeV (top figure) one clearly observes that absorption of the ρ meson in the most dense medium reached at SIS energies ($\sim 3\rho_B/\rho_{B0}$) is already a strong effect. If only decaying ρ mesons are taken into account the effective density probed reduces to ($\sim 2\rho_B/\rho_{B0}$) At higher beam energies ($11A$ GeV, $30A$ GeV) this splitting in the density between decaying ρ mesons and absorbed ρ mesons becomes even more pronounced. Here, absorption

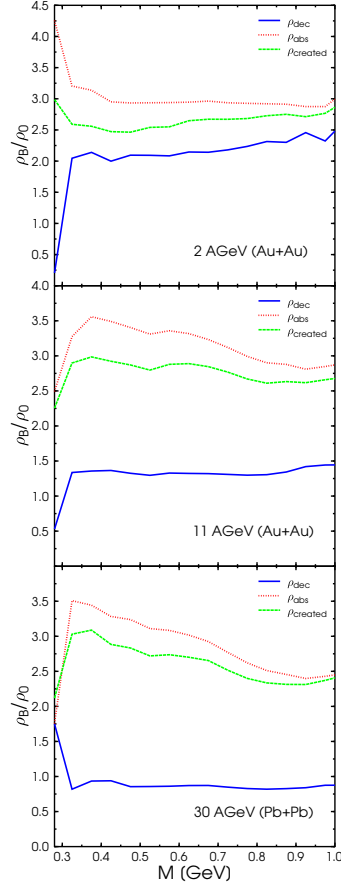


Figure 11.6: Average baryon density experienced by a ρ meson as a function of the mass of the ρ meson. The results of the present calculation for the creation, absorption and decay point of the respective ρ meson are shown. From top to bottom we display central Au+Au/Pb+Pb collisions at 2, 11 and 30 AGeV.

processes are strongly dominating the high baryon density stage, while decays populate the low baryon density region.

11.5 Dilepton rates

To relate the present discussion directly to the sensitivity of dileptons to the most dense stages of the reaction, dilepton rates are calculated as a

function of the baryon density at which the dileptons are emitted. The dilepton calculations are based on standard cross sections as discussed in chapter 4. Fig. 11.5 gives the distribution of the baryon density at which the e^+e^- -pairs from the ρ vector meson are emitted (from top to bottom central Au+Au/Pb+Pb collisions at 2, 11 and 30 AGeV are shown). For each energy, the dilepton production as a function of baryon density is separated into a part where the initial ρ meson decays (dashed lines) and a part where the ρ meson was absorbed by the medium (dotted lines), the sum of both contributions provides the total emission rate of dileptons and is shown as full lines.

Two different scenarios related to the initially discussed theoretical approaches for the dilepton extraction can be discussed:

1. In the first scenario, the full branching ratio into dileptons is attached to both the ρ decay and the ρ absorption vertices (shown as thin lines). This provides the most optimistic reach towards high baryon densities, as it assumes that no collisional broadening takes place even in the most dense stage of the reaction (i.e. it is a full vacuum baseline calculation). On the one hand, this setting is similar to the one employed in models that calculate dileptons from folding the \sqrt{s} distribution of nucleon-nucleon collisions as it assumes no interaction of the produced ρ meson with the medium, i.e. absorption. On the other hand, if one omits the dileptons emitted in the absorption process, these calculations are similar to previous calculations that assume dilepton production only from the late stage decays of (baryon) resonances.
2. This scenario is set in contrast to the shining approach (indicated by thick lines). In the shining method, a continuous emission of dileptons is assumed over the whole lifetime of the ρ meson (generally for all relevant hadrons). The dilepton emission rate is then integrated over time, taking the collisional broadening for each individual vector meson in its surrounding into account. Due to the strong collisional broadening in the medium, a drastic reduction in the analysis reach of dileptons

towards high densities (shown in Fig. 11.5 from the comparison of the thick and thin full lines) results. At SIS and FAIR energies, the effective baryon density probed by ρ mesons decaying into dileptons is reduced to 1-2 ρ_B/ρ_{B0} in contrast to the expected values of around 2-3 ρ_B/ρ_{B0} from scenario 1. At higher energies (11A GeV, 30A GeV), the reach of dileptons into the most dense stage is also strongly reduced. In addition, late stage decays of baryon resonances and ρ mesons provide a strong trigger towards low baryon densities, resulting in strong peak of the dilepton emission rate below 1-1.5 ρ_B/ρ_{B0} . This low density peak might possibly blur the view on the most interesting dileptons from the most dense stages of the reaction.

Finally, we explore the average baryon density experienced by ρ mesons with different masses. This is important to understand whether any prominent features are present in the ρ meson mass region between 400 – 600 MeV, which is of interest for the intermediate mass dilepton enhancement. Fig. 11.6 depicts the average baryon density experienced by a ρ meson as a function of the mass of the ρ meson. Fig. 11.6 gives the results of the present calculation for the creation, absorption and decay point of the respective ρ meson. One observes that the baryon density of the system is constant as a function of the mass, indicating that most ρ mesons, independent of their mass, decay at a certain (low) baryon density, as argued before. Note that the baryon density where ρ mesons are absorbed is higher, which is in line with the previous discussion.

In conclusion of this analysis, we have shown that the measured dileptons provide only a restricted view into the most dense stages of the reaction despite the fact that electromagnetic probes leave the reaction zone without any further interaction. Thus, possible studies of meson and baryon properties at highest baryon densities might be blurred.

However, after analyzing leptonic decay channels it is plausible to investigate hadronic decay channels as well. This analysis will be carried out in the next chapter.

— *Physics isn't a religion. If it were, we'd have a much easier time raising money.*

Leon Lederman

12

High p_T resonances as a possibility to explore hot and dense nuclear matter

12.1 Problems of hadronic decay channels

The experimental analysis of heavy ion reactions using resonances has been applied for several years from low energy [A+07, L+07] through intermediate [A+01, A+03] to high energy heavy ion collisions [A+06a, A+08a, F08]. In general one distinguishes between leptonic and hadronic decay channels. Although the leptonic decay channels have the advantage that the decay particles do not undergo final state interactions, the hadronic decay channels have the advantage of larger branching ratios. Thus it is worthwhile to work out the differences and the advantages and disadvantages of the two approaches which will be discussed in the following.

The leptonic channels have been thoroughly discussed in the previous chapters 9, 10 and 11. So let us turn our attention to the hadronic channels and check if we can use their large branching ratios as a tool to gather information from the high density phase of heavy ion collisions.

The present Relativistic Heavy Ion Collider (RHIC) at Brookhaven and the upcoming Facility for Antiproton and Ion Research (FAIR, for a recent status on the project we refer to [H08]) provide an excellent research environment for probing resonances in matter. At the RHIC experiments it has been observed [M08] that less resonances are measured than expected from statistical model calculations [ABMRS03]. Stable hadrons however follow the prediction of this model. This suggests the conclusion that after chemical freeze-out, when the chemical composition of the final state is determined, hadrons still undergo collisions and therefore some of the resonances cannot be identified by the invariant mass of the decay products.

At FAIR the leptonic as well as the hadronic decay channel can be explored. While the leptonic channel is usually regarded as the 'cleaner' channel the calculations discussed in the previous chapter have shown that the dilepton channel might not probe the dense phase as it was expected before. In light of this new development it is worthwhile to evaluate the density-profile and the space-time-evolution of resonances which can be reconstructed in the hadronic decay channels. Although those channels suffer from the drawback of final state interaction of the decay products, their large branching ratios might make them better suited for the investigation of the high density phase of heavy ion collisions compared to leptonic decay channels.

As already mentioned in chapter 8, the experimental reconstruction of resonances is challenging. One often applied technique is to reconstruct the invariant mass spectrum for single events. Then, an invariant mass distribution of mixed events is generated (here, the particle pairs are uncorrelated by definition). The mixed event distribution is subtracted from the invariant mass spectrum of the single (correlated) events. As a result one obtains the mass distributions and yields (after all experimental corrections) of the

resonances by fitting the resulting distribution with a suitable function (usually a Breit-Wigner function peaked around the pole mass of the respective resonance).

If the resonance spectral function changes in the hadronic medium this is in principle visible in the difference spectrum between true and mixed events. However, if a daughter particle (re-)scatters before reaching the detector the signal for the experimental reconstruction is blurred or even lost. Especially for strongly interacting decay products this effect can be sizeable. It is therefore difficult to judge whether a deviation from an expected Breit-Wigner distribution is due to an initial deformation or an increase of the initial width or due to the momentum dependence of the rescattering cross section of the daughter particles.

What makes this analysis even tougher is the fact that the resonances decay over a wide range of densities and therefore only an average value is measured. If this average value is dominated by resonance decays at low density the information from the high density phase is blurred and may offer only a limited view on the high density phase of the heavy ion collision.

UrQMD offers a different technique for the extraction of resonances which we apply here. We follow the individual decay products of each decaying resonance (the daughter particles). If the daughter particles do not rescatter in the further evolution of the system, the resonance is counted as “reconstructable”. The advantage of this method is that it allows to trace back the origin of each individual resonance to study their spatial and temporal emission pattern. Because UrQMD follows the space time evolution of all particles it is possible to link production and decay point of each individual resonance. This method also allows to explore the reconstruction efficiency in different decay branches.

In order to calculate at which density the resonance decays we have to determine the baryonic density. The baryon density is calculated locally at the position of the resonance in the rest frame of the baryon current (Eckart frame) as $\rho_B = j^0$ with $j^\mu = (\rho_B, \vec{0})$. Details on the calculation of the baryon

density are discussed in the Appendix. In all figures we present the density in units of ground state density, where a value of 0.16 1/fm^3 is assumed, which is in accordance to [RRM+86]. In the following we discuss the density dependence of the probability that a resonance can be reconstructed. Naively, one would expect that the higher the densities the more the rescattering effect becomes dominant. Therefore it is unlikely that a resonance which decays at high density is reconstructable. The view on the low density zone is expected to remain unblurred but is less interesting because it resembles that observed in elementary collisions.

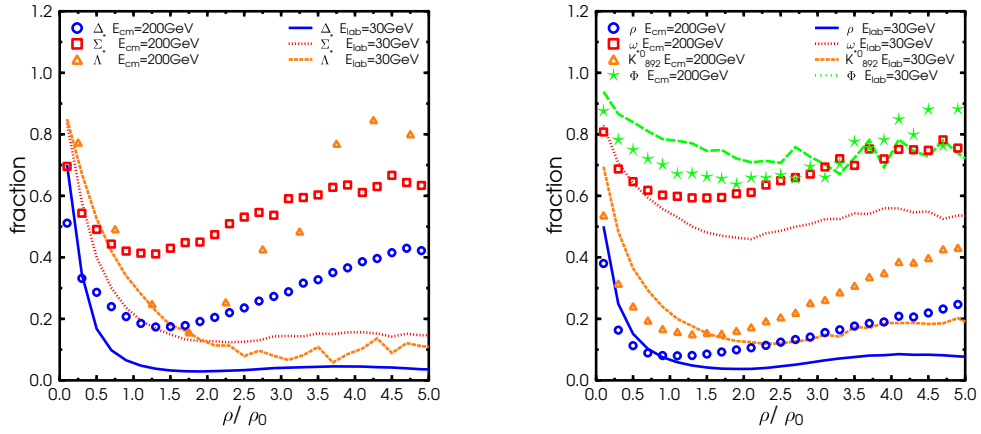


Figure 12.1: Fraction of reconstructable baryon resonances (left) and meson resonances (right) as a function of baryon density at the point of production for central Au+Au collisions at $E_{lab}=30$ AGeV and $\sqrt{s}=200$ AGeV. One observes a clear splitting in lifetime of the resonance for both energies.

12.2 Reconstruction probability in heavy ion collisions

Depicted in Fig. 12.1 left (right) is the probability that a resonance - shown are Δ , $\Sigma^*(1385)$ and $\Lambda^*(1520)$ baryon resonances (ρ , ω , K^{*0} and Φ mesons) - which was produced at a certain density can be reconstructed experimen-

tally. One observes a clear peak at very low density and a steady decrease towards higher density. This means that resonances that are produced at rather low density have a high probability to be detected and as the density increases the chance to reconstruct the resonances decreases. This is nothing unexpected. However, this trend stops at roughly $2 \rho_0$. At higher densities the chance to reconstruct a resonance saturates or even increases slightly again. This increase, which we discuss later in detail, is caused by resonances which picked up very high transverse momenta and leave the interaction zone quickly. This results in a decay in a region with less hadronic activity and a higher chance to be reconstructed.

Whereas the form of the curves is qualitatively similar for the different hadrons the absolute value of the fraction of reconstructable resonances is rather different. It can be understood in terms of lifetimes of the resonances and in terms of the rescattering cross sections of the decay products.

Due to the large cross section of pions in nuclear matter (usually undergoing $N + \pi \rightarrow \Delta$ or $\pi + \pi \rightarrow \rho$ reactions) the probability to detect a high density Δ resonance or a ρ meson is rather small compared to the probability to detect a high density Φ meson, since the Φ meson itself has a small cross section in nuclear matter and a long lifetime of ~ 40 fm/c and the hadronic decay products (mostly kaons and antikaons) have a smaller cross sections when compared to the pions from the decay of a ρ meson. Similarly, the long lifetime of the Λ increases their possibility to be reconstructed. As mentioned earlier, the saturation or slight increase of the reconstruction probability as a function of density has its origin in the possibility that resonances with a large p_T can escape quickly from the reaction zone which is rather small initially.

Fig. 12.2 shows the density spectrum for various experimentally reconstructable resonances. The integral over all densities is normalized to unity. One observes that most of those resonances are produced at very low densities, which is especially true for the mesonic resonances.

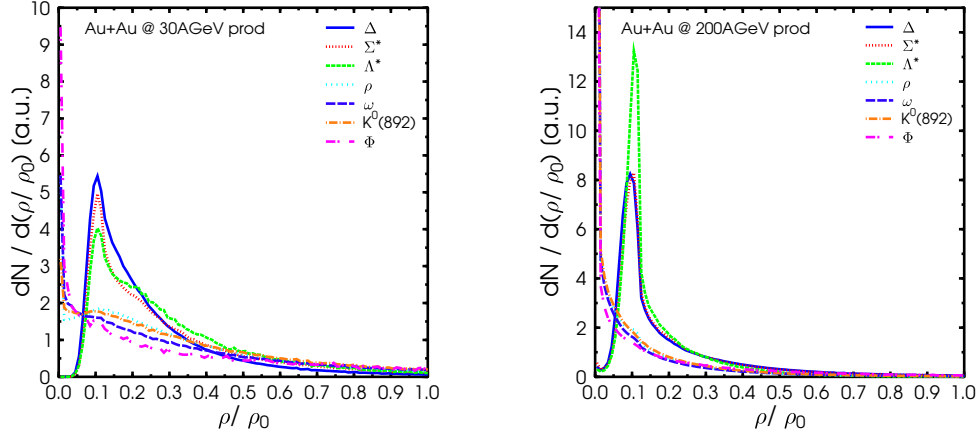


Figure 12.2: Probability distribution of baryon density at the production vertex for various reconstructable resonances in central ($b \leq 3.4$ fm) Au+Au collisions at 30 AGeV (left figure) and 200 AGeV (right figure) as a function of baryon density. One observes that most resonances which can be reconstructed in the hadronic decay channel originate from low baryon density.

Reconstructable baryon resonances stem from slightly higher baryon densities, however most are still produced at rather low densities (with a peak at roughly 0.1 ground state density). So the detection of resonances produced at densities above ground state densities using hadronic decay channels seems not too encouraging. However, as we discuss next, a loophole might exist.

12.3 Using high p_T resonances to explore the hot and dense phase

Let us illustrate this further with two examples which however are representative for all investigated particles.

Fig. 12.3 depicts the average transverse momentum of Δ (left) and ρ resonances (right) as a function of baryon density. Lines show reconstructable

12.3. USING HIGH P_T RESONANCES TO EXPLORE THE HOT AND DENSE PHASE

resonances, symbols show all decayed resonances. The striking feature is the different average transverse momentum between all resonances and those which are reconstructable. The higher the average transverse momentum, the larger is the chance that the resonance can be reconstructed. The $\langle p_T \rangle$ of reconstructable Δ resonances is about 200 MeV higher than for all Δ resonances. Resonances with a large p_T can leave the high density zone rather fast and move with a velocity of about $\langle p_T \rangle / m$ outwards.

Another interesting feature in Fig. 12.3 is the difference between the $\sqrt{s}=200$ AGeV and $E_{lab}=30$ AGeV curves. While the $E_{lab}=30$ AGeV data shows a decrease of $\langle p_T \rangle$ as a function of the baryon density, the $\sqrt{s}=200$ AGeV data show an increase. At $\sqrt{s}=200$ AGeV the initial collisions (which happen at high baryon density) are more energetic and give the particles a high transverse momentum, subsequent rescattering decreases p_T . For the $E_{lab}=30$ AGeV collisions the situation is opposite. Initially the particle p_T is small and the rescattering increases the p_T due to transverse expansion.

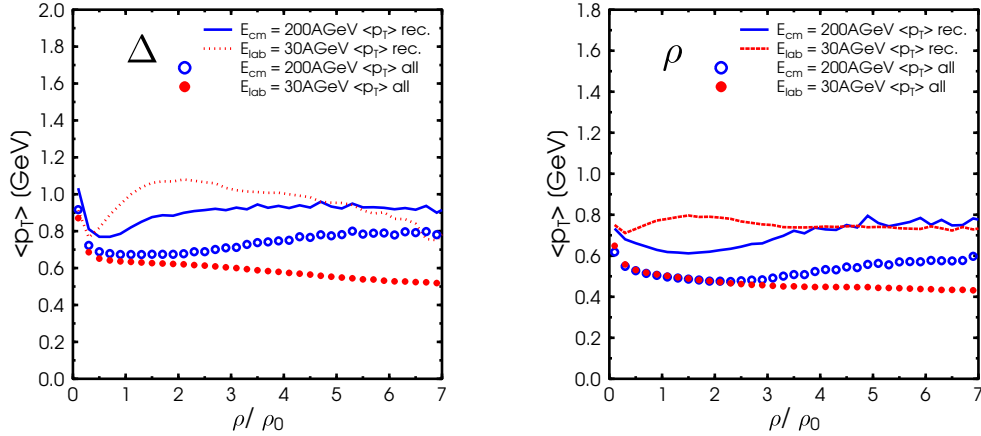


Figure 12.3: Average transverse momentum of reconstructable (line) or all (symbol) Δ baryons (left) and ρ mesons (right) as a function of baryon density for two different energies.

Fig. 12.4 shows the p_T dependence of the reconstruction probability in detail. The left figure is calculated for central Au+Au collisions at 30 GeV beam energy, whereas the right figure is calculated for 200 GeV center of mass

energy. The figures depict the transverse momentum spectra for all (full symbols) and reconstructable resonances (open symbols). The numbers stated in the three shaded areas ($p_T < 1$ GeV, $1 \text{ GeV} < p_T < 2$ GeV, $p_T > 2$ GeV) are the percentages of reconstructable resonances created at a density higher than $2\rho_0$. One observes that at low transverse momentum the percentage of reconstructable resonances is low and increases when going to higher transverse momenta, i.e. that with increasing p_T the chance to reconstruct a resonance produced at high baryon density increases.

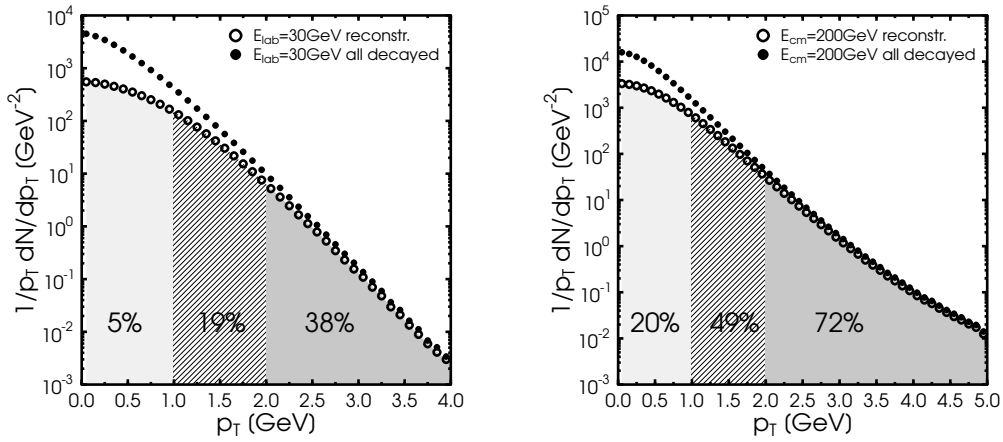


Figure 12.4: Transverse momentum spectra for all and reconstructable resonances for central ($b \leq 3.4$ fm) Au+Au collision at 30 AGeV beam energy. Full circles depict the spectrum for all decayed resonances (included in the analysis are Δ, Λ, Σ baryons, as well as ρ, ω, K^{*0} and ω mesons), open circles for reconstructable resonances. The numbers indicate the percentage of reconstructable resonances stemming from density region with $\rho/\rho_0 > 2$.

This is encouraging on the one hand, since it might give a handle on the high density zone of heavy ion collisions, however on the other hand high p_T resonances are a rare probe and such might be not as accessible as particles from the bulk of the collision. It has to be studied thoroughly if the experimental feasibility is given, however first steps in that direction are already performed [M07b, MBV08].

— *A conclusion is the place where you got tired of thinking.*

Arthur Bloch

13

Conclusions

This thesis discussed several techniques to explore the high density zone of Heavy Ion Collisions.

After giving an introduction to the physics of high energy heavy ion collisions in chapter 2 and giving examples of possible observables we explained the basics of chiral symmetry in chapter 3. Here we explained the symmetry transformations in detail and gave an overview of some experimental observables with focus on mass shifts and broadenings of spectral functions. Chapter 4 gave an overview over the physics of dileptons and within that chapter the relevant and applied branching ratios and decay widths have been calculated. The shining method has been explored in detail. The following chapter scratched the surface of experimental physics and gave a superficial overview over the detectors measuring. Chapter 6 then gave an overview on existing models for heavy ion collisions. Here

especially the Ultra-Relativistic Quantum Molecular Approach (which has been applied for this thesis) has been discussed.

In chapter 7 some recent studies involving resonances and dileptons were presented, especially experimental results from the STAR, NA60, HADES and CLAS collaborations.

First results have been presented in chapter 8, where the mass spectrum of the a_1 meson has been analyzed. We found that the mass spectrum is distorted when analyzed in the $\gamma\pi$ decay channel due to mass dependent branching ratios. That makes a straight forward analysis of the a_1 meson in that (otherwise promising) decay channel very difficult, if not impossible.

After having investigated this possible signal for chiral symmetry restoration we turned our attention to the potential broadening of vector mesons. Here a possible approach is to investigate dilepton spectra and investigate the region where one expects the vector mesons. The mass spectra and the deviations from a full vacuum calculations are discussed in chapter 9. The analysis shows that the low mass region of the dilepton spectra for C+C collisions is slightly underestimated by the model calculations at 1 AGeV, but well described at 2 AGeV. So one would not expect serious mass shifts or broadenings at those energies and systems. The time and density evolution has been reported in chapter 10. In particular, the influence of absorption of the parent resonances on their dilepton emission has been discussed. We found that absorption is responsible for a global suppression of the dilepton signal of about a factor 1.5-2. The absorption processes are more copious in the high density phase, resulting in a stronger suppression for particles (and therefore dileptons) produced at the highest densities.

In the following chapter 11 we analyzed the sensitivity of the ρ meson on the high density phase. We have shown that the measured dileptons provide only a restricted view into the most dense stages of the reaction despite the fact that electromagnetic probes leave the reaction zone without any further interaction. Thus, possible studies of meson and baryon properties at highest baryon densities might be blurred. For the ρ meson we have shown that the baryon density probed in the dilepton decay channel does depend on the method of dilepton extraction employed. We argued that

the absorption of resonances in the high baryon density region of a heavy ion collision masks information from the early hot and dense stage. To demonstrate this, we have split the contributions of the loss term of the ρ meson yield into “loss(absorbed)” and “loss(decayed)” and have shown that at early times, i.e. at the highest baryon densities the absorption results in substantial reduction of the ρ meson life times.

After having discussed mostly electromagnetic decay channels, chapter 12 discussed the hadronic decay channels in more detail. Here we found that the straight forward analysis of all decays does not work, which however was not unexpected. Instead of analyzing resonances from the bulk it might be very beneficial to analyze resonances with high transverse momenta. We argued that those resonances are sensitive to higher densities compared to resonances from the bulk. It will be interesting to explore if the properties of these resonances are different from the bulk emitted at low densities. This novel technique might therefore open a new keyhole for the exploration of the hot and dense phase of heavy ion collisions.

In conclusion we have shown that the analysis of observables which can be linked to chiral symmetry is very tedious and many difficulties lie ahead. It is not straightforward to gather information from the hot and dense phase in heavy ion collisions, however some loopholes exist.

Although the measured mass spectrum of the a_1 meson might be distorted for kinematic reasons it still is an interesting observable and it might be possible in the future to gather information on the a_1 spectral function. It will be of importance to gather more details about the specific decay channel. In general it will be important to gather as much information from elementary collisions, since all results gained from heavy ion collisions will need to have a reference measurement (or calculation).

One of the most promising signals to measure the hot and dense phase we have analyzed might be the hadronic decay channel of resonances, where the

resonances have a high transverse momentum. However the dependency on the transverse momentum might lead to the problem that this probe will be hard to measure. However first experimental steps are taken in that direction.

The study of resonances as a signal for chiral symmetry restoration is an active field of science. The work presented in this thesis is a part of collaborative effort and research on the topics discussed is still ongoing.

Nomenclature

- We use natural units, that means if not noted otherwise

$$\hbar = c = k_B = 1. \quad (13.1)$$

This leads to two significant units, namely MeV, being the unit of energy, mass, momentum and temperature, and fm being the unit of space and time. It is interesting to note that inverse energy equals space and time unit-wise (and vice versa). The conversion factor from inverse MeV to fm is then

$$\hbar c = 1 = 197 \text{ MeVfm}. \quad (13.2)$$

- We follow Einstein's sum convention, meaning that we sum over identical co- and contravariant indices.
- $g_{\mu\nu}$ denotes the flat metric, with the entries $\text{diag}[1,-1,-1,-1]$.
- Greek indices run from 0 to 3, with the 0th component being the time (in case of a space vector) or respectively the energy component (in case of a momentum vector).

Appendix: The four-current method

The local baryon density at a space point i is the zeroth component of the baryon four-current $j^\mu = (\rho_B, \vec{j})$. The local rest frame (RF) baryon density at this space point is defined in the frame where the three-current vanishes, $j_{RF}^\mu = (\rho_{B,RF}, \vec{j}_{RF})$, with $\vec{j}_{RF} = 0$. This definition is known as the Eckart frame. Other definitions are possible, e.g. in the Landau frame, the energy-momentum tensor is at rest while a baryon three-current might still be present. We believe however, that the Eckart frame definition captures the relevant physics at the energy regime under investigation.

In the context of the UrQMD model quantities are (per default) calculated in the computational frame (CF) which is (for symmetric systems) the center-of-mass frame of the whole heavy ion collision. In the computational frame one is only able to evaluate $j_{CF}^\mu = (\rho_{B,CF}, \vec{j}_{CF})$ where $\rho_{B,CF} = N/V$ is the baryon density (N denoting baryon number in the volume, V being the small local volume around the position i) and $\vec{j}_{CF} = \rho_{B,CF} \vec{\beta}$. In the limit of an infinitely small volume, the density $\rho_{B,CF}$ is a sum of Gaussians at position i :

$$\begin{aligned} \rho_{CF}(\vec{r}_i) &= \sum_{j=1}^N \left(\frac{1}{\sqrt{2\pi}\sigma} \right)^3 \gamma_z e^{-\frac{(x-x_0)^2+(y-y_0)^2+(z-z_0)^2\gamma_z^2}{2\sigma^2}} \\ &= \sum_{j=1}^N P_j \end{aligned} \quad (13.3)$$

i.e., a three-dimensional in z -direction contracted and normalised Gaussian with $\gamma_z = 1/\sqrt{1-\beta_z^2}$ being the Lorentz factor for the particle under consideration. The normalisation is different for individual particles due to the different γ factors. The nominal width of the Gaussian is case $\sigma = 1.5$ fm. The particle that defines position i has to be included in the sum because one is interested in the baryon density in the local rest frame of the cell and not in the density around a particle in its rest frame.

The velocity of the cell is computed with the same Gaussians as used for the density calculation as weighting functions. Therefore, the velocity of the cell in the computational frame is:

$$\vec{\beta}_{CF} = \frac{\sum_{j=1}^N \left(\frac{\vec{p}_j}{E_j} \right) \cdot P_j}{\sum_{j=1}^N P_j}$$

The last step is to perform a general Lorentz boost of the four-vector j_{CF}^μ into the local rest frame of the cell. I.e. a Lorentz transformation with the velocity of the cell $\vec{\beta}_{CF}$. The transformation matrix is the following:

$$\begin{pmatrix} \gamma & -\beta_x \gamma & -\beta_y \gamma & -\beta_z \gamma \\ -\beta_x \gamma & 1 + (\gamma - 1) \frac{\beta_x^2}{\beta^2} & (\gamma - 1) \frac{\beta_x \beta_y}{\beta^2} & (\gamma - 1) \frac{\beta_x \beta_z}{\beta^2} \\ -\beta_y \gamma & (\gamma - 1) \frac{\beta_y \beta_x}{\beta^2} & 1 + (\gamma - 1) \frac{\beta_y^2}{\beta^2} & (\gamma - 1) \frac{\beta_y \beta_z}{\beta^2} \\ -\beta_z \gamma & (\gamma - 1) \frac{\beta_z \beta_x}{\beta^2} & (\gamma - 1) \frac{\beta_z \beta_y}{\beta^2} & 1 + (\gamma - 1) \frac{\beta_z^2}{\beta^2} \end{pmatrix}$$

with $\beta^2 = \beta_x^2 + \beta_y^2 + \beta_z^2$ and $\gamma = 1/\sqrt{1 - \beta^2}$. The zero-component of the transformed j^μ four-vector is the local rest frame baryon density we are interested in and are using in our analyses.

Bibliography

- [A+91] M. Aguilar-Benitez *et al.*, Z. Phys. C **50**, 405 (1991).
- [A+95] G. Agakishiev *et al.* [CERES], Phys. Rev. Lett. **75**, 1272 (1995)
- [A+97] R. Averbeck *et al.* [TAPS], Z. Phys. A **359**, 65 (1997)
- [A+01] S. V. Afanasev *et al.* [NA49], J. Phys. G **27**, 367 (2001)
- [A+03] D. Adamova *et al.* [CERES], Phys. Rev. Lett. **91**, 042301 (2003)
- [A+05a] J. Adams *et al.* [STAR], Phys. Rev. C **71**, 064902 (2005)
- [A+05b] J. Adams *et al.* [STAR], Phys. Lett. B **612**, 181 (2005)
- [A+06a] J. Adams *et al.* [STAR], Phys. Rev. Lett. **97**, 132301 (2006)
- [A+06b] R. Arnaldi *et al.* [NA60], Phys. Rev. Lett. **96**, 162302 (2006)
- [A+07] G. Agakishiev *et al.* [HADES], Phys. Rev. Lett. **98**, 052302 (2007)
- [A+08a] B. I. Abelev *et al.* [STAR], Phys. Rev. C **78**, 044906 (2008)
- [A+08b] D. Adamova *et al.* [CERES], Phys. Lett. B **666**, 425 (2008)
- [A+08c] G. Agakishiev *et al.* [HADES], Phys. Lett. B **663**, 43 (2008)
- [A+09] G. Agakishiev *et al.* [HADES], arXiv:0902.3478
- [A86] J. Aichelin and H. Stoecker, Phys. Lett. B **176**, 14 (1986)
- [A91] J. Aichelin, Phys. Rept. **202**, 233 (1991)

- [ABBM+08] A. Andronic, F. Beutler, P. Braun-Munzinger, K. Redlich and J. Stachel, arXiv:0804.4132
- [ABMRS03] A. Andronic, P. Braun-Munzinger, K. Redlich and J. Stachel, Nucl. Phys. A **715**, 529 (2003)
- [AGK+08] I. Augustin, H. H. Gutbrod, D. Kramer, K. Langanke and H. Stoecker, arXiv:0804.0177
- [AKNS85] V.V. Anisovich, M.N. Kobrinsky, J. Nyiri and Y. Shabelski, *Quark model and high energy collisions*, (World Scientific, Singapore, 1985)
- [ALICE] <http://aliceinfo.cern.ch/Collaboration/Documents/TDR/index.html>
- [B+96] R. M. Barnett *et al.* [Particle Data Group], Phys. Rev. D **54**, 1 (1996)
- [B+98] S. A. Bass *et al.*, Prog. Part. Nucl. Phys. **41**, 225 (1998)
- [B+99] M. Bleicher *et al.*, J. Phys. G **25** 1859 (1999)
- [B+04] E. L. Bratkovskaya *et al.*, Phys. Rev. C **69**, 054907 (2004)
- [B03] M. Bleicher, Nucl. Phys. A **715**, 85 (2003)
- [BA02] M. Bleicher and J. Aichelin, Phys. Lett. B **530**, 81 (2002)
- [BC08] E. L. Bratkovskaya and W. Cassing, Nucl. Phys. A **807**, 214 (2008)
- [BCEM99] E. L. Bratkovskaya, W. Cassing, M. Effenberger and U. Mosel, Nucl. Phys. A **653**, 301 (1999)
- [BCRW98] E. L. Bratkovskaya, W. Cassing, R. Rapp and J. Wambach, Nucl. Phys. A **634**, 168 (1998)
- [BFB+83] G. Baym, B. L. Friman, J. P. Blaizot, M. Soyeur and W. Czyz, Nucl. Phys. A **407**, 541 (1983)
- [BGSG99] S. A. Bass, M. Gyulassy, H. Stoecker and W. Greiner, J. Phys. G **25**, R1 (1999)

BIBLIOGRAPHY

- [BHS95] S. A. Bass, C. Hartnack, H. Stoecker and W. Greiner, Phys. Rev. C **51**, 3343 (1995)
- [BK99] E. L. Bratkovskaya and C. M. Ko, Phys. Lett. B **445**, 265 (1999)
- [BMMRS] P. Braun-Munzinger, D. Magestro, K. Redlich and J. Stachel, Phys. Lett. B **518**, 41 (2001)
- [BMSWX95] P. Braun-Munzinger, J. Stachel, J. P. Wessels and N. Xu, Phys. Lett. B **344**, 43 (1995)
- [BMSWX96] P. Braun-Munzinger, J. Stachel, J. P. Wessels and N. Xu, Phys. Lett. B **365**, 1 (1996)
- [BR91] G. E. Brown and M. Rho, Phys. Rev. Lett. **66**, 2720 (1991)
- [BR95] G. E. Brown and M. Rho, Phys. Rept. **269**, 333 (1996)
- [BR02] G. E. Brown and M. Rho, Phys. Rept. **363**, 85 (2002)
- [BR05a] G. E. Brown and M. Rho, arXiv:nucl-th/0509001
- [BR05b] G. E. Brown and M. Rho, arXiv:nucl-th/0509002
- [BS04] M. Bleicher and H. Stoecker, J. Phys. G **30**, S111 (2004)
- [BZK71] A. Bialas, K. Zalewski and A. Kotanski, Nucl. Phys. B **28**, 1 (1971)
- [C+98] H. Calen *et al.*, Phys. Rev. C **58**, 2667 (1998)
- [CB99] W. Cassing and E. L. Bratkovskaya, Phys. Rept. **308**, 65 (1999)
- [CBJ00] W. Cassing, E. L. Bratkovskaya and S. Juchem, Nucl. Phys. A **674**, 249 (2000)
- [CBM] CBM homepage: <http://www.gsi.de/fair/experiments/CBM/>
- [CBRW98] W. Cassing, E. L. Bratkovskaya, R. Rapp and J. Wambach, Phys. Rev. C **57**, 916 (1998)

- [CEK95] W. Cassing, W. Ehehalt and C. M. Ko, Phys. Lett. B **363**, 35 (1995)
- [CERES] PhD thesis Matúš Kaliský (TU Darmstadt)
- [CFSF06] M. D. Cozma, C. Fuchs, E. Santini and A. Fassler, Phys. Lett. B **640**, 170 (2006)
- [CORW06] J. Cleymans, H. Oeschler, K. Redlich and S. Wheaton, Eur. Phys. J. A **29**, 119 (2006)
- [CR99] J. Cleymans and K. Redlich, Phys. Rev. C **60**, 054908 (1999)
- [CS81] L. P. Csernai and H. Stoecker, Phys. Rev. C **25**, 3208 (1981)
- [CS93] J. Cleymans and H. Satz, Z. Phys. C **57**, 135 (1993)
- [CSSO90] J. Cleymans, H. Satz, E. Suhonen and D. W. von Oertzen, Phys. Lett. B **242**, 111 (1990)
- [D96] A. Drees, Nucl. Phys. A **610**, 536C (1996)
- [DFN84] D. Drijard, H. G. Fischer and T. Nakada, Nucl. Instrum. Meth. A **225**, 367 (1984)
- [DLS] DLS Homepage: <http://macdls.lbl.gov/DLS>
- [DMQC91] N. J. Davidson, H. G. Miller, R. M. Quick and J. Cleymans, Phys. Lett. B **255**, 105 (1991)
- [DMO91] N. J. Davidson, H. G. Miller and D. W. von Oertzen, Phys. Lett. B **256**, 554 (1991)
- [DMOR92] N. J. Davidson, H. G. Miller, D. W. von Oertzen and K. Redlich, Z. Phys. C **56**, 319 (1992)
- [DTZ07] K. Dusling, D. Teaney and I. Zahed, Phys. Rev. C **75**, 024908 (2007)

BIBLIOGRAPHY

- [EBB+98] C. Ernst, S. A. Bass, M. Belkacem, H. Stoecker and W. Greiner, Phys. Rev. C **58**, 447 (1998)
- [F08] P. Fachini, J. Phys. G **35**, 044032 (2008)
- [FFK00] A. Faessler, C. Fuchs and M. I. Krivoruchenko, Phys. Rev. C **61**, 035206 (2000)
- [FKM03] A. Faessler, C. Fuchs, M. I. Krivoruchenko and B. V. Martemyanov, J. Phys. G **29**, 603 (2003)
- [FMMR84] V. Flaminio, W. G. Moorhead, D. R. O. Morrison and N. Rivoire, CERN-HERA 84-01 (1984)
- [FP97] B. Friman and H. J. Pirner, Nucl. Phys. A **617**, 496 (1997)
- [GL60] M. Gell-Mann and M. Levy, Nuovo Cimento **16**, 53 (1960)
- [GLL+07] K. Gallmeister, T. Leitner, S. Leupold, U. Mosel, P. Muehlich, L. Alvarez-Ruso and V. Shklyar, Nucl. Phys. A **782**, 166 (2007)
- [H+97] R. Holzmann *et al.* [TAPS], Phys. Rev. C **56**, 2920 (1997)
- [H08] W. F. Henning, Nucl. Phys. A **805**, 502 (2008)
- [HADES] HADES homepage: <http://www-hades.gsi.de/>
- [HL92a] T. Hatsuda and S. H. Lee, Phys. Rev. C **46**, 34 (1992)
- [HL92b] U. W. Heinz and K. S. Lee, Nucl. Phys. A **544**, 503 (1992)
- [K93] P. Koch, Z. Phys. C **57**, 283 (1993)
- [K97] V. Koch, Int. J. Mod. Phys. E **6**, 203 (1997)
- [KB93] V. Koch and G. E. Brown, Nucl. Phys. A **560**, 345 (1993)
- [KBH+95] G. Kortemeyer, W. Bauer, K. Haglin, J. Murray and S. Pratt, Phys. Rev. C **52**, 2714 (1995)
- [KF02] M. I. Krivoruchenko and A. Faessler, Phys. Rev. D **65**, 017502 (2002)

- [KH03] P. F. Kolb and U. W. Heinz, arXiv:nucl-th/0305084.
- [KK06] L. P. Kaptari and B. Kampfer, Nucl. Phys. A **764**, 338 (2006)
- [KLBS96] C. M. Ko, G. Q. Li, G. E. Brown and H. Sorge, Nucl. Phys. A **610**, 342C (1996)
- [KLW90] S. Klimt, M. Lutz and W. Weise, Phys. Lett. B **249**, 386 (1990).
- [KRR83] K. Kajantie, R. Raitio and P. V. Ruuskanen, Nucl. Phys. B **222**, 152 (1983)
- [KS96] V. Koch and C. Song, Phys. Rev. C **54**, 1903 (1996)
- [KTBF06] A. Kisiel, T. Taluc, W. Broniowski and W. Florkowski, Comput. Phys. Commun. **174**, 669 (2006)
- [L+07] X. Lopez *et al.* [FOPI], Phys. Rev. C **76**, 052203 (2007)
- [L85] L. G. Landsberg, Phys. Rept. **128**, 301 (1985)
- [LK95] G. Q. Li and C. M. Ko, Nucl. Phys. A **582**, 731 (1995)
- [LKB95] G. Q. Li, C. M. Ko and G. E. Brown, Phys. Rev. Lett. **75**, 4007 (1995)
- [LKBS96] G. Q. Li, C. M. Ko, G. E. Brown and H. Sorge, Nucl. Phys. A **611**, 539 (1996)
- [LKL+05] Z. W. Lin, C. M. Ko, B. A. Li, B. Zhang and S. Pal, Phys. Rev. C **72**, 064901 (2005)
- [LRT94] J. Letessier, J. Rafelski and A. Tounsi, Phys. Lett. B **328**, 499 (1994)
- [LWF02] M. F. M. Lutz, G. Wolf and B. Friman, Nucl. Phys. A **706**, 431 (2002) [Erratum-ibid. A **765**, 431 (2006)].
- [M94] M. A. Mazzoni [HELIOS/3], Nucl. Phys. A **566**, 95C (1994)

BIBLIOGRAPHY

- [M06] D. Miskowiec [CERES], Nucl. Phys. A **774**, 43 (2006)
- [M07a] C. Markert, arXiv:0706.0729 [nucl-ex].
- [M07b] C. Markert [STAR], arXiv:0706.0724
- [M08] C. Markert [STAR], J. Phys. G **35**, 044029 (2008)
- [MBV08] C. Markert, R. Bellwied and I. Vitev, Phys. Lett. B **669**, 92 (2008)
- [MG00] D. Molnar and M. Gyulassy, Phys. Rev. C **62**, 054907 (2000)
- [MSL+06] P. Muehlich, V. Shklyar, S. Leupold, U. Mosel and M. Post, Nucl. Phys. A **780**, 187 (2006)
- [MTR02] C. Markert, G. Torrieri and J. Rafelski, arXiv:hep-ph/0206260.
- [N+06] M. Naruki *et al.*, Phys. Rev. Lett. **96**, 092301 (2006)
- [NA60] NA60 homepage: <http://na60.cern.ch>
- [O+01] K. Ozawa *et al.* [E325], Phys. Rev. Lett. **86**, 5019 (2001)
- [P+97] R. J. Porter *et al.* [DLS], Phys. Rev. Lett. **79**, 1229 (1997)
- [P87] D. H. Perkins, Introduction to High Energy Physics, Addison-Wesley Publishing, 1987
- [P95] R. D. Pisarski, Phys. Rev. D **52**, 3773 (1995)
- [PBBS08] H. Petersen, M. Bleicher, S. A. Bass and H. Stoecker, arXiv:0805.0567
- [PHENIX] PhD thesis Christian Klein-Bösing (Univ. Münster)
- [PM01] M. Post and U. Mosel, Nucl. Phys. A **688**, 808 (2001)
- [PM02] M. Post and U. Mosel, Nucl. Phys. A **699**, 169 (2002)
- [PPL+98] W. Peters, M. Post, H. Lenske, S. Leupold and U. Mosel, Nucl. Phys. A **632**, 109 (1998)

- [R03] R. Rapp, Nucl. Phys. A **725**, 254 (2003)
- [R07] R. Rapp, Nucl. Phys. A **782**, 275 (2007)
- [RCW96] R. Rapp, G. Chanfray and J. Wambach, Phys. Rev. Lett. **76**, 368 (1996)
- [RCW97] R. Rapp, G. Chanfray and J. Wambach, Nucl. Phys. A **617**, 472 (1997)
- [RGR+08] J. Ruppert, C. Gale, T. Renk, P. Lichard and J. I. Kapusta, Phys. Rev. Lett. **100**, 162301 (2008)
- [RR07] J. Ruppert and T. Renk, Eur. Phys. J. C **49**, 219 (2007)
- [RRM06] J. Ruppert, T. Renk and B. Muller, Phys. Rev. C **73**, 034907 (2006)
- [RRM+86] P. G. Reinhard, M. Rufa, J. Maruhn, W. Greiner and J. Friedrich, Z. Phys. A **323**, 13 (1986)
- [RW00] R. Rapp and J. Wambach, Adv. Nucl. Phys. **25**, 1 (2000)
- [S+92] H. Stoecker *et al.*, Nucl. Phys. A **538**, 53C (1992)
- [S+01] C. Sturm *et al.* [KaoS], Phys. Rev. Lett. **86** 39 (2001)
- [S+05] S. Schael *et al.* [ALEPH], Phys. Rept. **421**, 191 (2005)
- [S69] J.J. Sakurai, Currents and mesons, University of Chicago Press, Chicago, 1969
- [S95] H. Sorge, Phys. Rev. C **52**, 3291 (1995)
- [S03] E. V. Shuryak, Heavy Ion Phys. **21**, 185 (2004)
- [S06] G. S. F. Stephans, J. Phys. G **32**, S447 (2006)
- [SBCM89] M. Schafer, T. S. Biro, W. Cassing and U. Mosel, Phys. Lett. B **221**, 1 (1989)

BIBLIOGRAPHY

- [SCF+08] E. Santini, M. D. Cozma, A. Faessler, C. Fuchs, M. I. Krivoruchenko and B. Martemyanov, *Phys. Rev. C* **78**, 034910 (2008)
- [SFF+03] K. Shekhter, C. Fuchs, A. Faessler, M. Krivoruchenko and B. Martemyanov, *Phys. Rev. C* **68**, 014904 (2003)
- [SK96] C. Song and C. M. Ko, *Phys. Rev. C* **53**, 2371 (1996)
- [SM03] R. Shyam and U. Mosel, *Phys. Rev. C* **67**, 065202 (2003)
- [SM08] R. Shyam and U. Mosel, arXiv:0811.0739
- [SSG89] H. Sorge, H. Stoecker and W. Greiner, *Annals Phys.* **192**, 266 (1989)
- [SSU93] E. Schnedermann, J. Sollfrank and U. W. Heinz, *NATO Adv. Study Inst. Ser. B Phys.* **303**, 175 (1993).
- [SSV+09] K. Schmidt, E. Santini, S. Vogel, C. Sturm, M. Bleicher and H. Stoecker, *Phys. Rev. C* **79**, 064908 (2009)
- [SVB06] D. Schumacher, S. Vogel and M. Bleicher, *Acta Phys. Hung. A* **27**, 451 (2006)
- [TCE+97] S. Teis, W. Cassing, M. Effenberger, A. Hombach, U. Mosel and G. Wolf, *Z. Phys. A* **356**, 421 (1997)
- [THWA07] M. Thomere, C. Hartnack, G. Wolf and J. Aichelin, *Phys. Rev. C* **75**, 064902 (2007)
- [TR01] G. Torrieri and J. Rafelski, *Phys. Lett. B* **509**, 239 (2001)
- [TR03] G. Torrieri and J. Rafelski, *Phys. Rev. C* **68**, 034912 (2003)
- [TR04] G. Torrieri and J. Rafelski, *Nukleonika* **49**, S109 (2004)
- [TW80] H. H. K. Tang and C. Y. K. Wong, *Phys. Rev. C* **21**, 1846 (1980)
- [VB05] S. Vogel and M. Bleicher, arXiv:nucl-th/0505027

- [VB06a] S. Vogel and M. Bleicher, Phys. Rev. C **74**, 014902 (2006)
- [VB06b] S. Vogel and M. Bleicher, Rom. Rep. Phys. **58**, 63 (2006)
- [VB08] S. Vogel and M. Bleicher, Phys. Rev. C **78**, 064910 (2008)
- [vHR06] H. van Hees and R. Rapp, Phys. Rev. Lett. **97**, 102301 (2006)
- [VPS+08] S. Vogel, H. Petersen, K. Schmidt, E. Santini, C. Sturm, J. Aichelin and M. Bleicher, Phys. Rev. C **78**, 044909 (2008)
- [W+96] L. A. Winckelmann *et al.*, Nucl. Phys. A **610**, 116C (1996)
- [W+98] W. K. Wilson *et al.* [DLS], Phys. Rev. C **57**, 1865 (1998)
- [W+08] M. H. Wood *et al.* [CLAS], Phys. Rev. C **78**, 015201 (2008)
- [W07] R. Witt, arXiv:nucl-ex/0701063
- [WBC+90] G. Wolf, G. Batko, W. Cassing, U. Mosel, K. Niita and M. Schaefer, Nucl. Phys. A **517**, 615 (1990)
- [WCMS90] G. Wolf, W. Cassing, U. Mosel and M. Schaefer, Phys. Rev. C **43**, 1501 (1990)
- [WCM93] G. Wolf, W. Cassing and U. Mosel, Prog. Part. Nucl. Phys. **30**, 273 (1993) [Nucl. Phys. A **552** (1993 NUPHA,A545,139C-150C.1992) 549]
- [WDNW07] D. P. Weygand, C. Djalali, R. Nasseripour and M. Wood [CLAS], Int. J. Mod. Phys. A **22**, 380 (2007)
- [WL07] M. Wagner and S. Leupold, arXiv:0708.2223
- [WSSG95] L. A. Winckelmann, H. Sorge, H. Stoecker and W. Greiner, Phys. Rev. C **51**, 9 (1995)
- [XG05] Z. Xu and C. Greiner, Phys. Rev. C **71**, 064901 (2005)
- [XKL90] L. H. Xia, C. M. Ko and C. T. Li, Phys. Rev. C **41**, 572 (1990)

BIBLIOGRAPHY

[Y+06] W. M. Yao *et al.* [Particle Data Group], J. Phys. G **33**, 1 (2006)

[Z98] B. Zhang, Comput. Phys. Commun. **109**, 193 (1998)

Acknowledgements

This work would not have been possible without the help of several people. Let me especially thank Prof. Dr. Marcus Bleicher who made this work possible. He was directly involved with all parts of this thesis and provided constructive feedback, many ideas and made it possible to present my work on several occasions.

Let me also thank Prof. Dr. Horst Stöcker, who got me into the Institute for Theoretical Physics. He created a very unique atmosphere in the institute and provided the freedom to work on several projects. His never-ending enthusiasm and support is contagious, which is one of the reasons the institute works as it does.

Thanks to the people working at ITP, especially the folks directly involved with this thesis (be it via discussions, coding or working together on the project). Let me especially thank Barbara Betz, Oliver Fochler, Mauricio Martinez Guerrero, Elvira Santini, Katharina Schmidt and Giorgio Torrieri. Let me also thank the people outside ITP who contributed to this thesis, especially by proof-reading or helping with code issues: Benjamin Liebing, Thomas Jung and Andreas Renner.

Let me also thank my former room-mates, especially Kerstin Paech, Yasushi Nara, Harmen Warringa and Susanne Ehret for the excellent working atmosphere in the office.

Many thanks to Tilo Havermeier, for the many Kicker-matches during coffee-breaks.

The Helmholtz Research School on Quark Matter Studies (H-QM) provided me with a great framework and infrastructure. I benefited from the lecture weeks, the softskill-program and mostly from the people attending. Many thanks go especially to Henner Büsching, who organized the program with great effort and enthusiasm.

Special thanks also goes to Joerg Aichelin and Boris Tomasik, both provided me with the opportunity to work in different institutes for some time. Working at Subatech and Mateja Bela University was a very pleasant experience.

Very special thanks go out to the lunch crew consisting of Thomas Buervenich, Thomas Cornelius, Uli Harbach and Jason Stuber. The tradition of TPC will live on.

The computational resources have been provided by the Center for Scientific Computing (CSC). Although exchanging mails back and forth about deleting huge files and buying more harddrives I deeply acknowledge their work and without the cluster and the people behind we never were able to do the calculations.

Finally and most importantly let me say thank you to my family and my girlfriend Patricia, without them and their support my studies and writing this thesis would have not been possible. Thank you.

Curriculum Vitae

Personal Data

Name: Sascha Vogel
Address: Hamburger Allee 56
City: 60486 Frankfurt
eMail: svogel@th.physik.uni-frankfurt.de
Date of Birth: 01.02.1982
Birthplace: Frankfurt am Main
Nationality: German
Marital Status: single

Education

1988-1992	Villa-Kunterbunt-Grundschule, Maintal
1992-2001	Albert-Einstein-Gymnasium, Maintal
2001	Abitur
2001-2005	Studies in physics, mathematics, geophysics and philosophy at the Johann Wolfgang von Goethe-University Frankfurt
2003	Pre-diploma
2005	Diploma thesis under supervision of Prof. Dr. Bleicher und Prof. Dr. Stöcker, awarded with the Philipp Siedler-Wissenschaftspreis
since 2005	Graduate Studies at the Institute for Theoretical Physics at the Johann Wolfgang Goethe-University Frankfurt am Main
since 2006	Member of the Helmholtz Research Schools for Quark Matter Studies
since 2007	Member of the Otto-Stern-School Frankfurt am Main

Teaching

- Tutorials in
 - Mechanics I
 - Mechanics II
 - Electrodynamics
 - Quantum mechanics
 - Thermodynamics and Statistical Physics
 - Theoretical Nuclear Physics I / II / III
- Teaching Assistant and Lecture substitution for
 - Theoretical Physics I / II: Theoretical Mechanics
 - Theoretical Physics I for Teachers
 - Theoretical Nuclear Physics I / II / III

Publications:

1. M. Bleicher, E. Bratkovskaya, **S. Vogel**, X. Zhu: *Transverse Pressure and Strangeness Dynamics in Relativistic Heavy Ion Reactions*, J. Phys. G **31**, S709 (2005) [arXiv:hep-ph/0503252]
2. O. Fochler, **S. Vogel**, M. Bleicher, C. Greiner, P. Koch-Steinheimer, Z. Xu: *Dynamic Canonical Suppression of Strangeness in Transport Models*, proceedings of the XLIII. International Winter Meeting on Nuclear Physics, Bormio, Italy [arXiv:hep-ph/0505025]
3. **S. Vogel**, M. Bleicher: *Resonance Absorption and Regeneration in Relativistic Heavy Ion Collisions*, proceedings of the XLIII. International Winter Meeting on Nuclear Physics, Bormio, Italy [arXiv:nucl-th/0505027]
4. **S. Vogel**, M. Bleicher: *Reconstructing ρ^0 and ω mesons from non-leptonic decays in C+C at 2A GeV in transport model calculations*, Phys. Rev. C **74**, 014902 (2006) [arXiv:nucl-th/0509105]
5. O. Fochler, **S. Vogel**, M. Bleicher, C. Greiner, P. Koch-Steinheimer, Z. Xu: *Canonical suppression in microscopic transport models*, Phys. Rev. C **74**, 034902 (2006) [arXiv:nucl-th/0601062]
6. **S. Vogel**, M. Bleicher: *Resonance Rescattering and Absorption in Low Energy Heavy Ion Collisions*, Rom. Rep. Phys. **58**, 63 (2006)
7. **S. Vogel**, M. Bleicher: *Reconstructing ρ^0 and ω mesons from non-leptonic decays in C+C at 2A GeV in transport model calculations*, proceedings of the XLIV. International Winter Meeting on Nuclear Physics, Bormio, Italy [arXiv:nucl-th/0505027]

8. **S.Vogel**, M.Bleicher: *Resonance Production in Heavy Ion Collisions - what can we learn from RHIC?*,
proceedings of the 22nd Winter Workshop on Nuclear Dynamics, La Jolla, USA [arXiv:hep-ph/0607242]
9. H.Petersen, **S.Vogel**, X.Zhu, M.Bleicher: *Elliptic Flow and Constituent Quark Scaling in High Energy Nuclear Collisions*,
proceedings of the 22nd Winter Workshop on Nuclear Dynamics, La Jolla, USA
10. D.Schumacher, **S.Vogel**, M.Bleicher: *Theoretical analysis of dilepton spectra in heavy ion collision at GSI-FAIR energies*,
Acta Phys. Hung. A **27**, 451 (2006) [arXiv:nucl-th/0608041]
11. **S.Vogel**, M.Bleicher: *Resonance multiplicities in a hadron transport approach*,
Acta Phys. Hung. A **27**, 421 (2006)
12. **S.Vogel**, H.Petersen, K.Schmidt, E.Santini, J.Aichelin, M.Bleicher: *How sensitive are dileptons from rho mesons to the high baryon density region?*,
Phys. Rev. C **78**, 044909 (2008) [arXiv:0710.4463]
13. **S.Vogel**, M.Bleicher *Evidence for the $a(1)$ meson being a difficult messenger for the restoration of chiral symmetry*,
Phys. Rev. C **78**, 064910 (2008) [arXiv:0710.1158]
14. J.Aichelin, H.Petersen, **S.Vogel**, M.Bleicher, *How can we explore the onset of deconfinement by experiment?*
PoS C **POD07**, 004 (2007) [arXiv:0711.2995]
15. K.Schmidt, E.Santini, **S.Vogel**, C.Sturm, M.Bleicher, H.Stöcker, *Production and evolution path of dileptons at energies accessible to the HADES detector*
Phys. Rev. C **79**, 064908 (2009) [arXiv:0811.4073]

-
16. I.Melo, B.Tomasik, G.Torrieri, **S.Vogel**, M.Bleicher, S.Korony, M.Gintner *The Kolmogorov-Smirnov test and its use for the identification of fireball fragmentation*
Phys. Rev. C **80**, 024904 (2009) [arXiv:0902.1607]
 17. B.Tomasik, I.Melo, G.Torrieri, **S.Vogel**, M.Bleicher *The use of Kolmogorov-Smirnov test in event-by-event analysis*
to appear in the proceedings of the 21st International Conference on Nucleus Nucleus Collisions [arXiv:0907.2179]

In preparation:

18. **S.Vogel**, G.Torrieri, M.Bleicher: Elliptic flow fluctuations in heavy ion collisions at RHIC and the perfect liquid hypothesis,
in preparation
[arXiv:nucl-th/0703031]
19. **S.Vogel**, J.Aichelin, M.Bleicher High p_T resonances as a possibility to explore hot and dense nuclear matter
submitted to Phys. Rev. Lett.
[arXiv:0908.3811]

Presentations**1. DPG-Tagung, Berlin, 2005**

Resonance Absorption and Regeneration in Relativistic Heavy Ion Collisions

2. XVIII. International Winter Meeting on Nuclear Physics, Bormio, 2005

- Resonance Absorption and Regeneration in Relativistic Heavy Ion Collisions
- Canonical Suppression in Microscopic and Stochastic Transport Models

3. 18th International Conference on Nucleus Nucleus Collisions (Quark Matter), Budapest, 2005

Resonance Absorption, Rescattering and Regeneration at SPS and RHIC (Poster)

4. XLIV. International Winter Meeting on Nuclear Physics, Bormio, 2006

Reconstructing ρ^0 and ω mesons from non-leptonic decays in C+C at 2A GeV in transport model calculations

5. 22nd Winter Workshop on Nuclear Dynamics, La Jolla, 2006

Resonance Dynamics in Heavy Ion Collisions - What can we learn from RHIC?

6. International Conference on Strangeness in Quark Matter, Los Angeles, 2006

Resonance Absorption, Rescattering and Regeneration at SPS and RHIC (Poster)

7. 19th International Conference on Nucleus Nucleus Collisions (Quark Matter), Shanghai, 2006

Resonance Absorption, Rescattering and Regeneration at SPS and RHIC (Poster)

8. **DPG-Tagung, Giessen, 2007**
Resonance Studies in Heavy Ion Collisions
9. **Berkeley School on Collective Dynamics, Berkeley, 2007**
How robust are signals for chiral symmetry restoration
10. **ECT* Workshop: Electromagnetic Probes of Strongly Interacting Matter, Trento, 2007**
How robust are signals for chiral symmetry restoration
11. **I3 Workshop of the European Network on the Physics of the Quark Gluon Plasma, Sardinia, 2008**
How robust are signals for chiral symmetry restoration
12. **DPG-Tagung, Bochum, 2009**
How sensitive are dileptons from rho mesons to the high baryon density region?
13. **21st International Conference on Nucleus Nucleus Collisions (Quark Matter), Knoxville, 2009**
Why the a_1 meson might be a difficult messenger for the restoration of chiral symmetry (Poster)
14. **21st International Conference on Nucleus Nucleus Collisions (Quark Matter), Knoxville, 2009**
How sensitive are dileptons from rho mesons to the high baryon density region? (Poster)
15. **International Conference on Strangeness in Quark Matter, Buzios, 2009**
Formation and decay of hadronic resonances in hot and dense nuclear matter

Akademische Lehrer

Prof. Dr. Becker
Prof. Dr. Bleicher
Prof. Dr. Blume
PD Dr. Bruls
Prof. Dr. Dinges
Prof. Dr. Dörner
Prof. Dr. Dumitru
Prof. Dr. Essler
Prof. Dr. Greiner
Prof. Dr. Dr. h.c. mult. Greiner
Prof. Dr. Huth
Prof. Dr. Lang
Prof. Dr. Maruhn
Prof. Dr. Metzler
Prof. Dr. Schempp
Prof. Dr. Schmeling
Dr. Soff
PD Dr. Steinheimer
Prof. Dr. Stock
Prof. Dr. Stöcker
Prof. Dr. Stroth